공학박사학위논문

전단부 혹을 가진 날개 주변의 유동 특성

Characteristics of flow around a wing with leading-edge tubercles

2019 년 2 월

서울대학교 대학원

기계항공공학부

김 희 수

Characteristics of flow around a wing with leading-edge tubercles

Heesu Kim
Department of Mechanical & Aerospace Engineering
Seoul National University

Abstract

Leading-edge tubercles on a humpback whale flipper are known to enhance its hydrodynamic performance at post-stall angles of attack (Miklosovic *et al* 2004). We investigate vortical structures above a three-dimensional wing with tubercles using surface-oil-flow visualization and particle image velocimetry measurement. Two wing models with and without tubercles, previously studied by Miklosovic *et al* (2004), are considered at the Reynolds number of 180,000 based on the free-stream velocity and mean chord length. At this Reynolds number, tubercles delay the stall angle by 7° and increase the maximum lift coefficient by about 22%. At a low angle of attack, flow separation first occurs near the tip region for both wing models. While flow separation rapidly progresses inboard (toward the wing root) for the model without tubercles with increasing angle of attack, tubercles produce two types of vortical motions and block the inboard progression of flow separation, resulting in delayed stall from $\alpha = 8°$ to 15°. One of these two vortical structures is pairs of counter-rotating streamwise vortices evolving from hemi-spherical separation bubbles near the leading edge troughs at pre-, near-, and post-stall angles of attack, and the other is asymmetric pairs of streamwise vortices evolving from separated flow regions after the mid-chord region at near-stall angle of attack. At a post-stall angle of

attack ($\alpha = 16°$), strong clockwise and counter-clockwise streamwise vortices are generated from foci at the root and tip near the trailing edge, respectively, and delay flow separation in the mid-span, resulting in a higher lift coefficient than that without tubercles.

Leading-edge tubercles are applied to the quadrotor blade(Phantom4, DJI) to improve performance in forward flight condition. The new blade has ten tubercles with amplitude of 6% and wavelength of 50% of the mean chord length of the blade without tubercles. The rotating speed is varied from 3,500 RPM to 5,100 RPM corresponding to Reynolds number range of $62{,}000 - 90{,}000$. The forward flight speed is varied from 4 m/s to 16 m/s corresponding to advance ratio range of $0.048 - 0.279$. The angle of attack considered in this study is $40°$. At low advance ratio ($\mu \leq 0.1$), power and thrust coefficients of the both models are similar to each other within the experimental uncertainty range. As advance ratio increases, however, tubercles increase the thrust coefficient more than the power coefficient, indicating the enhancement of the blade performance. Based on velocity field measurement, counter-rotating streamwise vortex pairs are observed in the wake of the blade with tubercles, resulting in reduction of back-flow region behind the peak on the advancing side.

Keywords: humpback whale flipper, leading-edge tubercle, flow separation, stall delay, quadrotor blade, forward flight

Student number: 2013-31295

Contents

List of Figures

Figure

Nomenclature

Roman Symbols

A	planform area of the model
C_D	drag coefficient
C_L	lift coefficient
C_P	pressure coefficient
C_{Po}	power coefficient
C_T	thrust coefficient
c	chord length of the model
c_l	local chord length of the model
D	drag force
L	lift force
P	time-averaged surface pressure
P_∞	static pressure at the free-stream
R	radius of the blade
r	radial location
Re	Reynolds number
s	span length of the model
T	thrust
U_∞	free-stream velocity
u	streamwise velocity
$u_{x'}$	velocity in $x'-$direction
v	spanwise velocity
$v_{y'}$	velocity in $y'-$direction

w	vertical velocity
x, y, z	cartesian coordinate in the streamwise, spanwise and vertical direction, respectively
x'	the direction pointing upward lied on the disk plane
y'	the direction of counter-clockwise rotation of the blade

Greek Symbols

α	angle of attack
θ	pitch angle of the blade
μ	advance ratio
ν	kinematic viscosity
ρ	density of air
σ	solidity of the blade
Ω	angular velocity of the blade
ω_x	streamwise vorticity

Superscripts

$\bar{()}$	mean quantity

Abbreviations

PIV	particle image velocimetry

Chapter 1

Introduction

Living creatures have long evolved through natural selection to cope with the surrounding environment. In particular, aquatic animals have changed their morphology to move efficiently in water (Fish & Lauder, 2006). For example, tubercles on the pectoral flipper of humpback whale enhance the hydrodynamic performance at high angles of attack (Miklosovic *et al.*, 2004, 2007); carapace of some species of the boxfish has low drag coefficients and provides self-correcting trimming forces to swim in smoother trajectories (Bartol *et al.*, 2003, 2005); scales of a shortfin mako are bristled by reversed flow, preventing flow separation (Lang *et al.*, 2014); grooves of scallops increase the lift-to-drag ratio at moderate and high angles of attack (Choi *et al.*, 2012); longitudinal ridges of leatherback turtles improve the hydrodynamic performance depending on swimming modes (Bang *et al.*, 2016). Especially, the humpback whale has been known as one of the most acrobatic whales in spite of its huge size, and it has been suggested that this agility results from the use of large pectoral flippers which have rounded tubercles along the leading edge (Jurasz & Jurasz, 1979; Fish & Battle, 1995). Previous field studies reported that humpback whales exhibit unique feeding behaviours that require tight turnings (Jurasz & Jurasz, 1979; Hain *et al.*, 1982). Because the path radius is inversely proportional to the lift force, increasing the lift force is important to catch prey with unique feeding behaviours (Fish & Battle, 1995; Weihs, 1981). Therefore, many researchers have investigated the

relationship between the leading-edge tubercles and lift force.

1.1 Previous studies

Previous studies on the effects of leading-edge tubercles on the hydrodynamic (or aerodynamic) performance may be categorized into two types depending on the wing (or airfoil) models used, namely two-dimensional (2D) airfoil vs. three-dimensional (3D) wing. Studies on 2D airfoils, which were conducted at Re = 50,000 - 450,000, showed that hydrodynamic performances of 2D airfoils with leading-edge tubercles are better than those without tubercles only in the post-stall region but worse before stall (Miklosovic *et al.*, 2007; Johari *et al.*, 2007; Hansen *et al.*, 2011; Zhang *et al.*, 2013, 2014; Cai *et al.*, 2015; Custodio *et al.*, 2015; New *et al.*, 2015). Studies using 3D wing models, however, showed various results depending on the wing planform geometry and Reynolds number. In the case of an idealized humpback whale flipper model which imitated a real humpback-whale pectoral flipper and had a back-swept planform geometry, leading-edge tubercles delay the stall, increase the maximum lift coefficient, and increase the lift and decrease the drag in the post-stall region at Re = 505,000 - 631,000 (Miklosovic *et al.*, 2004, 2007). Stanway (2008), who conducted experiments using a slightly modified humpback-whale flipper model with a lower aspect ratio at Re = 44,648 - 119,060, reported that leading-edge tubercles delay the stall for all Reynolds numbers considered, but increase the maximum lift coefficient only at the highest Reynolds number of Re = 119,060. Bolzon *et al* (2017a) considered a back-swept wing model with a sweep angle of 35° and a taper ratio of 0.4 at Re = 225,000. They reported that tubercles on the leading edge little change the stall phenomenon, but decrease the lift for all angles of attack (0° - 20°) and the drag at low angles of attack

(0° - 8°). In addition, they suggested based on velocity measurements in the wake that spanwise locations corresponding to the troughs have local maximum profile drag and minimum induced drag, but those corresponding to the peaks have the opposite result (see also Bolzon *et al* 2016). Bolzon *et al* (2017b) also considered an untapered back-swept wing model with the same sweep angle, and showed that the lift and drag are little changed by single tubercle located at the wing tip. Wei *et al* (2018a) investigated two different back-swept wing models with a sweep angle of 30° and a taper ratio of 0.33 at Re = 220,000. In one model tubercles are aligned with the freestream direction, but in the other they are normal to the leading edge. They showed that the tubercles delay the stall but decrease the lift before the stall for both models, but the maximum lift coefficient increases only for the latter model. On the other hand, for the first model, the lift increases for all angles of attack at a lower Reynolds number of Re = 55,000 (Wei *et al* 2018b). Researches have been also conducted for unswept wings. Weber *et al* (2010) experimentally investigated the effects of leading-edge tubercles on the hydrodynamic performance of unswept rudders with low aspect ratio of 1.6 and tapered ratio of 0.67 at Re = 200,000 - 880,000. They suggested that there exists a critical Reynolds number of Re = 800,000 above which the effects of leading-edge tubercles disappear. Guerreiro and Sousa (2012) measured forces on unswept finite wing models with low aspect ratios of 1 and 1.5 at Re = 70,000 and 140,000. They showed that leading-edge tubercles increase the lift in the post-stall region at Re = 140,000 when tubercle amplitude and wavelength are properly selected, otherwise the lift is unchanged or decreases for all angles of attack considered. On the other hand, tubercles have favourable effects even at low angles of attack for Re = 70,000. Yoon *et al* (2011) conducted RANS simulations for an unswept finite wing model with a low aspect ratio of 1.5 at Re = 1,000,000. They investigated

the effect of R_w (ratio of span length with tubercles to whole span length) on the wing performance. For $R_w \geq 0.4$, leading-edge tubercles are effective in increasing the lift coefficient in the post-stall region.

Previous studies on 2D airfoils suggested that streamwise vortices play a major role in improving the hydrodynamic performance in the post-stall region (Hansen *et al.*, 2011; Favier *et al.*, 2012; Zhang *et al.*, 2014; Rostamzadeh *et al.*, 2014; Cai *et al.*, 2015; New *et al.*, 2015; Hansen *et al.*, 2016; Rostamzadeh *et al.*, 2016; Pérez-Torró & Kim, 2017). There are, however, disagreements about the mechanisms how the streamwise vortices are generated by tubercles and act on the flow field. Favier *et al* (2012) conducted direct numerical simulation at very low Reynolds number of $Re = 800$, and proposed that spanwise variation of the streamwise velocity induces the Kelvin-Helmholtz instability and produces the surface-normal vorticity near the leading edge, which in turn changes into streamwise vortex delaying flow separation. Rostamzadeh *et al* (2014) conducted both numerical and experimental studies at Re =120,000, and suggested two mechanisms responsible for the generation of streamwise vortices near the leading edge. The first was the cyclic variation of the circulation along the span due to tubercles, resulting in the spanwise vorticity variation by the Stokes law and leading to the development of counter-rotating streamwise vortices. The second was the skew-induced vorticity generation in which the spanwise vorticity in the boundary layer tilts into the streamwise and wall-normal directions due to flow skewness near the leading edge. Moreover, additional streamwise vortices were generated from separation bubbles behind the leading edge and separated flow regions near the trailing edge along trough planes. These streamwise vortices were responsible for the formation of attached flow by transporting high momentum fluid into near-wall region. Hansen *et al* (2016) also conducted both numerical and experimental studies at a low Reynolds number of Re =

2,230, and they found that the circulation of streamwise vortices increases as they travel downstream because of continued influx of vorticity from separating shear layer near the trailing edge, which is similar to the leading edge vortex of delta wing. Pérez-Torró & Kim (2017) investigated flow over a deep-stalled airfoil using large eddy simulation at Re = 120,000. They suggested that streamwise vortices evolving from laminar separation bubbles (LSBs) behind the troughs prevent adjacent fully separated shear layers from penetrating into LSBs, resulting in attached flow behind LSBs and contributing to higher lift generation.

Previous studies on 3D wing models also suggested that streamwise vortices play a major role in enhancing the hydrodynamic performance. Pedro and Kobayashi (2008) conducted a detached eddy simulation of flow around the idealized humpback whale flipper model of Miklosovic *et al* (2007) at Re = 500,000. They reported that streamwise vortices generated from leading-edge tubercles provide high momentum to near-wall region and delay the trailing edge separation. Moreover, flow separation near the leading edge was confined only in the tip region by tubercles. Stanway (2008) suggested that streamwise vortices generated near the leading edge are the key structure to delay the stall angle, and they are similar to leading edge vortices of the delta wing which generate additional lift at high angles of attack. Weber *et al* (2011) conducted RANS simulations for an idealized humpback whale flipper model at the same Reynolds number as that of Miklosovic *et al* (2004), and suggested that leading-edge tubercles play a role similar to that of a delta wing and generate streamwise vortices, producing a net downwash at the spanwise locations of tubercle peaks and resulting in separation delay. Bolzon *et al* (2016) also suggested that asymmetric (due to swept angle) counter-rotating streamwise vortex pairs induce downwash and attach flow behind the peaks, but they in-

duce upwash and bring early separation behind the troughs. Wei *et al* (2018a) showed through surface-oil-flow visualizations that counter-rotating streamwise vortices evolve from laminar separation bubbles behind the troughs and delay flow separation. These flow structures also prevented large-scale recirculation observed near the mid-span.

Other flow structures beside the streamwise vortices have also been suggested. Skillen *et al* (2015) simulated flow over a 2D airfoil at Re = 120,000. They suggested that leading-edge tubercles locally induce a spanwise pressure gradient driving low-inertia near-wall fluid toward trough regions. As a result, high momentum fluid was attracted to peak regions and reenergized the boundary layer, resulting in separation delay. van Nierop *et al* (2008) proposed an aerodynamic model predicting main features of the gradual stall phenomenon, and explained that nonuniform downwash which is larger at peak planes than trough planes results in a lower effective attack angle at peak planes and delays flow separation. Serson *et al* (2017) conducted direct numerical simulations for an infinite wing with spanwise waviness at Re = 10,000 and 50,000. They showed that wavy leading edge produces weaker adverse pressure gradient behind peaks, resulting in attached flow there, and early transition behind troughs also reattaches flow and increases the lift.

1.2 Objectives

As described chapter 1.1, most of previous experimental studies have suggested the flow structures, responsible for the stall delay and lift and drag variations by tubercles, as symmetric or asymmetric counter-rotating streamwise vortices behind the tubercles. These structures had been observed in the wake behind back-swept wings at the pre-stall angles of $0° \leq \alpha \leq 12°$ by measuring

mean flow fields on a cross-flow plane in the wake using a velocity measurement probe (Bolzon *et al.*, 2016, 2017a, b). Other studies conducted oil-flow visualizations on the suction surfaces (Wei *et al.*, 2018a, b), and PIV measurements on a surface-parallel 2D plane above the suction surface (Stanway, 2008) at the pre-stall, stall and post-stall angles of attack, from which they indicated the existence and evolution of counter-rotating vortices above the suction surface. However, modifications of overall flow feature on the suction side by tubercles for a wide range of the angle of attack have not been deeply investigated yet. For example, how the counter-rotating vortical structures evolve and how the tip and root vortices affect the flow structures as the angle of attack increases are not yet clearly explained. Therefore, to answer these questions, we conduct experiments on the idealized (swept and tapered) wing models with and without tubercles devised by Miklosovic *et al* (2007). We measure the drag and lift forces on both models by varying the angle of attack from 0° to 25° at Re = 180,000. To investigate how leading-edge tubercles change the flow fields and affect the hydrodynamic performance, surface-oil-flow visualization, and surface pressure and 2D-PIV measurements (on several streamwise and cross-flow 2D planes) are performed at four different angles of attack of 4°, 9°, 13° and 16°. The experimental setup is described in chapter 2. The results from force measurements and the flow characteristics around both models are in detail discussed in chapter 3. Further discussions on the roles of tubercles for 3D wings are provided in chapter 4 and application to a quadrotor blade is discussed in chapter 5, followed by conclusions in chapter 6.

Chapter 2

Experimental Set-up

To investigate the effect of the leading edge tubercles, three-dimensional wing models with and without tubercles are constructed as same as those used in Miklosovic *et al* (2007). The lift and drag forces on both models are measured using two force sensors. The flow characteristics near both models are obtained using a two-dimensional particle image velocimetry (2D-PIV), a pressure measurement and a surface-oil-flow visualization. Three-dimensonal flipper models used in the present study are described in chapter 2.1. Experimental set-up for the force measurement is provided in chapter 2.2. Detailed descriptions of the 2D-PIV measurement, surface pressure measurement, and surface-oil-flow visualization are given in chapter 2.3, chapter 2.4, and chapter 2.5, respectively.

2.1 Wing model

Figure 2.1 shows planform views of the present wing models. They are designed using the procedure outlined in previous study (Miklosovic *et al.*, 2007) and made of acrylonitrile butadiene styrene (ABS) resin. They have the NACA 0020 cross-section, a mean chord length of $\bar{c} = 129$ mm, a span length of $s = 571.5$ mm, and planform area of $A = 737$ cm^2. The blockage ratio is 3.85% at the maximum angle of attack considered ($\alpha = 25°$) which is less than the minimum value (7.5%) recommended to avoid disturbances from the wind-tunnel wall

(Barlow *et al.*, 1999). The surfaces of wing models are coated with matt black to reduce laser reflection and sanded with progressively finer sandpaper down to 600 grit to have smooth surfaces. The wing models without and with leading-edge tubercles are named as base and tubercle models, respectively. For the tubercle model, all tubercle peaks and troughs are numbered from 1 to 7 (from the root to the tip; see figure 2.1). Same spanwise locations are also marked for the base model for comparison. Note that the tubercle model does not have tubercles near the wing root region as in Miklosovic *et al* (2007).

2.2 Force measurement

Figure 2.2 shows the schematic diagram of the force measurement. To minimize the effect of the incoming boundary layer from the wind tunnel floor, an end plate is installed at the test section. The leading edge of the end plate is shaped into a half ellipse with a ratio of major to minor axis of 2. To reduce leakage flow, the wing models are mounted within 2 mm from the upper surface of end plate, which is within the range of the suggested maximum gap of 0.005 $\times$ model span length (Barlow *et al.*, 1999). The lift (L) and drag (D) forces on the wing models are measured with force sensors (AND LCB03 series) which are attached to the supporter assembled with the models. Signals from the force sensor are sampled for 60 s at a rate of 10 kHz to obtain a fully converged mean force and digitized by the A/D converter (NI PCI-6259). The lift (C_L) and drag (C_D) coefficients are defined as $C_L = L/(0.5\rho U_\infty^2 A)$ and $C_D = D/(0.5\rho U_\infty^2 A)$, respectively, where ρ is the air density and U_∞ is the free-stream velocity. The force measurements are conducted at $Re = U_\infty \bar{c}/\nu = 180,000$, where ν is the kinematic viscosity of air. The angle of attack is varied from 0° to 25° by increments of 1°. Using the method in Coleman and Steele (2009), uncertainties

of the measured lift and drag coefficients are estimated to be less than 2.5%.

2.3 Particle image velocimetry

The velocity fields around the wing models are measured using a 2D-PIV system shown in figure 2.3. The 2D-PIV system consists of a fog generator (SAFEX), a double-pulsed Nd:YAG laser (Litron Lasers) operating at 135 mJ, a CCD camera (Vieworks VH-4M) with a 2,048 pixel $\times$ 2,048 pixel resolution, and a timing hub (Integrated Design Tools). The fog generator produces liquid droplets having a mean diameter of 1 μm, which are introduced into the wind tunnel. Laser and laser optics make laser sheets having a thickness of 2 mm, which illuminate the planes of interest. The x, y, z denote the streamwise, spanwise and vertical directions, respectively. The origin is located $0.48\bar{c}$ downstream from the leading edge of the root plane along the chord line. The velocity measurements are performed on several streamwise $(x-z)$ planes indicated as black solid and blue dashed lines in figure 2.1, and on crossflow $(y-z)$ planes. An iterative cross-correlation analysis is implemented with an initial interrogation window size of 64 pixel $\times$ 64 pixel and a final interrogation window size of 32 pixel $\times$ 32 pixel. The interrogation window is overlapped by 50%, leading to spatial resolutions of $0.0086c_l$ (c_l: local chord length) on the $x-z$ plane and $0.0048\bar{c}$ on the $y-z$ plane. For selected $y-z$ planes in the pre-stall region, a 2D-PIV is conducted using a reduced field of view. In this case, a final interrogation window size is 16 pixel $\times$ 16 pixel and overlapped by 50%, leading to a spatial resolution of $0.00085\bar{c}$. One thousand pairs of images are taken to obtain the time-averaged flow field. The uncertainties of velocity and vorticity are estimated to be less than 5.8% and 6.4%, respectively (Willert & Gharib, 1991; Fouras & Soria, 1998; Raffel *et al.*, 2013).

2.4 Surface pressure measurement

To measure the pressure on the suction surfaces of wing models, we install a total number of 45 pressure taps along the chordwise direction from the leading edge (0 to $0.6c_l$ with increments of $0.05c_l$, $0.7c_l$ and $0.8c_l$) at three spanwise locations of P2, T3 and P3 for the base and tubercle models, respectively (see red dots in figure 2.1). Pressure tabs are connected to a digital manometer (MKS-220DD) having a measurement range of 0-100 Torr. Signals from the digital manometer are sampled for 40 s at a rate of 10 kHz to obtain a fully converged mean surface pressure and digitized by the A/D converter (NI PCI-6259). The pressure coefficient is defined as $C_P = (P - P_\infty)/(0.5\rho U_\infty^2)$, where P is the time-averaged surface pressure and P_∞ is the static pressure at the free-stream.

2.5 Surface-oil-flow visualization

Surface-oil-flow visualizations are also conducted using a mixture of oil and white dye to obtain flow patterns on the suction surfaces. For the visualization, the wing models are installed horizontally to reduce the oil movement by gravity. Photographs are taken after $180s$ to obtain images of fully evolved surface-oil-flow patterns. Videos are also taken to analyse the oil movement in time.

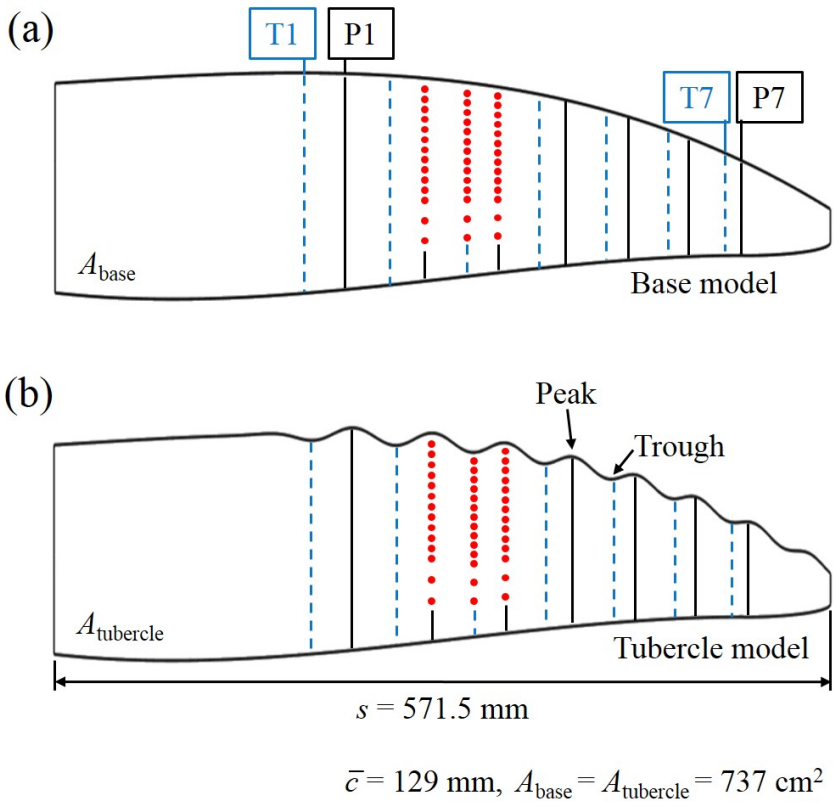

Figure 2.1. Planform views of the wing models. (a) Base model; (b) Tubercle model. Here, black solid and blue dashed lines denote spanwise locations of peaks and troughs, respectively. Red dots denote locations of pressure tabs.

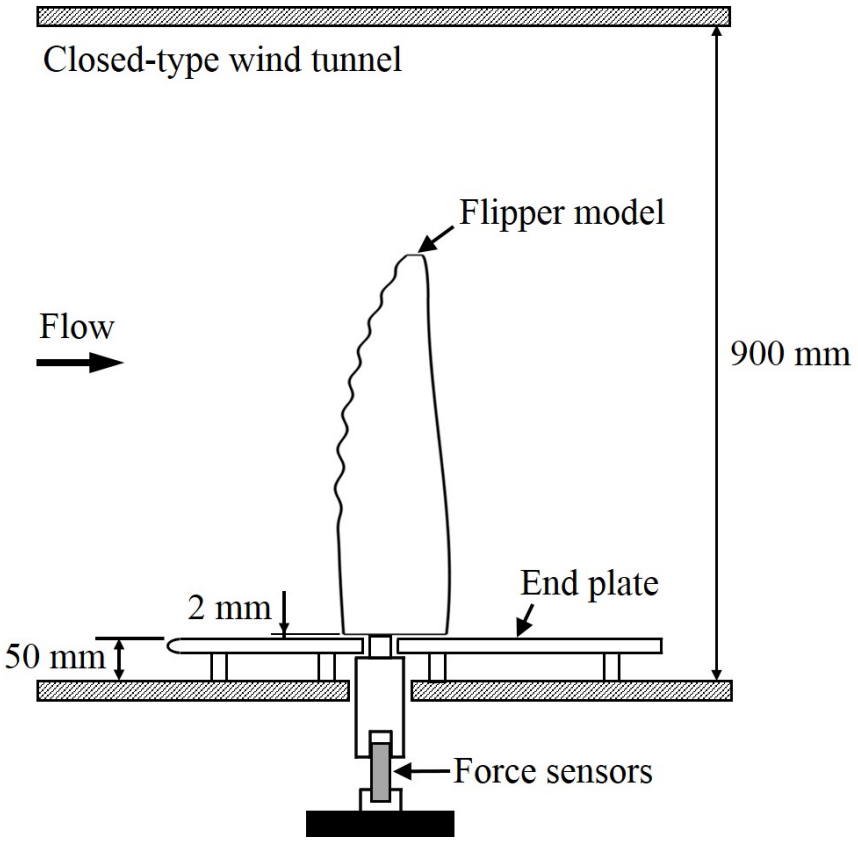

Figure 2.2. Schematic diagram of the experimental set-up for the force measurement.

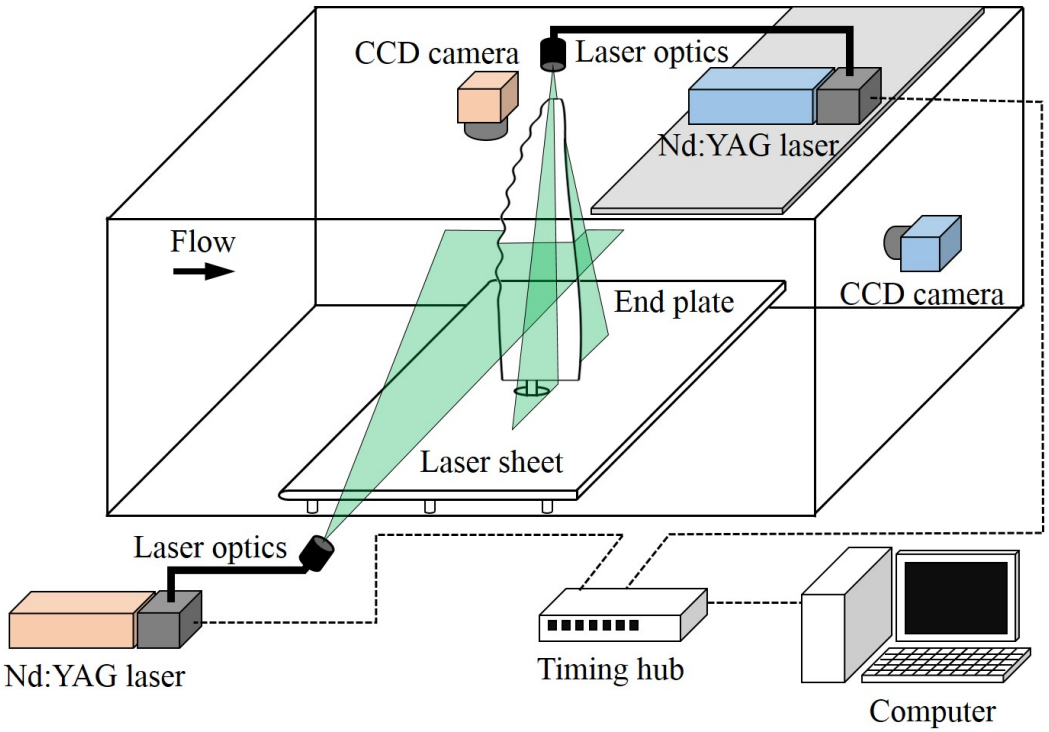

Figure 2.3. Schematic diagram of the experimental set-up for the two-dimensional PIV measurement (2D-PIV).

Chapter 3

Results and Discussion

3.1 Aerodynamic forces

Figures 3.1 - 3.3 show the variations of the lift and drag coefficients and lift-to-drag ratio with the angle of attack for the base and tubercle models at Re = 180,000, together with the results of Miklosovic *et al* (2004) at Re = 505,000 - 520,000. The lift coefficients of both models linearly increase until $\alpha = 7^\circ$ but with slightly different slopes ($dC_L/d\alpha$ = 4.87 and 4.58 for the base and tubercle models, respectively). This difference in the slopes was not observed in Miklosovic *et al* (2004) but was reported in Stanway (2008) who conducted an experiment at lower Reynolds numbers of Re = 44,648 - 119,060, indicating that the slope difference occurs due to relatively lower Reynolds number considered. The base model stalls at $\alpha = 8^\circ$, at which the maximum lift coefficient is 0.70. With further increase in α, the lift coefficient rapidly decreases, reaches minimum at $\alpha = 13^\circ$ and then increases again. On the other hand, with tubercles, the lift coefficient increases until $\alpha = 11^\circ$, maintains roughly a constant value (0.82 - 0.86) at $11^\circ \leq \alpha \leq 15^\circ$. The stall occurs at $\alpha = 15^\circ$, and then the lift coefficient decreases with increasing α. At $\alpha \geq 23^\circ$, the lift coefficients of both models are the same, indicating that the tubercles do not play any role at these very high angles of attack. The tubercles delay the stall angle by 7° and increase the maximum lift coefficient by about 22%. The

drag coefficient with tubercles is much lower at $9^\circ \leq \alpha \leq 15^\circ$ than that of base model (figure 3.2). The drag coefficients are higher than those of Miklosovic *et al* (2004) due to lower Reynolds number considered in the present study. With tubercles, maximum lift-to-drag ratio occurs at $\alpha = 5^\circ$, whereas it does at $\alpha = 8^\circ$ for the base model (figure 3.3). At higher angles of attack, L/D with tubercles decreases much more slowly and thus is higher than that of base model.

As explained in section 1, the lift characteristics on a tapered back-swept wing model considered by Bolzon *et al* (2017a) were very different from the present ones, probably because the taper ratio of the former study, 0.4, was much bigger than that of the present study (about 0.16). On the other hand, for a cambered back-swept wing model with a larger taper ratio of 0.33 by Wei *et al* (2018a), the lift characteristics are quite similar to the present ones. These results indicated that the taper ratio and camber of 3D wings are important parameters to determine the lift characteristics by tubercles.

3.2 Flow pattern on the suction surface

Figures 3.4 - 3.7 show flow patterns on the suction surfaces of the base and tubercle models using surface-oil-flow visualizations, where the spanwise locations of troughs (T) and peaks (P) are indicated on the top of this figure. Figures 3.8 - 3.10 show enlarged views of separation bubbles existing in the P2 - P3 region (indicated by blue dashed rectangles in figures 3.4 - 3.6) for the tubercle model. For the base model, flow separates and reattaches on the suction surface at $\alpha = 4^\circ$, forming a separation bubble elongated along the spanwise direction ($0.43 \leq y/\bar{c} \leq 4.43$), as shown in figure 3.4(a) (also observed by Bolzon *et al* 2017b, Wei *et al* 2018a, b). On the other hand, in the tubercle model,

complex flow patterns are observed in the downstream of tubercles, while a flow pattern similar to that of the base model is maintained in the spanwise location of smooth leading edge (figure 3.4(b)). Surface-oil-flow pattern in figures 3.4(b) and 3.8 shows hemi-spherical separation bubbles right after tubercle troughs. Inside this separation bubble, counter-rotating foci are observed ($x/\bar{c} \approx$ -0.2) (Wei *et al* 2018a). At a further downstream location ($x/\bar{c} \approx 0.1$), foci with clockwise and counter-clockwise rotating motions are formed at the spanwise locations between peaks and troughs. The discrete distribution of hemi-spherical separation bubbles near the leading edge in the tubercle model is similar to that observed from previous studies on 2D airfoil models (Karthikeyan *et al.*, 2014; Rostamzadeh *et al.*, 2016) and 3D back-swept wing models (Wei *et al* 2018a, b), although the detailed flow patterns are not precisely matched.

As the angle of attack increases to 9° at which the base model already stalls (figure 3.5(a)), the tip region of the base model has flow separation without reattachment, but an elongated separation bubble of smaller streamwise size still exists at $0.37 \leq y/\bar{c} \leq 3.13$ and further upstream location. Between these two flow regions (i.e., around $y/\bar{c} = 3.13$), a focus with a counter-clockwise rotating motion exists, also denoted as large-scale recirculating region by Wei *et al* (2018a, b). Moreover, a thin separation bubble (indicated by white line) is newly observed closer to the leading edge at $2.71 \leq y/\bar{c} \leq 4.43$. For the tubercle model (figures 3.5(b) and 3.9), flow separation without reattachment occurs very near the tip region due to its low local Reynolds number (Diebold, 2012; Wei *et al.*, 2018), and the focus with a counter-clockwise rotating motion, observed for the base model, occurs near the tip region (at $y/\bar{c} \approx 4$). On the other hand, flow pattern behind smooth leading edge is similar to that of the base model. At $1.28 \leq y/\bar{c} \leq 3.95$, hemi-spherical separation bubbles behind the trough become much weaker and smaller and locate further upstream than

those for $\alpha = 4°$, and foci located at the spanwise locations between the peaks and troughs are also much weaker. In addition, flow separates weakly near the trailing edge at the spanwise locations of troughs (figure 3.9), which is consistent with the observation made by previous studies (Johari *et al.*, 2007; Hansen *et al.*, 2011; Rostamzadeh *et al.*, 2014; Hansen *et al.*, 2016; Bolzon *et al.*, 2017).

At $\alpha = 13°$ where the lift coefficient of the base model is minimum (figure 3.6(a)), a thin separation bubble exists near the entire leading edge (thin white line in this figure), and main flow separation occurs afterwards (red dashed line). Figures 3.4(a), 3.5(a) and 3.6(a) clearly indicate that flow separation progresses inboard (i.e., tip to root) as the angle of attack increases (see also Pedro & Kobayashi 2008, Wei *et al* 2018a, b). In the tubercle model (figure 3.6(b)), the separated region near the tip becomes wider than that at $\alpha = 9°$ but is still confined to the outboard. The focus with a counter-clockwise rotating motion becomes stronger than that at $\alpha = 9°$ and occupies wider space at $y/\bar{c} \approx 3.5$. Separation bubble still exists behind smooth leading edge but its streamwise size becomes smaller. Near the trailing edge behind troughs (T1-T4), λ-shaped flow patterns exist, each of which consists of large and small foci with clockwise and counter-clockwise rotating motions, respectively (figure 3.5(a)). These flow patterns near the trailing edge differ from the delta- or horseshoe-shaped patterns (quasi-symmetric foci with counter-rotating motions) observed from 2D airfoil models (Rostamzadeh *et al.*, 2014; Hansen *et al.*, 2016).

At $\alpha = 16°$ where the tubercle model already stalls, main separation occurs outboard ($y/\bar{c} \geq 3.1$) and inboard ($y/\bar{c} \leq 1.6$), and foci with counter-clockwise and clockwise rotating motions exist in between. In addition, hemi-spherical separation bubbles are still observed downstream of troughs (T2-T5), and the λ-shaped flow patterns near the trailing edge now disappear. As illustrated in figures 3.4 - 3.10, the hemi-spherical separation bubbles after troughs and

λ-shaped surface flow patterns near the trailing edge are the key flow structures of separation delay by tubercles, which are examined from surface pressure and velocity measurements in the following sections.

3.3 Chordwise pressure distribution

Figures 3.11 and 3.12 show the distributions of the surface pressure coefficient at three spanwise locations of P2, T3 and P3 for the base and tubercle models. At $\alpha = 4^\circ$ (figure 3.11), the surface pressure coefficients of the base model at three spanwise locations are not very different among themselves. The tubercle model, however, shows very different pressure distributions from those of the base model. The peak magnitude of C_p on the suction surface at the trough T3 is higher than that at the same spanwise location of the base model, while the peak magnitudes at the peaks P2 and P3 are lower than those of the base model. As a result, there is a strong chordwise adverse pressure gradient on the suction surface behind the trough, inducing early flow separation, whereas weaker chordwise adverse pressure gradient is formed behind the peak and thus flow is attached there. Therefore, a hemi-spherical separation bubble is formed behind each trough, as shown in surface-oil-flow visualization (figures 3.4(b) and 3.8). At $\alpha = 13^\circ$ (figure 3.12), the pressure coefficient on the suction surface of the base model is almost flat in the chordwise direction because the flow already fully separates from the suction surface. For the tubercle model, however, the peak magnitudes of C_p on the suction surface at three spanwise locations are higher than those of the base model because of the separation delay, and strongest adverse pressure gradient is formed in the downstream of the trough T3, which induces strong λ-shaped flow patterns near the trailing edge (figure 3.10) and nearly flat pressure distribution at $x/\bar{c} \geq 0.2$.

3.4 Flow field around the wing model

Figure 3.13 shows the contours of the instantaneous streamwise vorticity and cross-flow velocity vectors on y-z planes near the trough T3 at three different streamwise locations for the tubercle model at $\alpha = 4°$. Since flow structures are not clearly visible due to strong attached flow toward the surface, Galilean transformation, adding $w/U_\infty = 0.12$ and 0.2 to the flow fields at $x/\bar{c} = 0.1$ and 0.33, respectively, is performed to better identify flow structures (see, e.g., Adrian *et al* 2000). At $x/\bar{c}$ = -0.2 (figure 3.13(a)), the flow within the hemi-spherical separation bubble does not show distinct flow characteristics but upward flow. At $x/\bar{c} = 0.1$ (figure 3.13(b)), a counter-rotating streamwise vortex pair evolve from counter-rotating foci inside the hemi-spherical separation bubble. Rostamzadeh *et al* (2014) observed a similar flow pattern from a 2D airfoil model with tubercles, and Hosseinverdi *et al* (2015) also found that a streamwise vortex pair evolve from a hemi-spherical separation bubble on a flat plate. As this streamwise vortex pair travel downstream, they move upward due to self-induced motion. An example of such vortex pair is shown in a red dashed box in figure 3.13(c). Counter-clockwise and clockwise rotating streamwise vortices observed at $y/\bar{c} \approx 2.3$ and 2.5, respectively, evolve from left and right foci at $x/\bar{c} \approx 0.1$ (figure 3.8).

Figures 3.14 - 3.17 show the contours of the mean streamwise velocity and velocity vectors for the base and tubercle models at $\alpha = 9°$ where the base model already stalls. For the base model, flow separation occurs on P5 − P7 planes. Note that separation-reattachment near the leading edge on P4 − P7 planes observed from surface-oil-flow visualization is not measured by PIV owing to low PIV resolution near the surface. For the tubercle model, flow is fully attached on P4 − P6 planes and reversal flow is observed near the trailing edge

of P7 plane, which is consistent with the results of surface-oil-flow visualization (figure 3.5(b)). Therefore, flow separation is significantly delayed by tubercles. Figure 3.18 shows the contours of the instantaneous streamwise vorticity and cross-flow velocity vectors near the trailing edge (at $x/\bar{c} = 0.4$) after Galilean transformation (adding $v/U_\infty = 0.1$ and $w/U_\infty = 0.12$ to instantaneous flow fields). Note that the flow fields shown here are measured at different instants owing to the limitation of the size of the field of view. Counter-rotating streamwise vortex pairs are observed in between peak and trough of tubercles, which evolve from foci inside hemi-spherical separation bubbles near the leading edge as observed at $\alpha = 4^\circ$. These streamwise vortex pairs prevent the spanwise progression of flow separation from tip to root and delay flow separation at $3.13 \leq y/\bar{c} \leq 3.95$. However, the prevention of spanwise progression was not observed in Wei *et al* (2018a, b). Due to this difference, the stall delay by tubercles is larger for the present model than for the back-swept wing models in Wei *et al* (2018a, b).

Figures 3.19 - 3.23 show the contours of mean streamwise velocity and velocity vectors for the base and tubercle models at $\alpha = 13^\circ$ where the base model has minimum lift coefficient. In the case of base model, massive flow separation occurs at all spanwise locations. For the tubercle model, flow is attached on most of suction surface. Massive flow separation is observed only on P6 plane (figure 3.23), and flow separation occurs near the trailing edge only in the downstream locations of troughs (figures 3.19 and 3.21). Figure 3.24 shows the contours of the instantaneous streamwise vorticity and cross-flow velocity vectors on cross-flow planes at three different streamwise locations for the tubercle model at $\alpha = 13^\circ$. Here, the velocity vectors at $x/\bar{c} = -0.07$ are modified through the Galilean transformation by adding $w/U_\infty = 0.17$, to better identify streamwise vortices. At $x/\bar{c} = -0.07$, a counter-rotating streamwise vortex pair

appear, similar to those shown at $\alpha = 4^\circ$ (figure 3.13(b)), which evolve from the hemi-spherical separation bubble in the upstream location. At $x/\bar{c} = 0.25$ (figure 3.24(b)), a pair of streamwise vortices are observed further away from the surface due to mutual induced motion. Other counter-clockwise and clockwise rotating vortices are found very near the surface (at $y/\bar{c} \approx 2.3$ and 2.45), which evolve from the upstream foci in the separated flow region ($2.28 \leq y/\bar{c} \leq 2.46$). At $x/\bar{c} = 0.56$ (figure 3.24(c)), streamwise vortices with positive and negative vorticity exist. However, the vortex with negative vorticity is stronger than that with positive vorticity, because the focus with clockwise rotation is stronger than the focus with counter-clockwise rotation (figure 3.10). Hence, the vortex with positive vorticity moves upward due to the induced flow by the vortex with negative vorticity. It is interesting to note that dominant vortical structure changes from the vortex with positive vorticity to that with negative vorticity as they approach the trailing edge, which is very different from a quasi-symmetric streamwise vortex pair found for 2D airfoil models (Rostamzadeh *et al.*, 2014; Hansen *et al.*, 2016). These vortical structures delay the stall by suppressing flow separation behind the peaks at $\alpha = 13^\circ$.

Figures 3.25 - 3.31 show the flow fields around the tubercle model at $\alpha = 16^\circ$ at which the tubercle model already stalls. At this angle of attack, flow separation occurs near the leading edge on P1 and P5 planes, but flow is attached at other locations (see also figure 3.7(b)). As shown from surface-oil-flow visualization (figure 3.7(b)), foci with clockwise and counter-clockwise rotations exist before the trailing edge. Thus, streamwise vortices with opposite directions of rotation are observed on the cross-flow plane near the trailing edge (figure 12). These two streamwise vortices generate downwash motions towards mid-span surface, resulting in the attached flow there. Although the tubercle model already stalls at this angle of attack, the lift coefficient is still higher than

that of the base model because of the attached flow at the mid-span.

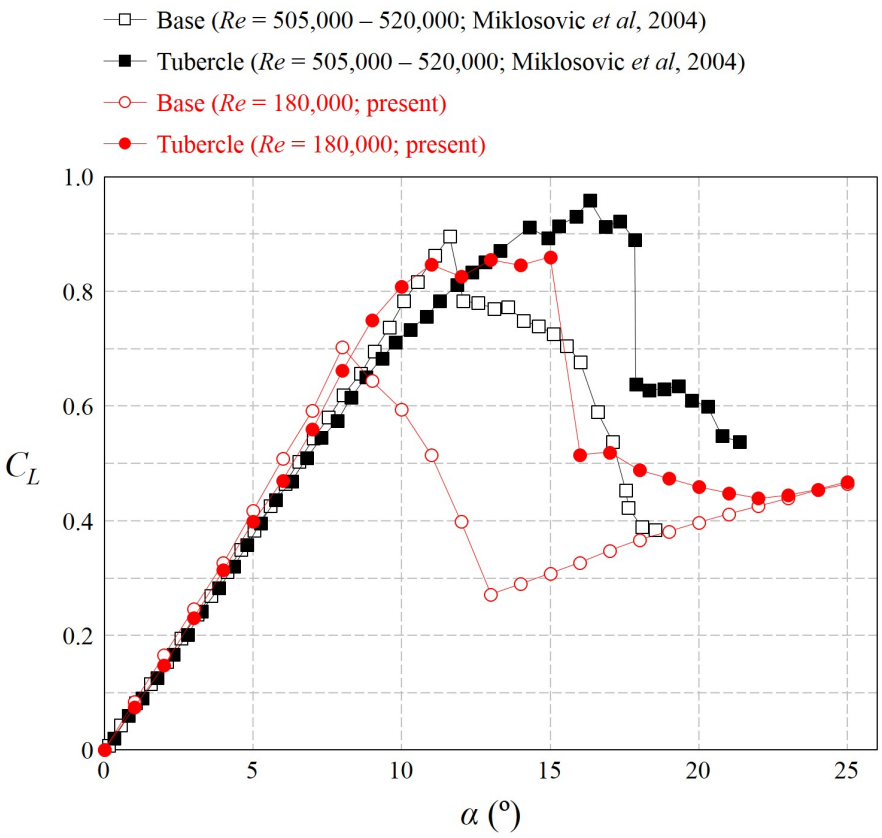

Figure 3.1. Variations of the lift coefficients with the angle of attack for the base and tubercle models at $Re = 180,000$.

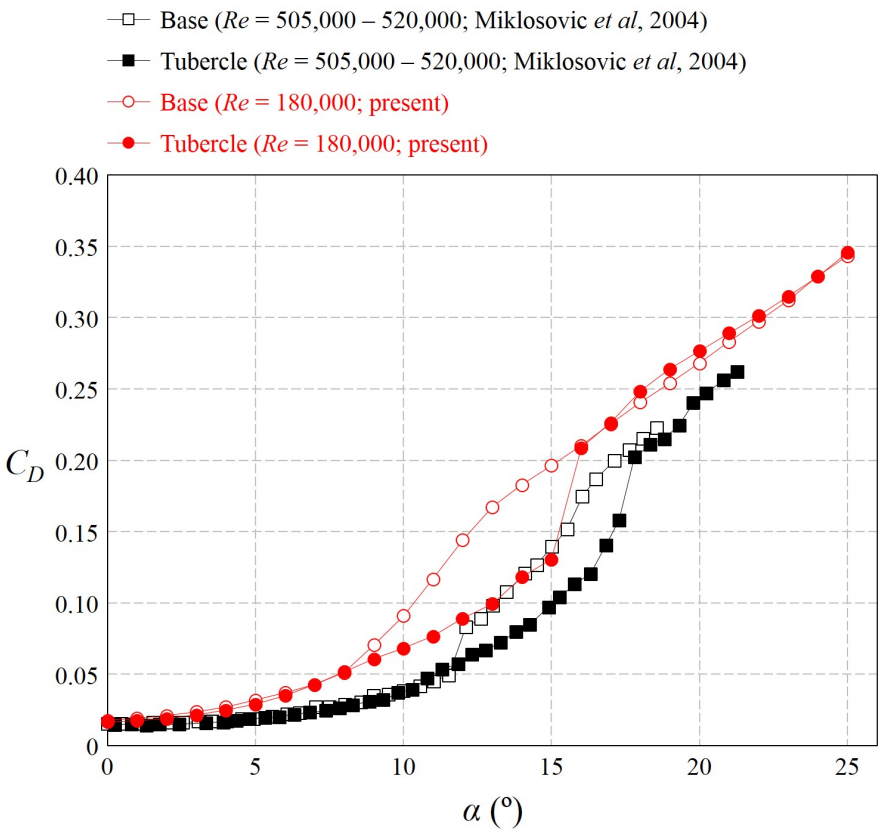

Figure 3.2. Variations of the drag coefficients with the angle of attack for the base and tubercle models at $Re = 180,000$.

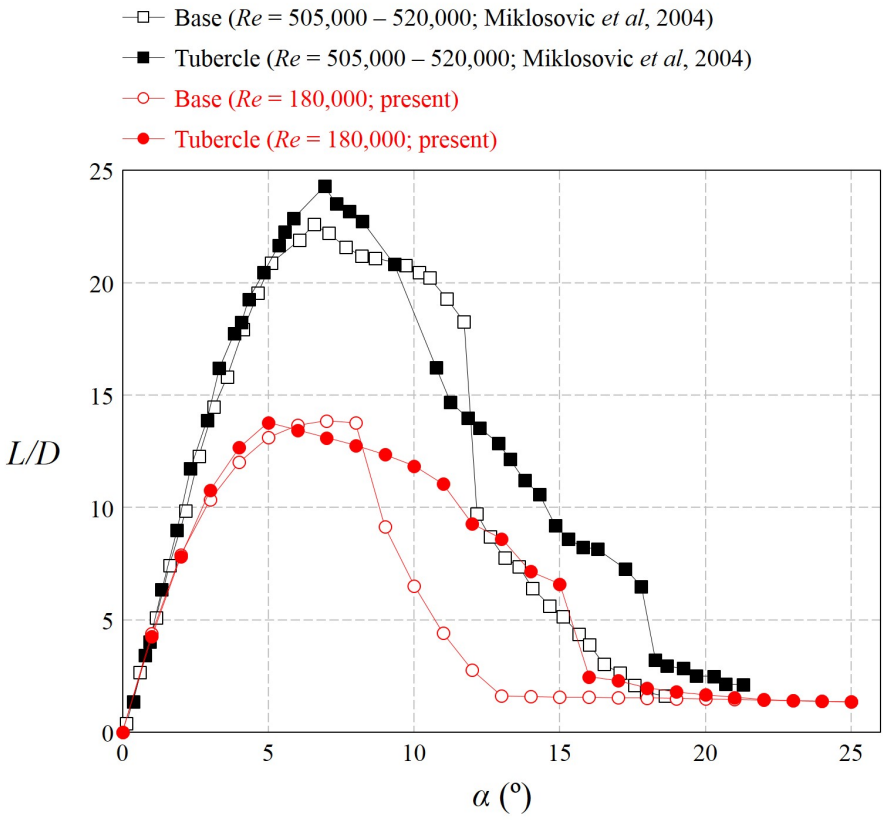

Figure 3.3. Variations of the lift-to-drag ratio (L/D) with the angle of attack for the base and tubercle models at $Re = 180,000$.

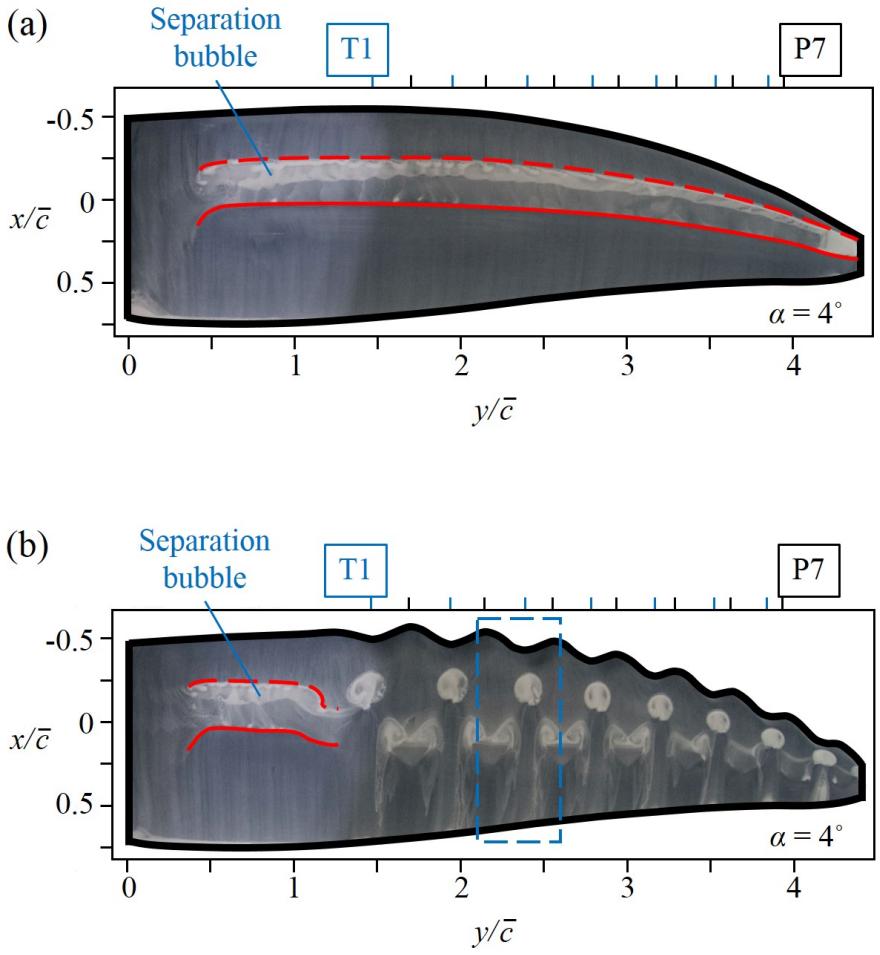

Figure 3.4. Surface-oil-flow visualizations at $\alpha = 4°$: (a) Base model; (b) Tubercle model. The red dashed and solid lines denote the flow separation and reattachment, respectively.

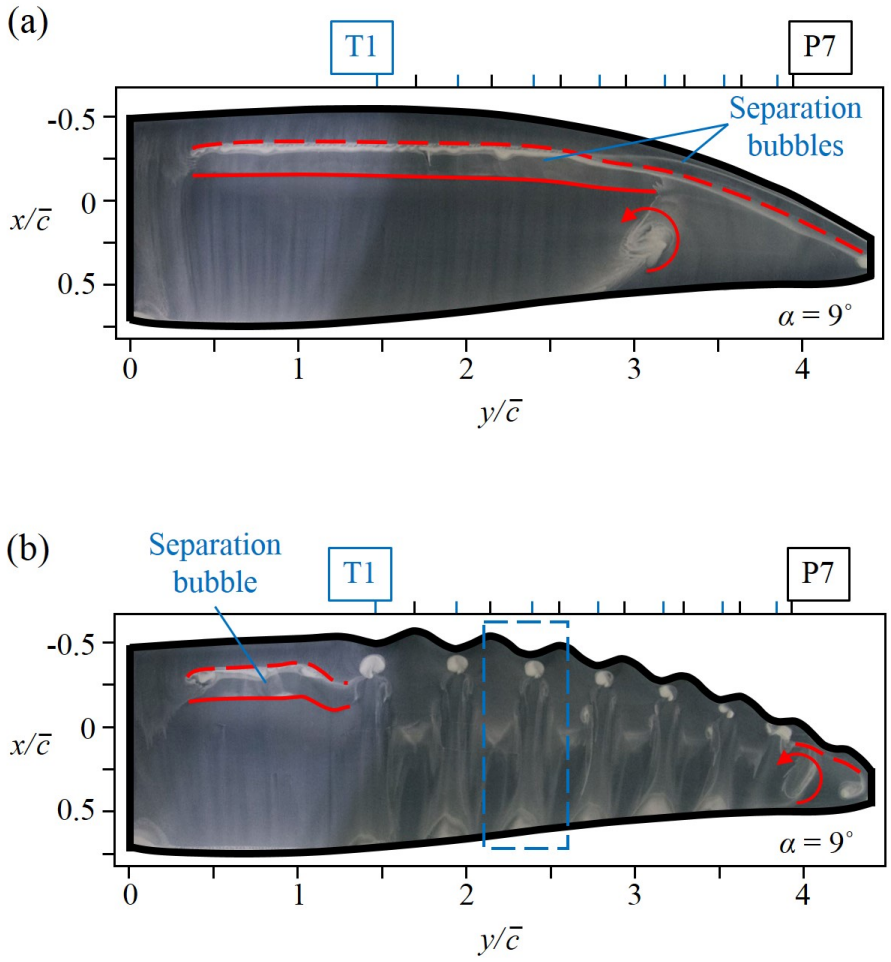

Figure 3.5. Surface-oil-flow visualizations at $\alpha = 9°$: (a) Base model; (b) Tubercle model. The red dashed and solid lines denote the flow separation and reattachment, respectively.

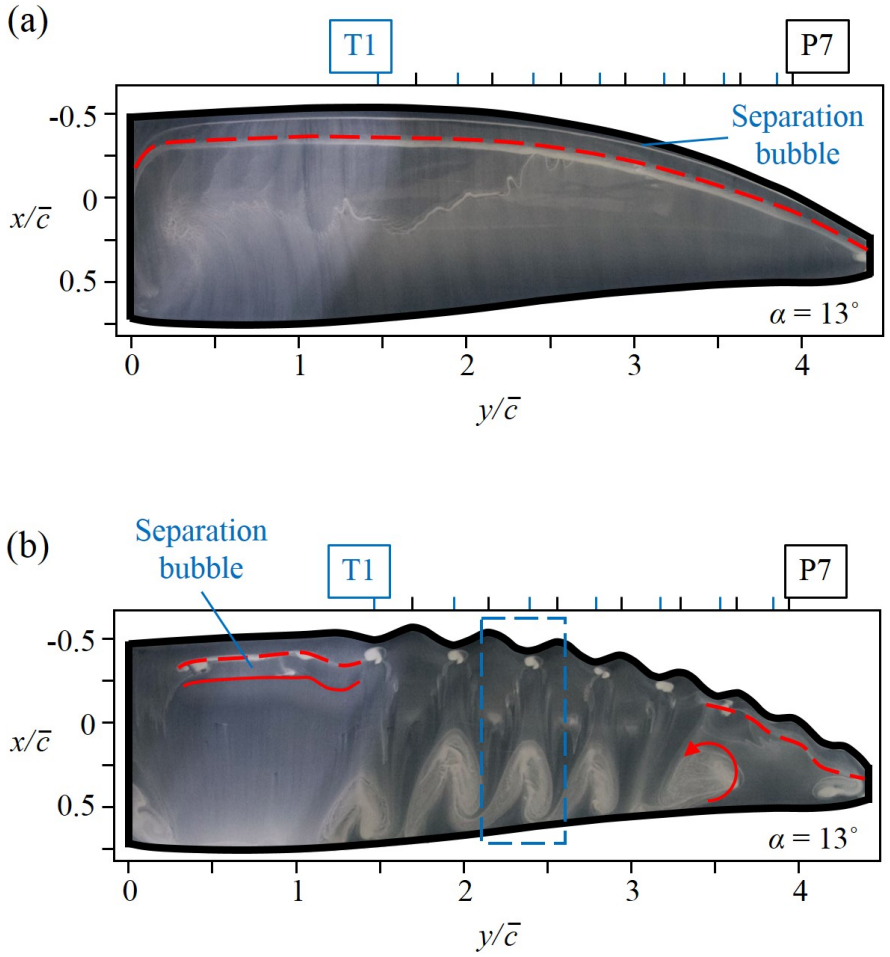

Figure 3.6. Surface-oil-flow visualizations at $\alpha = 13°$: (a) Base model; (b) Tubercle model. The red dashed and solid lines denote the flow separation and reattachment, respectively.

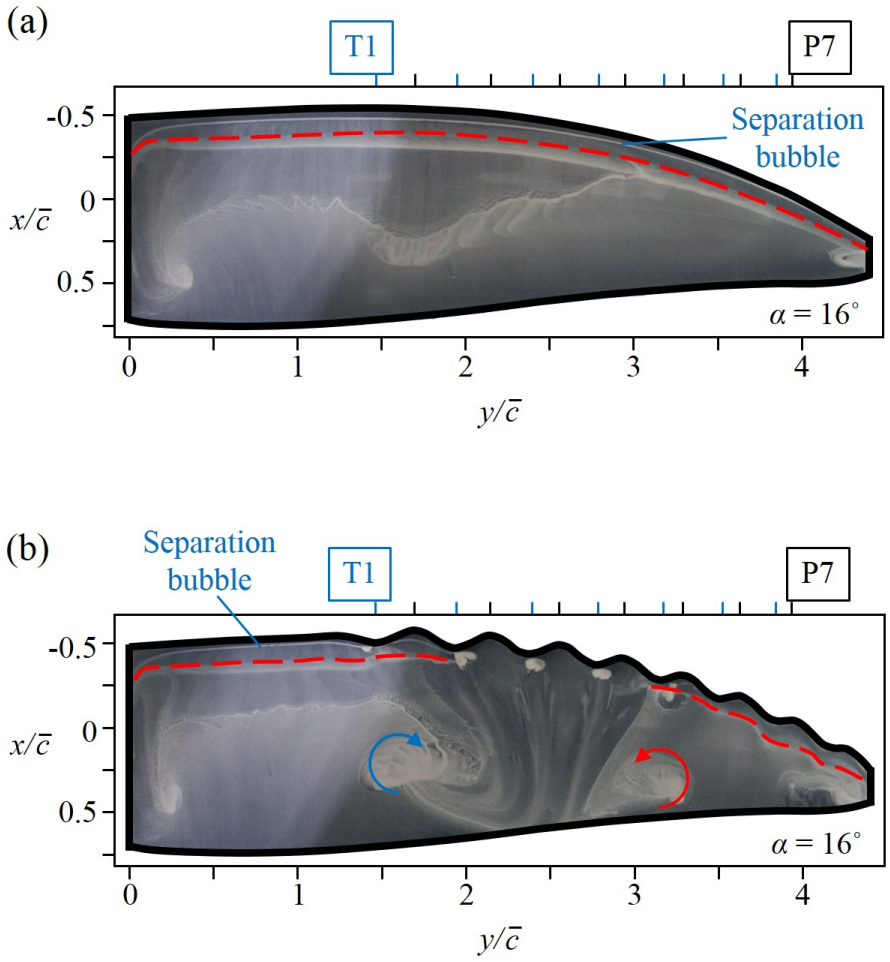

Figure 3.7. Surface-oil-flow visualizations at $\alpha = 16°$: (a) Base model; (b) Tubercle model. The red dashed and solid lines denote the flow separation and reattachment, respectively.

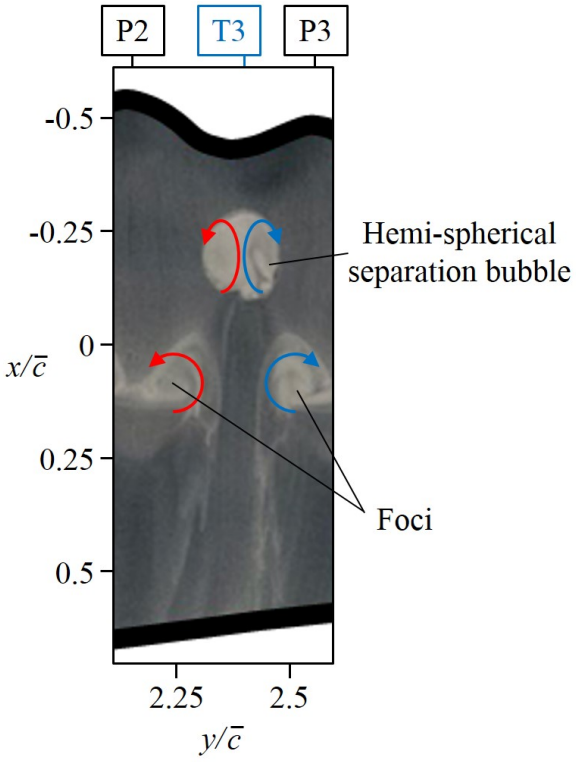

Figure 3.8. Enlarged view of the P2-P3 region for the tubercle model at $\alpha = 4°$. The region is indictaed by the blue dashed rectangles in figure 3.4(b).

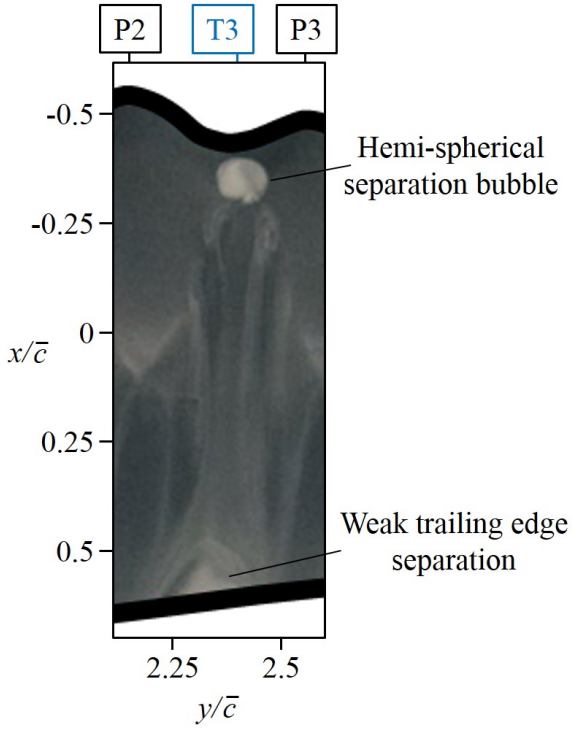

Figure 3.9. Enlarged view of the P2-P3 region for the tubercle model at $\alpha = 9°$. The region is indictaed by the blue dashed rectangles in figure 3.5(b).

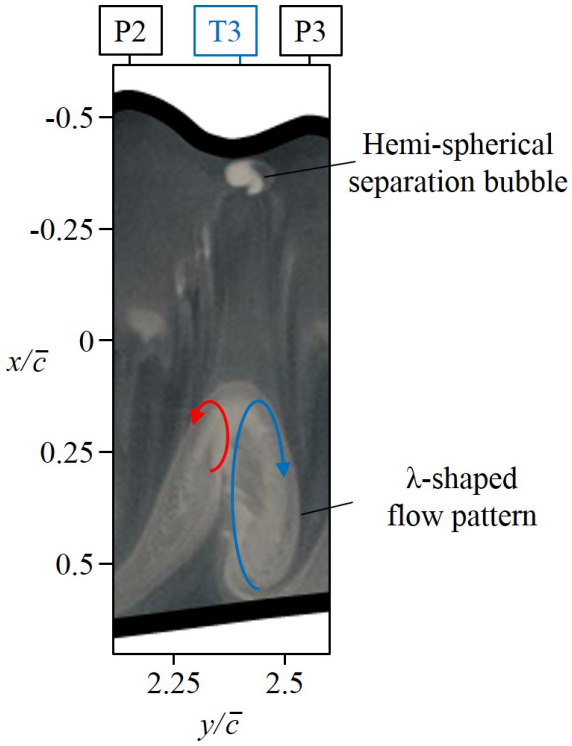

Figure 3.10. Enlarged view of the P2-P3 region for the tubercle model at $\alpha = 13°$. The region is indictaed by the blue dashed rectangles in figure 3.6(b).

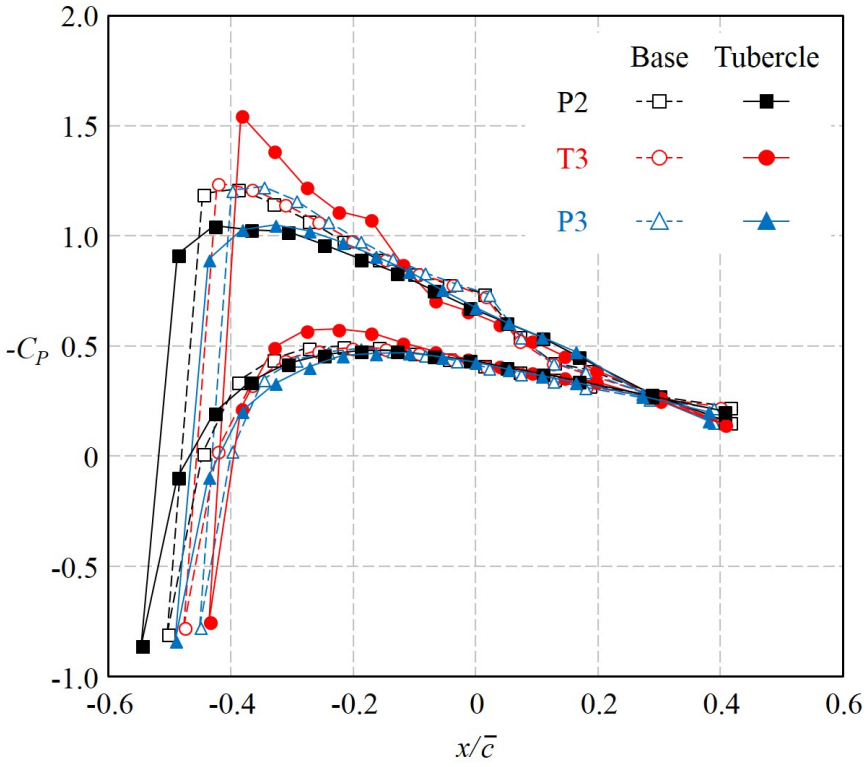

Figure 3.11. Distributions of the surface pressure coefficient at three spanwise locations of P2, T3 and P3 for the base and tubercle models at $\alpha = 4°$.

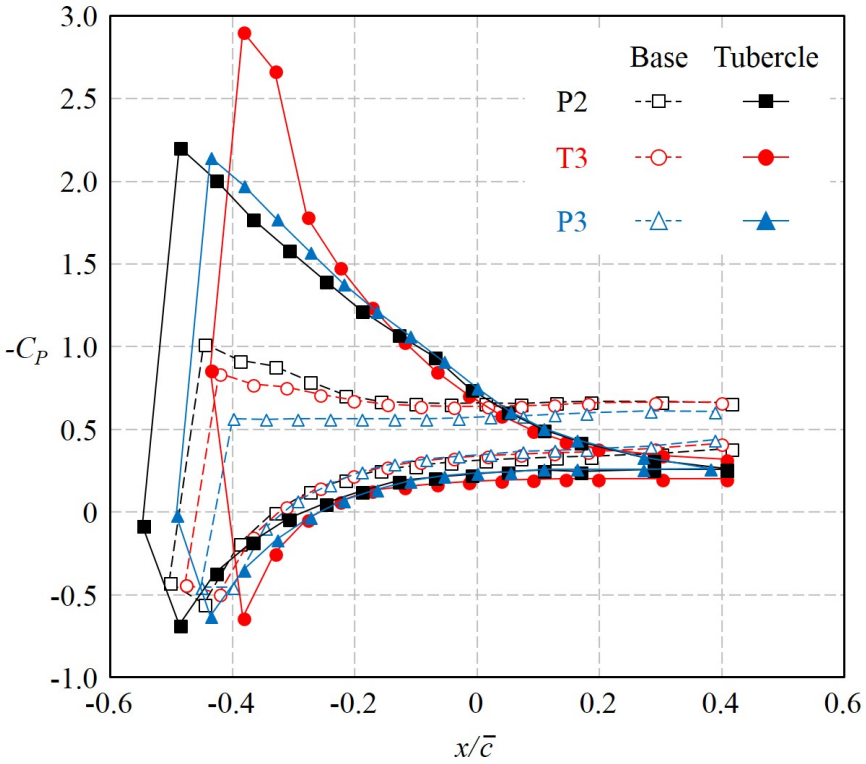

Figure 3.12. Distributions of the surface pressure coefficient at three spanwise locations of P2, T3 and P3 for the base and tubercle models at $\alpha = 13°$.

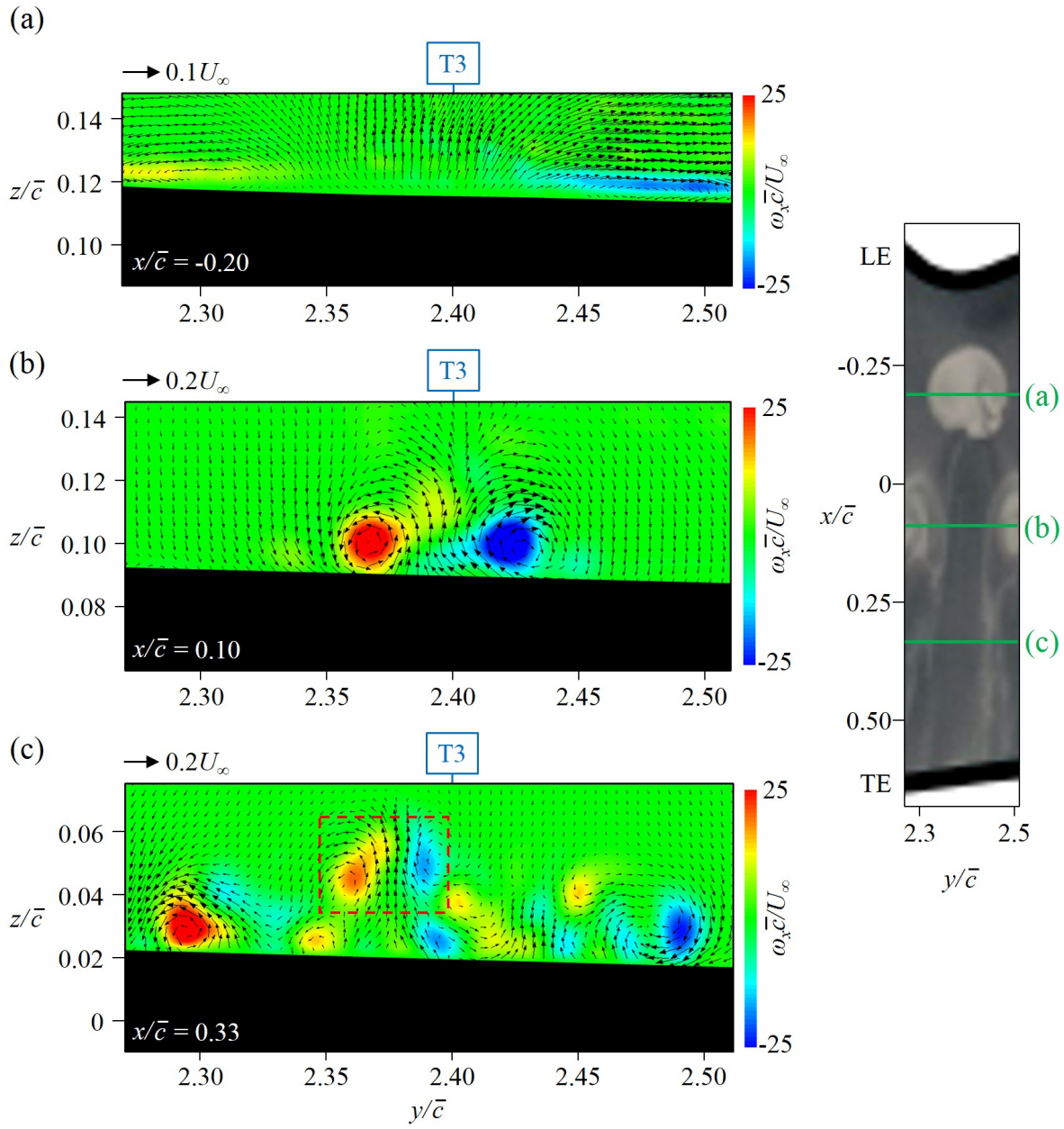

Figure 3.13. Contours of the instantaneous streamwise vorticity and cross-flow velocity vectors for the tubercle model at $\alpha = 4°$: (a) $x/\bar{c} = -0.2$; (b) $x/\bar{c} = 0.1$; (c) $x/\bar{c} = 0.33$. On the right, the PIV measurement locations are indicated by green lines.

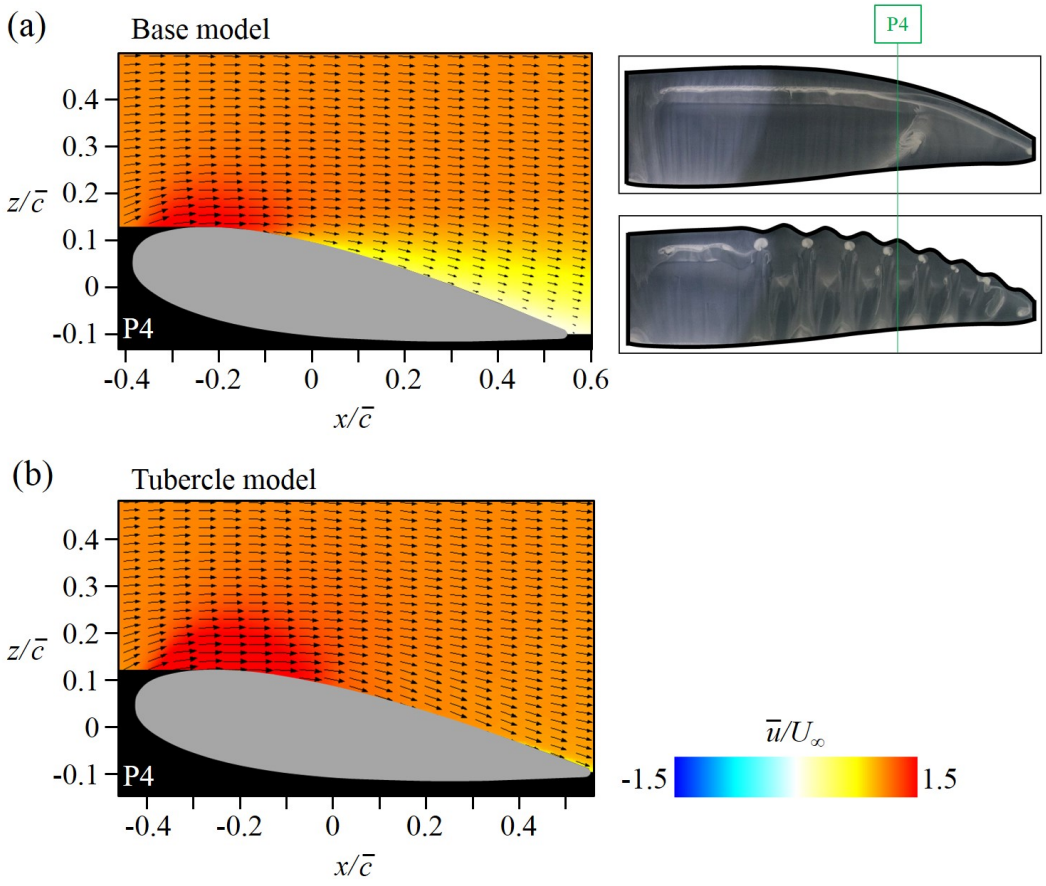

Figure 3.14. Contours of the mean streamwise velocity and velocity vectors at the spanwise location of P4 ($\alpha = 9°$): (a) Base model; (b) Tubercle model. Here, the black thick line denotes $\bar{u} = 0$. The spanwise location corresponding to P4 is indicated by green solid lines in the right figure.

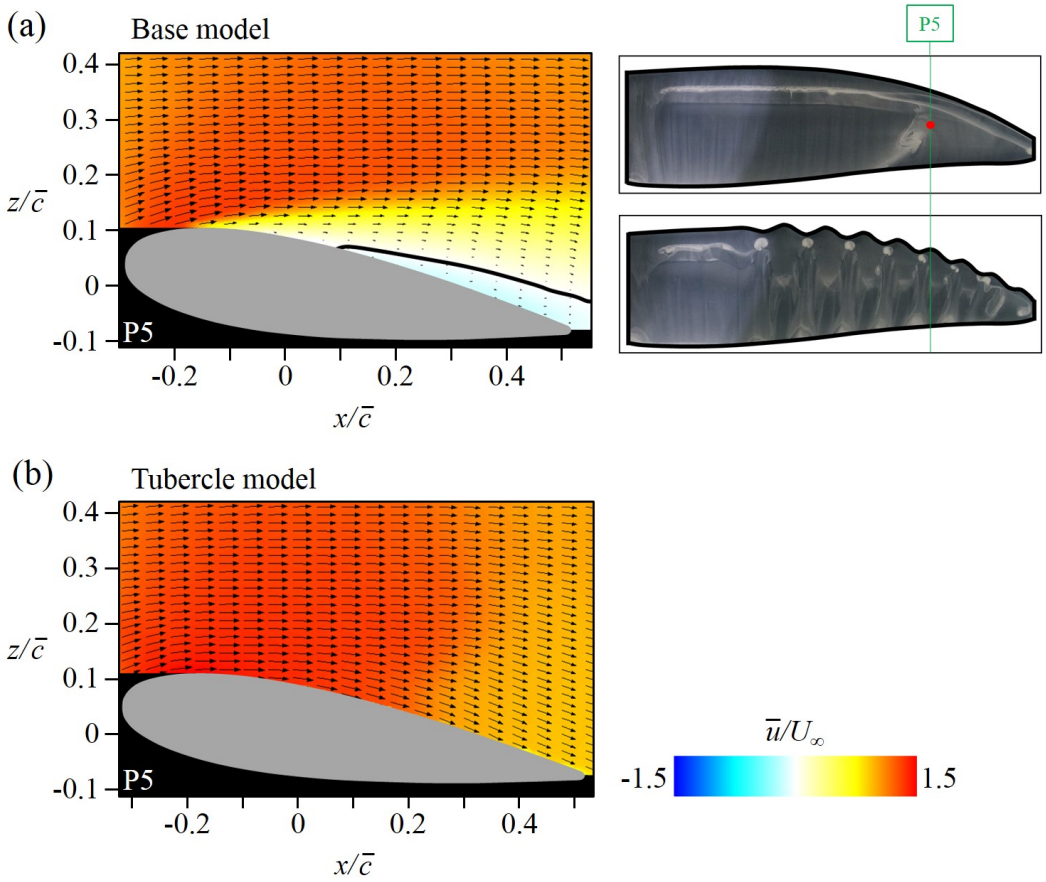

Figure 3.15. Contours of the mean streamwise velocity and velocity vectors at the spanwise location of P5 ($\alpha = 9°$): (a) Base model; (b) Tubercle model. Here, the black thick line denotes $\bar{u} = 0$. The spanwise location corresponding to P4 is indicated by green solid lines in the right figure. Red dot in the right figure denotes separation point measured by PIV.

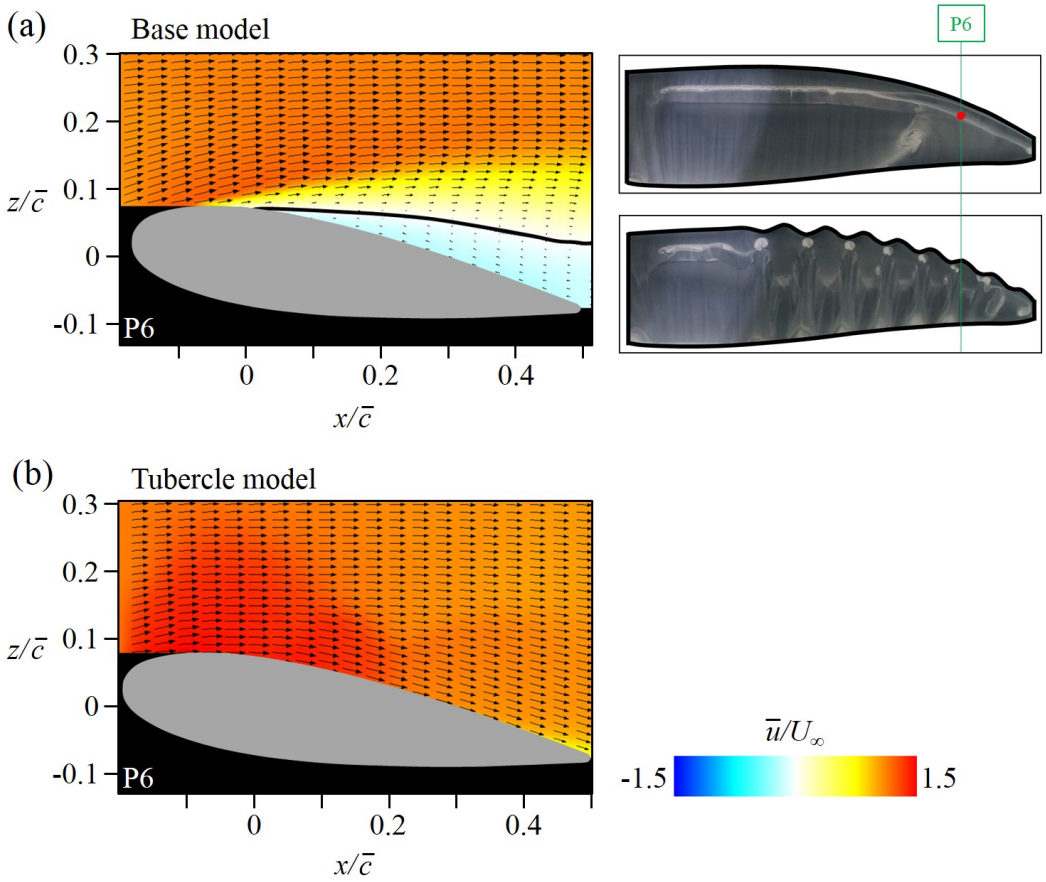

Figure 3.16. Contours of the mean streamwise velocity and velocity vectors at the spanwise location of P6 ($\alpha = 9°$): (a) Base model; (b) Tubercle model. Here, the black thick line denotes $\bar{u} = 0$. The spanwise location corresponding to P4 is indicated by green solid lines in the right figure. Red dot in the right figure denotes separation point measured by PIV.

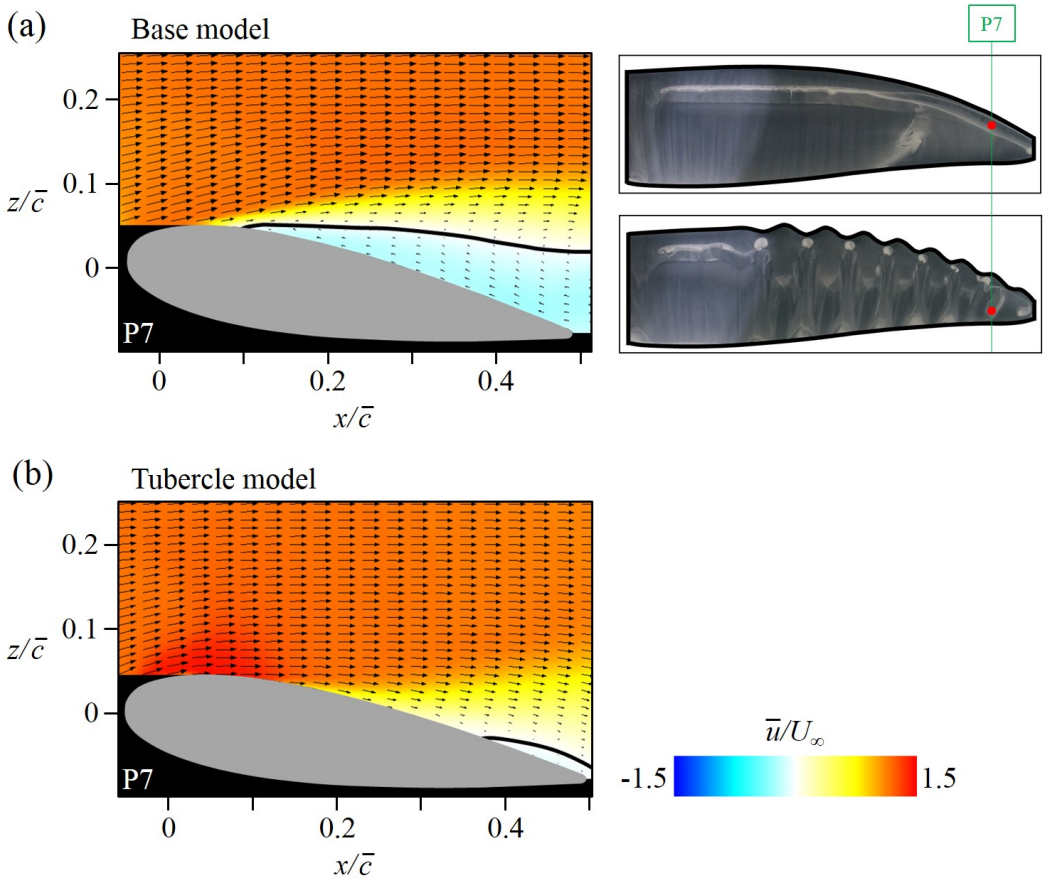

Figure 3.17. Contours of the mean streamwise velocity and velocity vectors at the spanwise location of P7 ($\alpha = 9°$): (a) Base model; (b) Tubercle model. Here, the black thick line denotes $\bar{u} = 0$. The spanwise location corresponding to P4 is indicated by green solid lines in the right figure. Red dots in the right figure denote separation points measured by PIV.

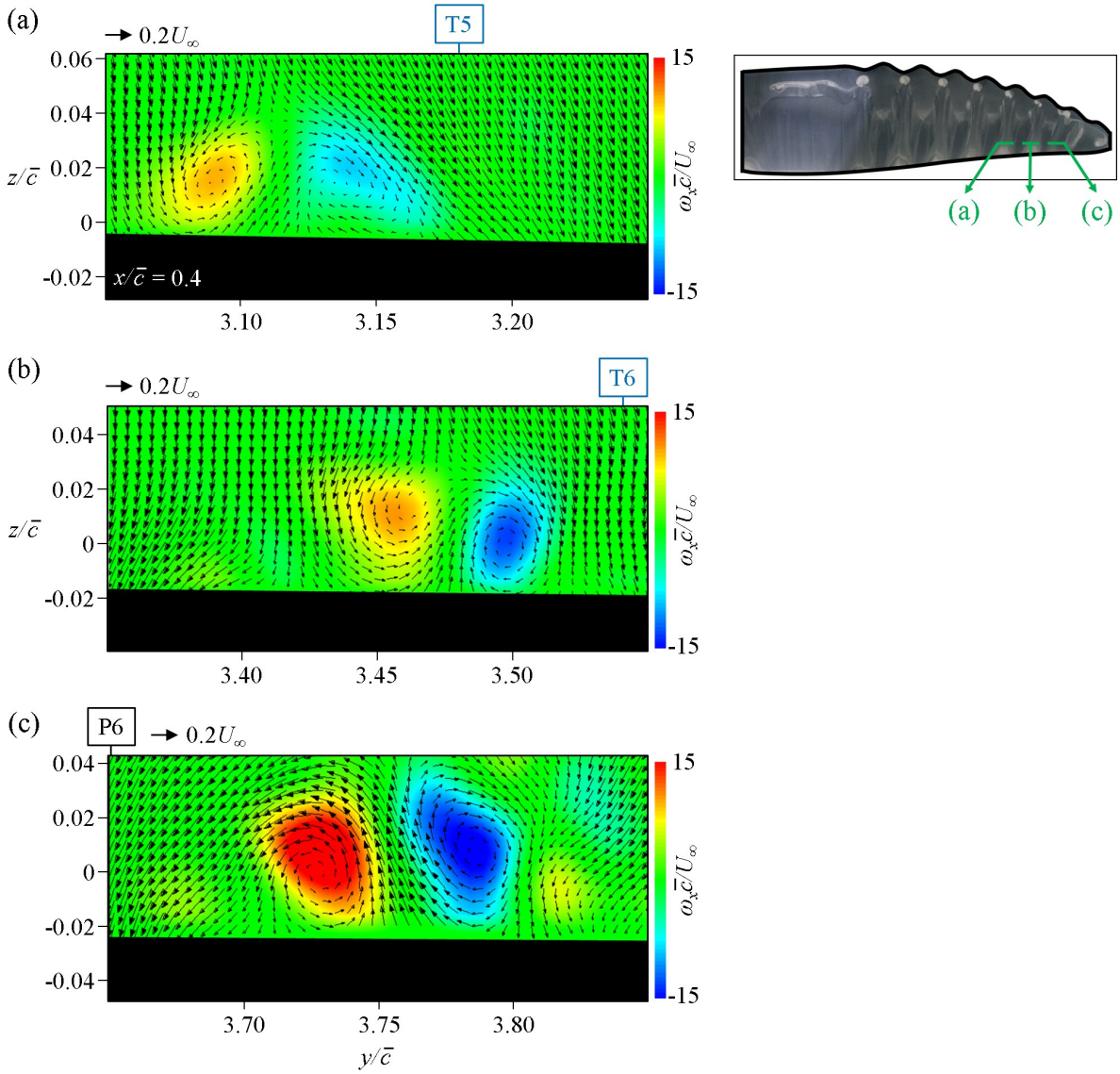

Figure 3.18. Contours of the instantaneous streamwise vorticity and cross-flow velocity vectors at $x/\bar{c} = 0.4$ for the tubercle model at $\alpha = 9°$: (a) $3.0 \leq y/\bar{c} \leq 3.3$; (b) $3.3 \leq y/\bar{c} \leq 3.6$; (c) $3.6 \leq y/\bar{c} \leq 3.9$. On the right, the PIV measurement locations are indicated by green lines.

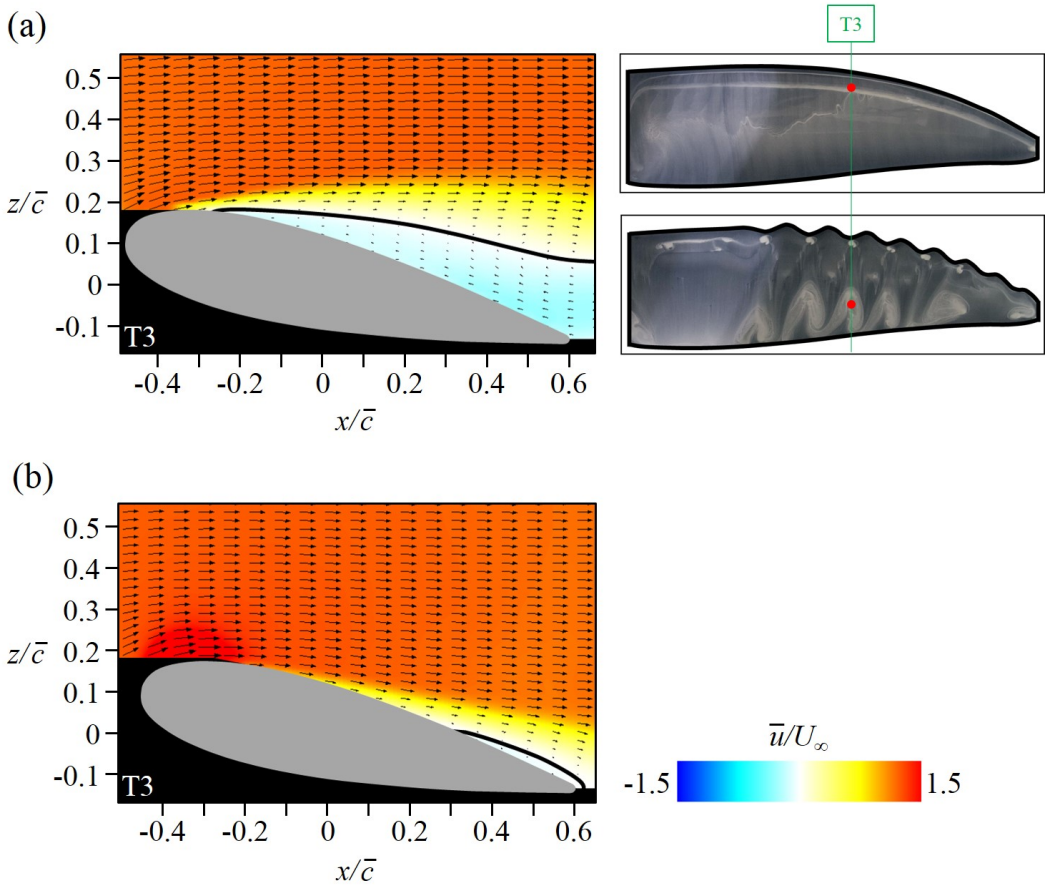

Figure 3.19. Contours of the mean streamwise velocity and velocity vectors at the spanwise location of T3 ($\alpha = 13°$): (a) Base model; (b) Tubercle model. Here, the black thick line denotes $\bar{u} = 0$. The spanwise location corresponding to T3 is indicated by green solid lines in the right figure. Red dots in the right figure denote separation points measured by PIV.

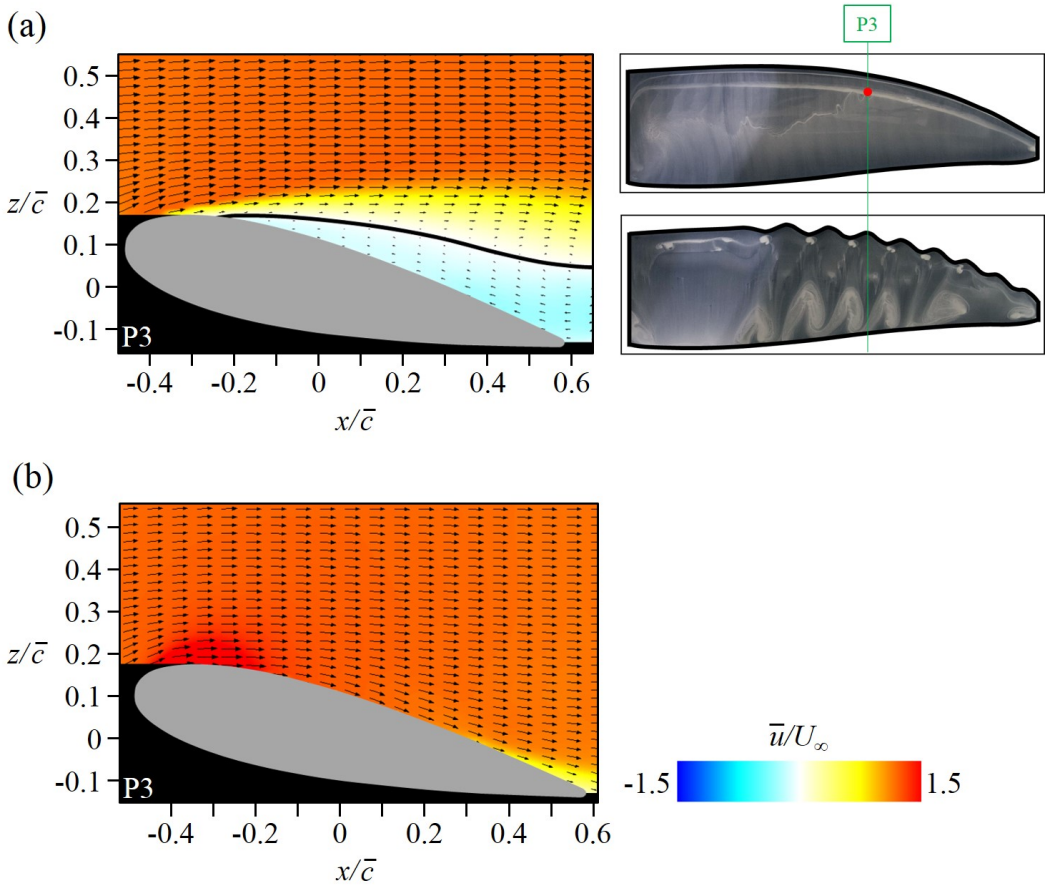

Figure 3.20. Contours of the mean streamwise velocity and velocity vectors at the spanwise location of P3 ($\alpha = 13°$): (a) Base model; (b) Tubercle model. Here, the black thick line denotes $\bar{u} = 0$. The spanwise location corresponding to P3 is indicated by green solid lines in the right figure. Red dot in the right figure denotes separation point measured by PIV.

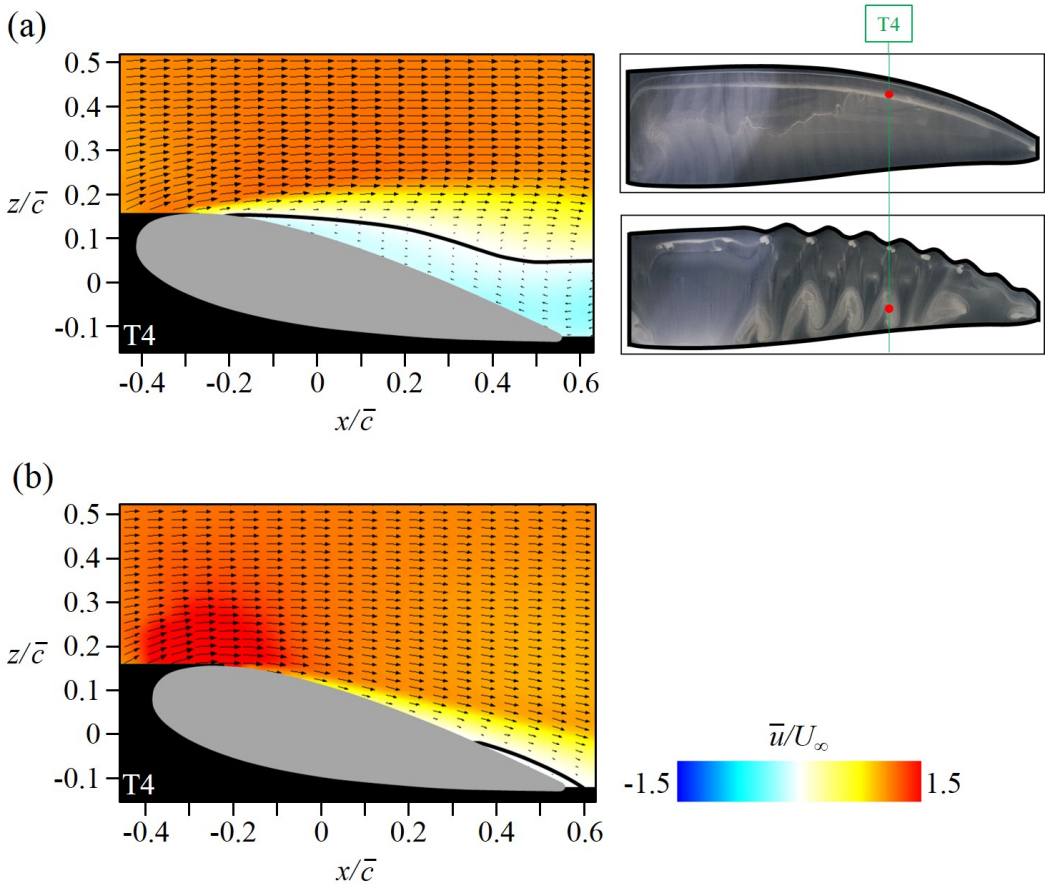

Figure 3.21. Contours of the mean streamwise velocity and velocity vectors at the spanwise location of T4 ($\alpha = 13°$): (a) Base model; (b) Tubercle model. Here, the black thick line denotes $\bar{u} = 0$. The spanwise location corresponding to T4 is indicated by green solid lines in the right figure. Red dots in the right figure denote separation points measured by PIV.

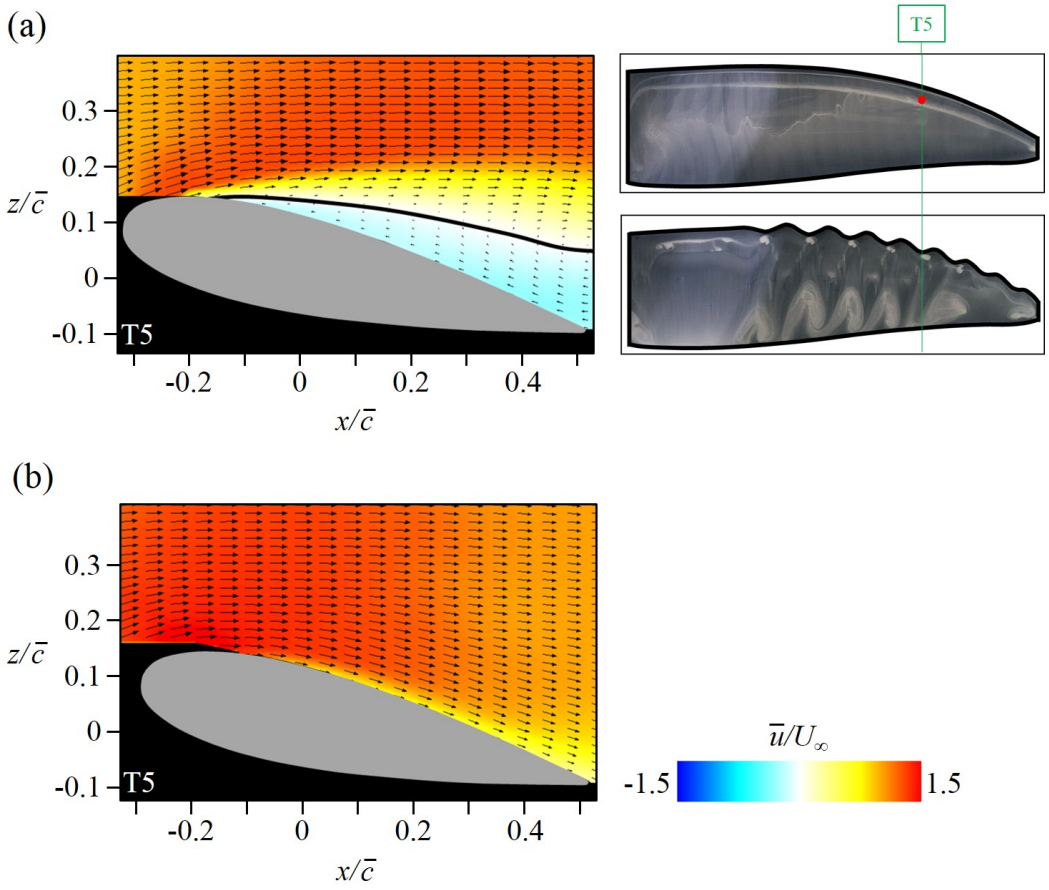

Figure 3.22. Contours of the mean streamwise velocity and velocity vectors at the spanwise location of T5 ($\alpha = 13°$): (a) Base model; (b) Tubercle model. Here, the black thick line denotes $\bar{u} = 0$. The spanwise location corresponding to T5 is indicated by green solid lines in the right figure. Red dot in the right figure denotes separation point measured by PIV.

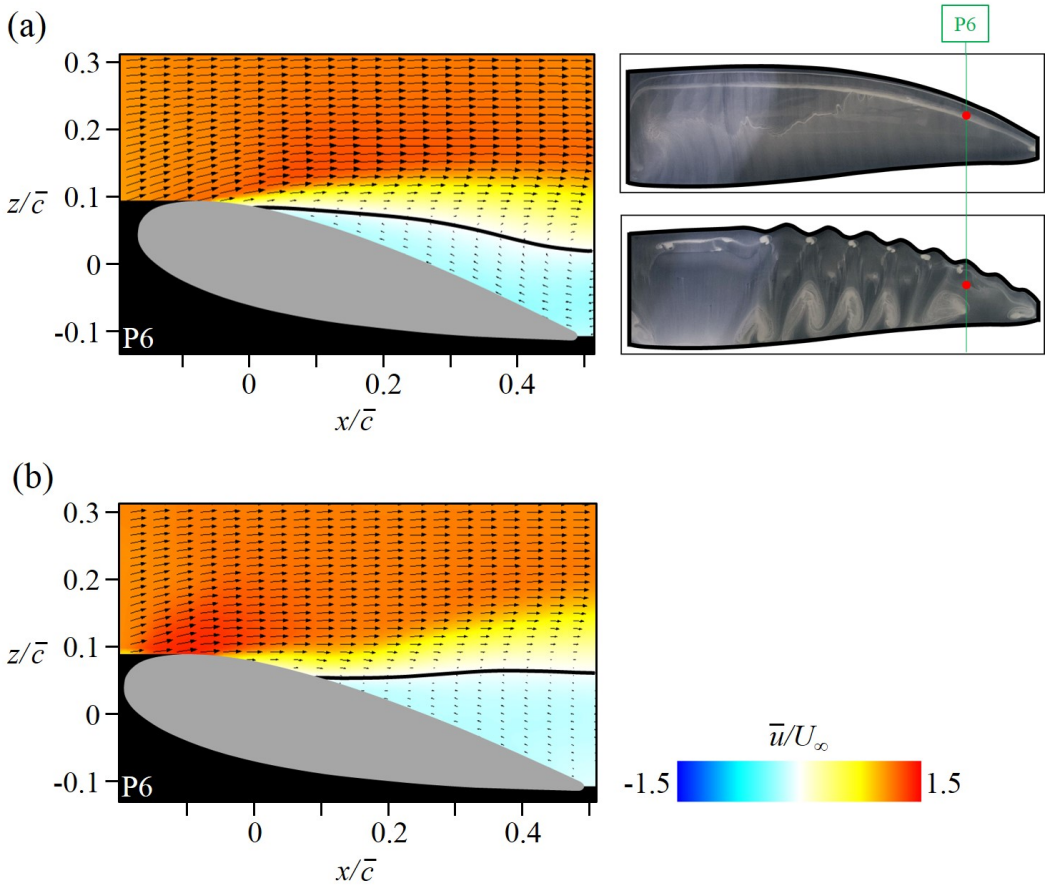

Figure 3.23. Contours of the mean streamwise velocity and velocity vectors at the spanwise location of P6 ($\alpha = 13°$): (a) Base model; (b) Tubercle model. Here, the black thick line denotes $\bar{u} = 0$. The spanwise location corresponding to P6 is indicated by green solid lines in the right figure. Red dots in the right figure denote separation points measured by PIV.

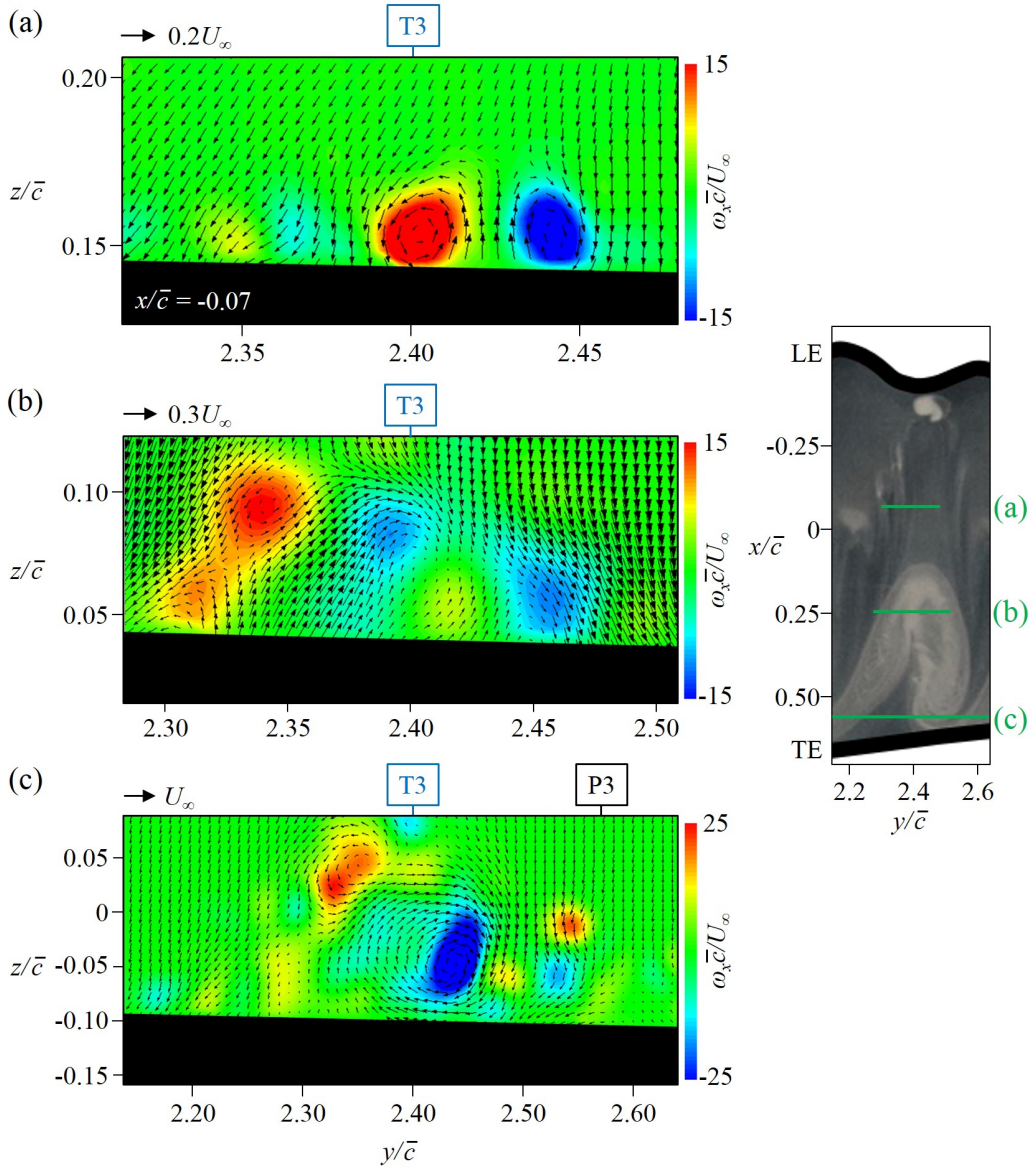

Figure 3.24. Contours of the instantaneous streamwise vorticity and cross-flow velocity vectors for the tubercle model at $\alpha = 13°$: (a) $x/\bar{c} = -0.07$; (b) $x/\bar{c} = 0.25$; (c) $x/\bar{c} = 0.56$. On the right, the PIV measurement locations are indicated by green lines. Note that the scales of the horizontal and vertical axes in (a) and (b) are different from that in (c).

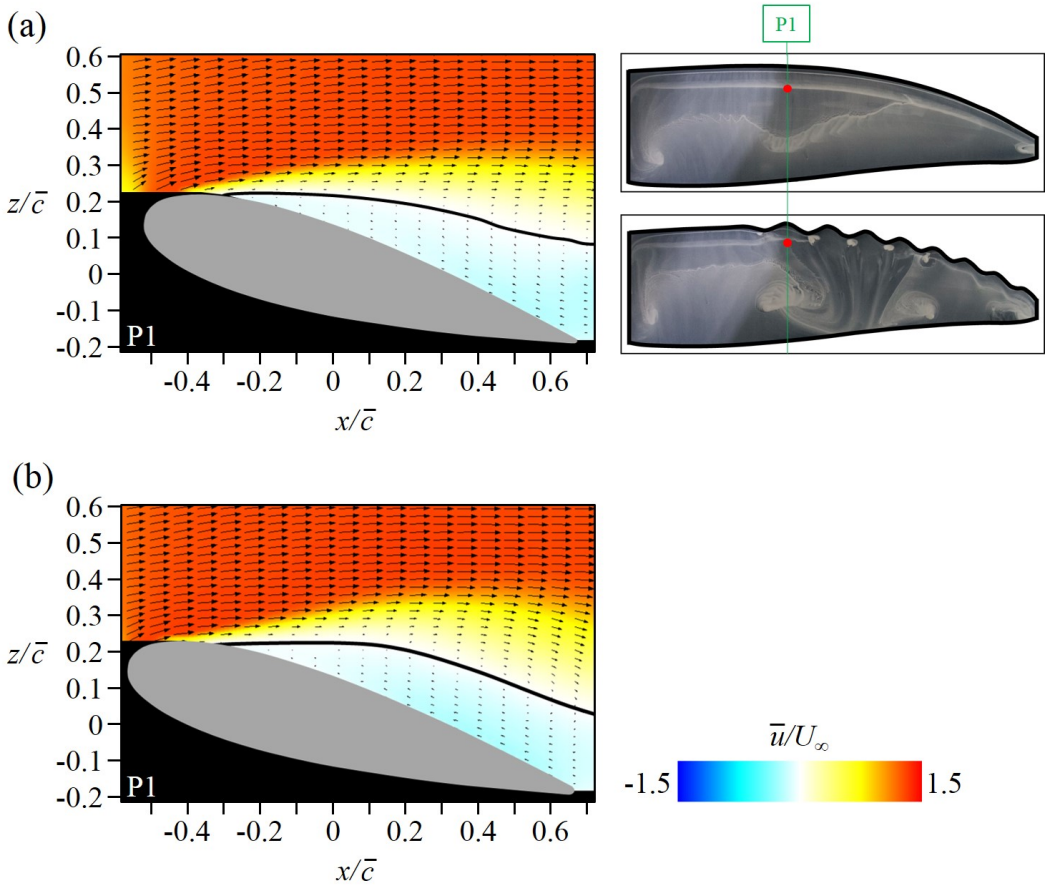

Figure 3.25. Contours of the mean streamwise velocity and velocity vectors at the spanwise location of P1 ($\alpha = 16°$): (a) Base model; (b) Tubercle model. Here, the black thick line denotes $\bar{u} = 0$. The spanwise location corresponding to P1 is indicated by green solid lines in the right figure. Red dots in the right figure denote separation points measured by PIV.

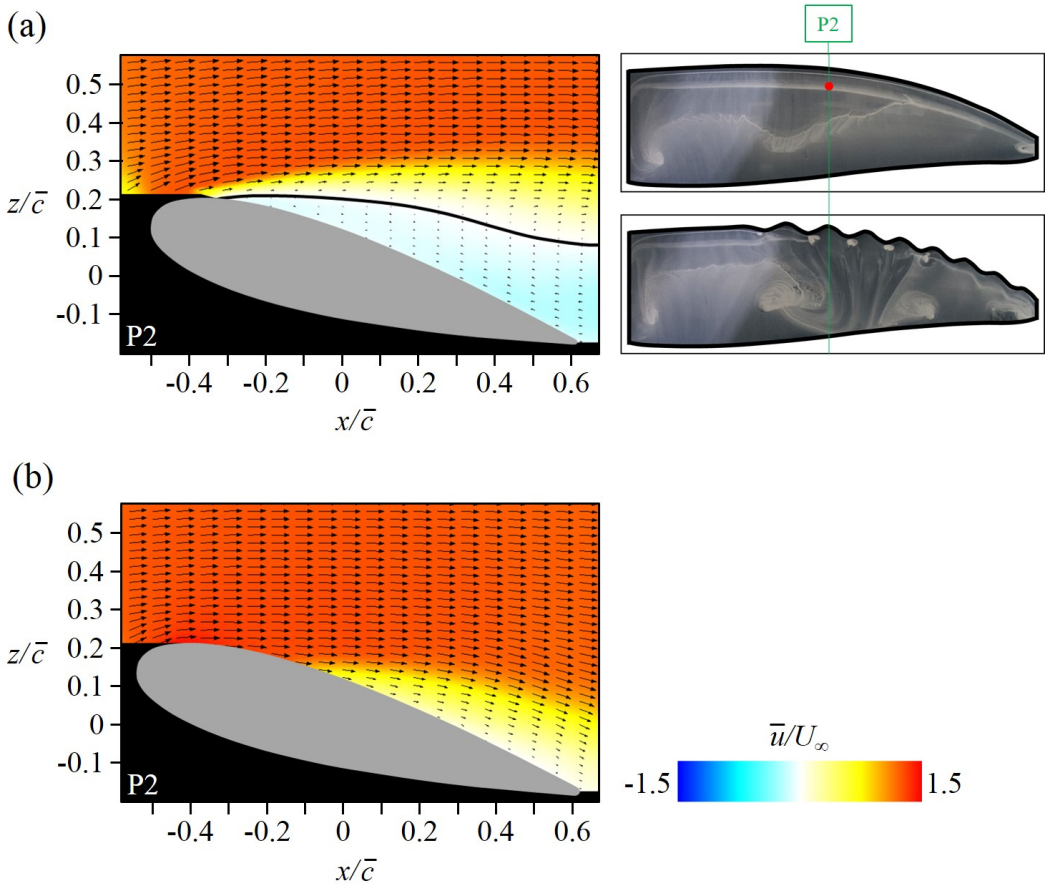

Figure 3.26. Contours of the mean streamwise velocity and velocity vectors at the spanwise location of P2 ($\alpha = 16°$): (a) Base model; (b) Tubercle model. Here, the black thick line denotes $\bar{u} = 0$. The spanwise location corresponding to P2 is indicated by green solid lines in the right figure. Red dot in the right figure denotes separation point measured by PIV.

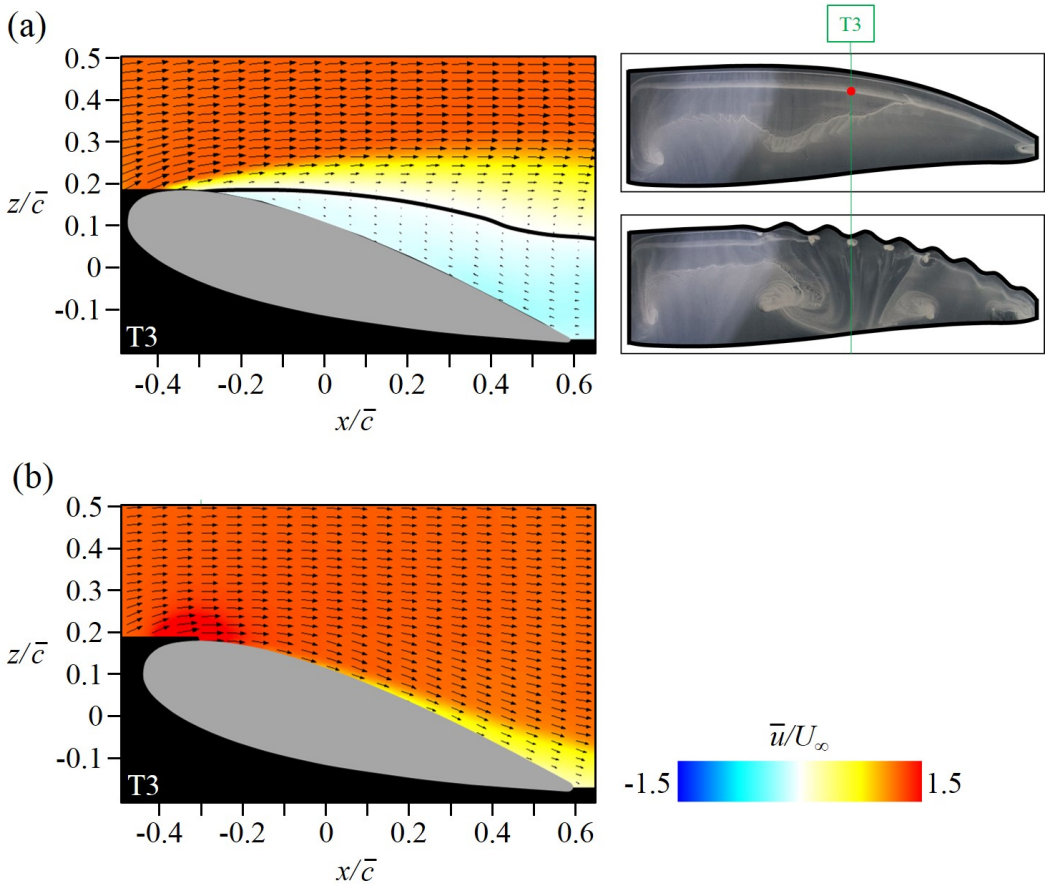

Figure 3.27. Contours of the mean streamwise velocity and velocity vectors at the spanwise location of T3 ($\alpha = 16°$): (a) Base model; (b) Tubercle model. Here, the black thick line denotes $\bar{u} = 0$. The spanwise location corresponding to T3 is indicated by green solid lines in the right figure. Red dot in the right figure denotes separation point measured by PIV.

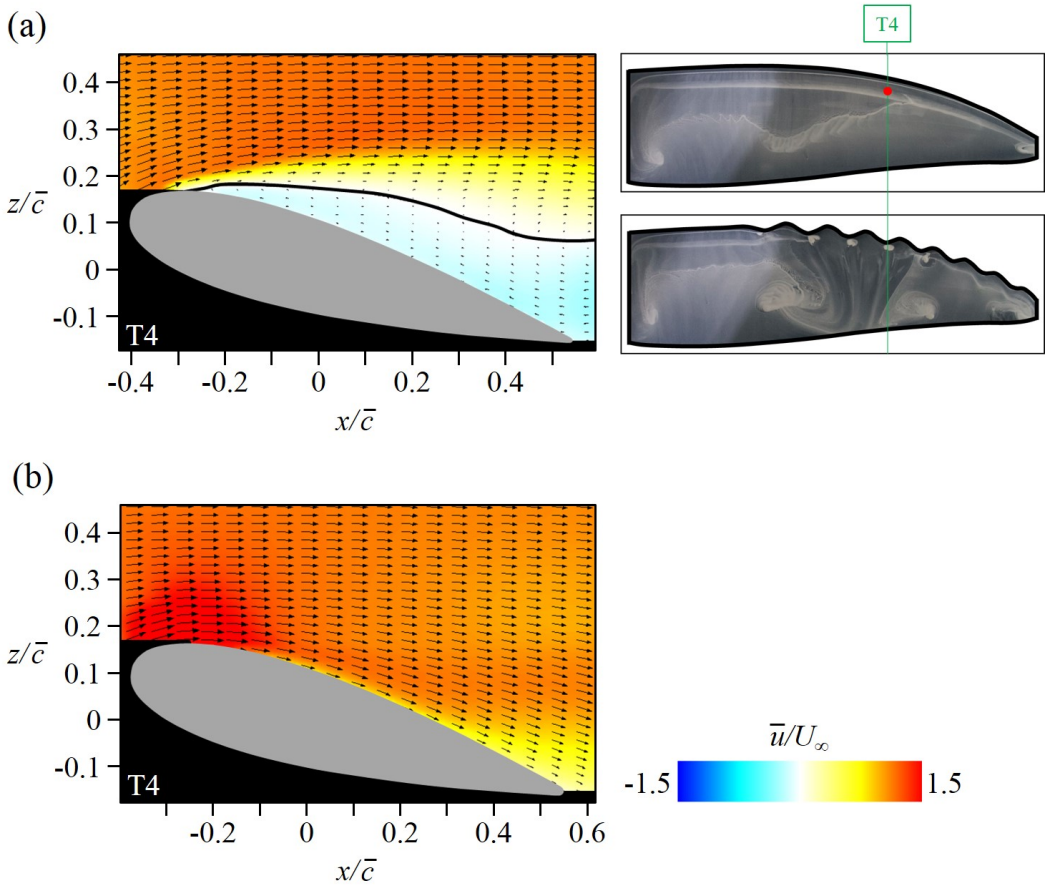

Figure 3.28. Contours of the mean streamwise velocity and velocity vectors at the spanwise location of T4 ($\alpha = 16°$): (a) Base model; (b) Tubercle model. Here, the black thick line denotes $\bar{u} = 0$. The spanwise location corresponding to T4 is indicated by green solid lines in the right figure. Red dot in the right figure denotes separation point measured by PIV.

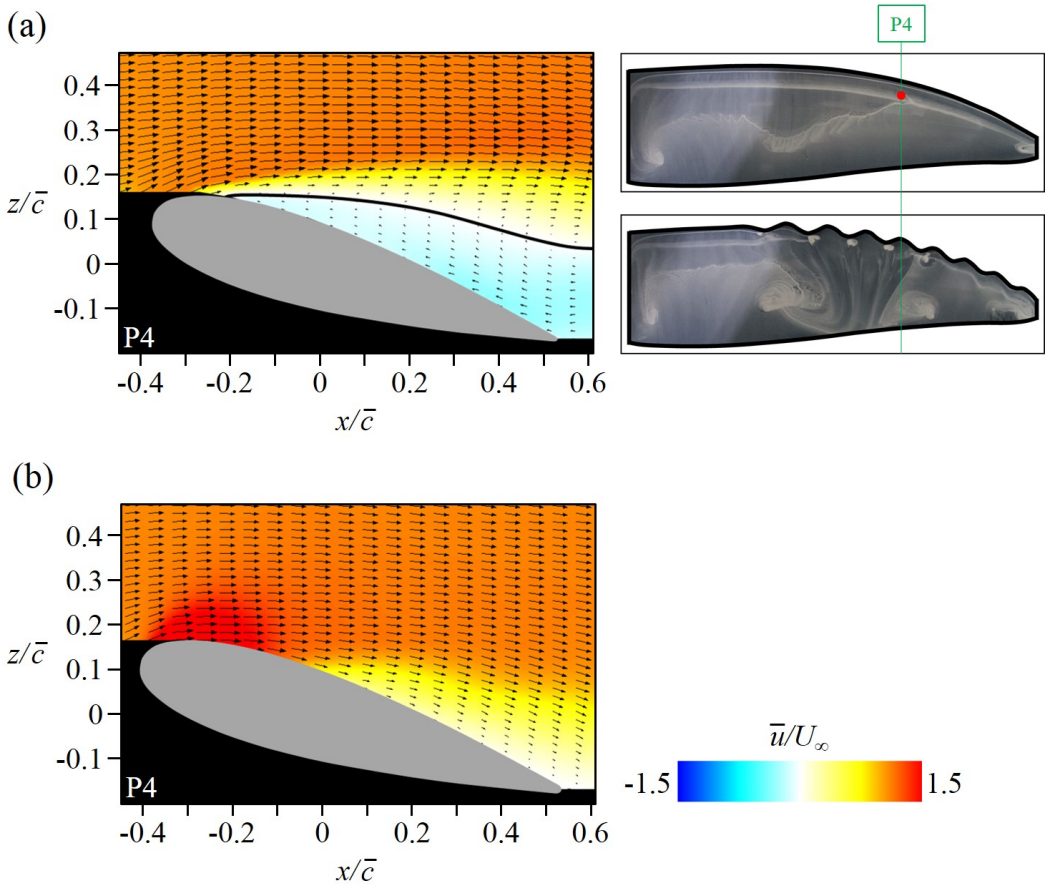

Figure 3.29. Contours of the mean streamwise velocity and velocity vectors at the spanwise location of P4 ($\alpha = 16°$): (a) Base model; (b) Tubercle model. Here, the black thick line denotes $\bar{u} = 0$. The spanwise location corresponding to P4 is indicated by green solid lines in the right figure. Red dot in the right figure denotes separation point measured by PIV.

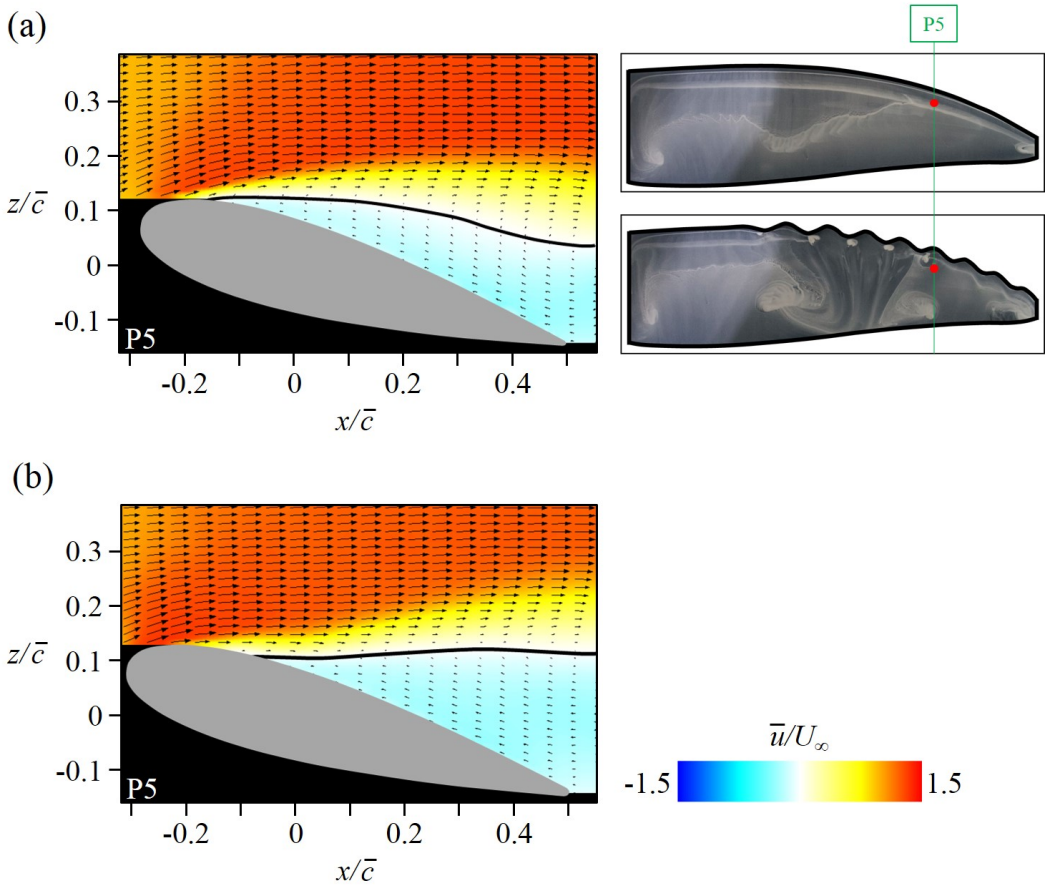

Figure 3.30. Contours of the mean streamwise velocity and velocity vectors at the spanwise location of P5 ($\alpha = 16°$): (a) Base model; (b) Tubercle model. Here, the black thick line denotes $\bar{u} = 0$. The spanwise location corresponding to P5 is indicated by green solid lines in the right figure. Red dots in the right figure denote separation points measured by PIV.

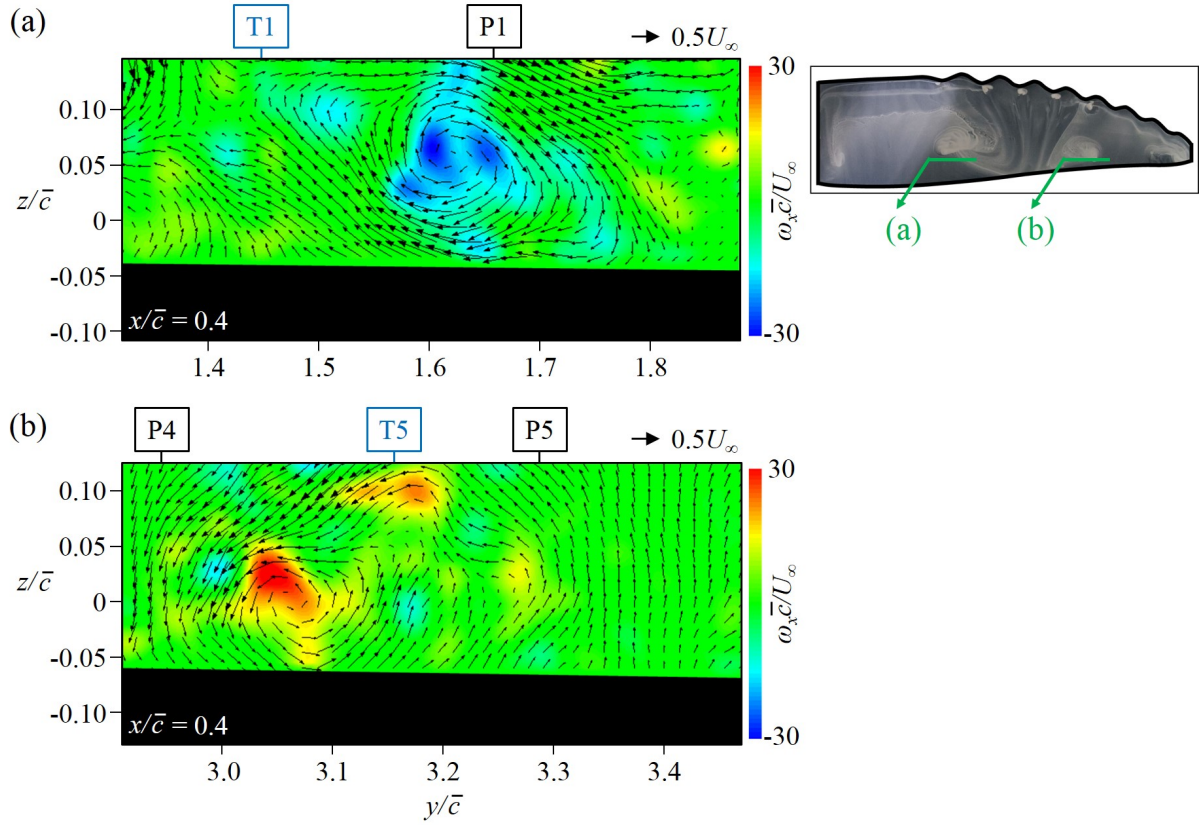

Figure 3.31. Contours of the instantaneous streamwise vorticity and cross-flow velocity vectors for the tubercle model ($\alpha = 16°$): (a) $1.32 \leq y/\bar{c} \leq 1.88$; (b) $2.91 \leq y/\bar{c} \leq 3.47$. On the right, the PIV measurement locations are indicated by green lines.

Chapter 4

Further Discussion

4.1 Comparison with 2D airfoil models

In this section, we compare the role of tubercles on the present 3D wing model with that on 2D airfoil models, and also discuss the effect of tubercles located on the wing root region. In the case of 2D airfoil models without tubercles, main flow separation first occurs near the trailing edge, and moves upstream as the angle of attack increases (Johari *et al.*, 2007; Rostamzadeh *et al.*, 2014). For the present 3D tapered wing model without tubercles, however, main flow separation first occurs near the tip, and progresses inboard with increasing angle of attack as shown in figures 3.4 - 3.7, which is consistent with the numerical simulation by Pedro & Kobayashi (2008). The present vortical structures look similar to those of 2D airfoil models with tubercles, but their effects are quite different. In case of 2D airfoil models with tubercles, counter-rotating streamwise vortices evolving from hemi-spherical separation bubbles lead to flow separation near the trailing edge at the spanwise locations of troughs, resulting in degraded performance in the pre-stall region (Rostamzadeh *et al.*, 2014). However, in the post-stall region, they induce high momentum near the surface and result in the attached and separated flows behind peaks and troughs, respectively, while the flow fully separates over the base 2D airfoil (Johari *et al.*, 2007; Favier *et al.*, 2012; Zhang *et al.*, 2014). In the case of 3D

tapered wing model, in the pre-stall region, streamwise vortices also evolve from hemi-spherical separation bubbles and produce flow separation near the trailing edge due to their induced upward motion behind the trough, which decreases the lift. However, these streamwise vortices prevent the inboard progression of flow separation near the tip region, which compensates the lift loss caused by flow separation near the trailing edge. Previous studies on 3D wing models with a rectangular planform geometry showed that the lift is indeed decreased by tubercles in the pre-stall region (Hansen *et al.*, 2010; Yoon *et al.*, 2011).

4.2 Effect of smooth leading edge in the root region

To investigate the effects of smooth leading edge in the root region for the present tubercle model, another tubercle model (named tubercle model II) is constructed: from root to P1 ($0 \leq y/\bar{c} \leq 1.71$), we add new tubercles which have the amplitude of $0.036c_l$ (nearly the same as the amplitude of P1) and the wavelength of 0.4 (similar to the wavelength of first tubercle) (figure 4.1). Figures 4.2 - 4.4 show the results from force measurements. The lift coefficient of tubercle model II is similar to that of the original tubercle model up to $\alpha = 10°$. At $11° \leq \alpha \leq 15°$, the lift coefficient of tubercle model II is slightly lower than that of the tubercle model. In the post-stall region ($\alpha \geq 16°$), however, the tubercle model II has a higher lift coefficient than the original tubercle model because of wider attached region near the root (see figure 4.5(b)). The tubercle model II has higher drag and lower L/D in the pre-stall region but has better performances in the post-stall region than the original tubercle model does. Figure 4.5 shows the surface-oil-flow visualizations for the tubercle model II at $\alpha = 13°$ (near-stall region) and 16° (post-stall region). Surface-oil-flow visualization in the near-stall region ($\alpha = 13°$; figure 4.5(a)) indicates that

trailing edge separation occurs even in the root region ($0 \leq y/\bar{c} \leq 1.71$) because of the leading-edge tubercles near the root, which is very different from the results of the original tubercle model (figure 3.6(b)). At $\alpha = 16°$, attached flow region on the tubercle model II becomes wider in the root region than the original tubercle model (figure 3.7(b)), resulting in higher lift coefficient at the post-stall region.

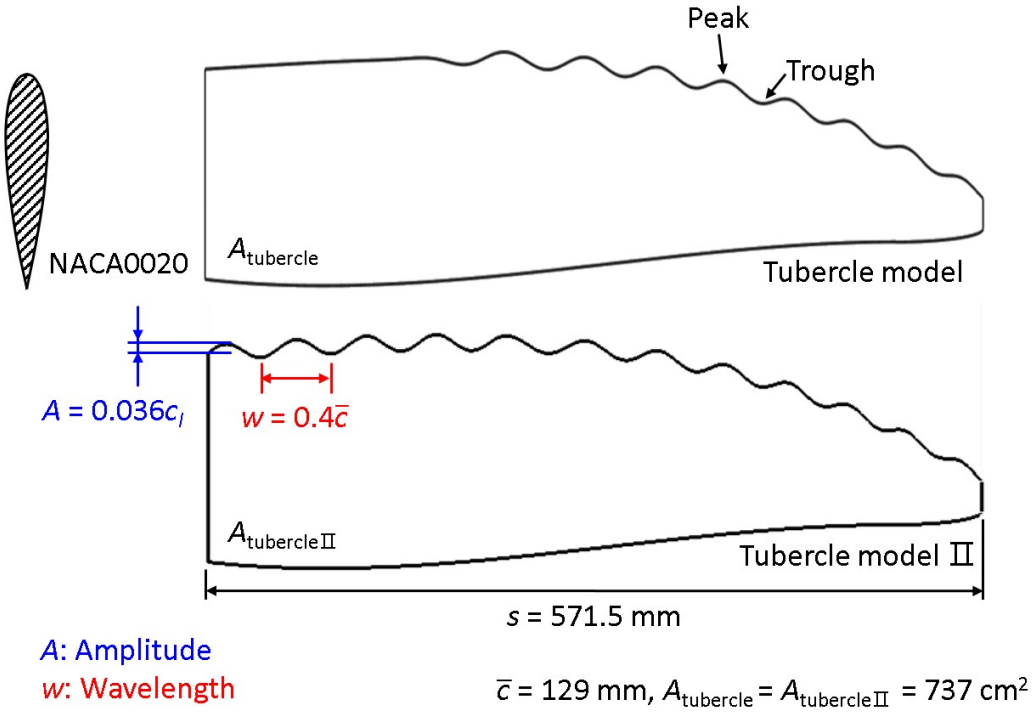

Figure 4.1. Planform views of the tubercle model and another tubercle model.

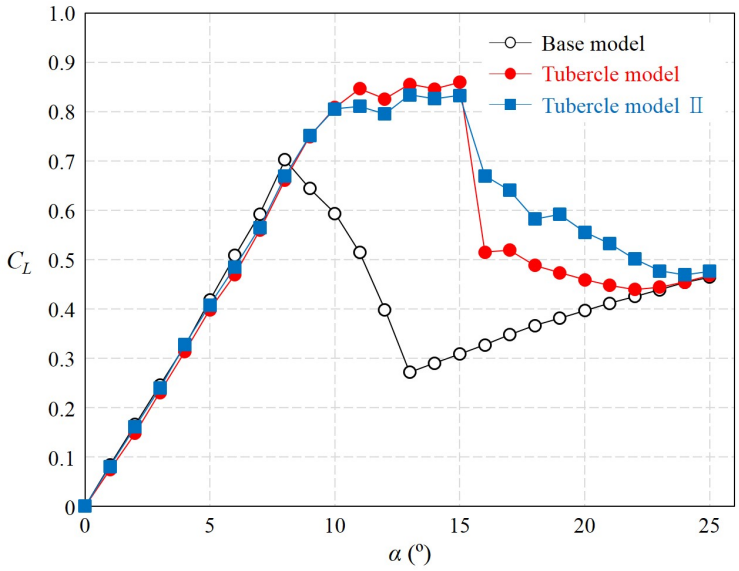

Figure 4.2. Variations of the lift forces with the angle of attack for the base, tubercle and anohter tubercle models.

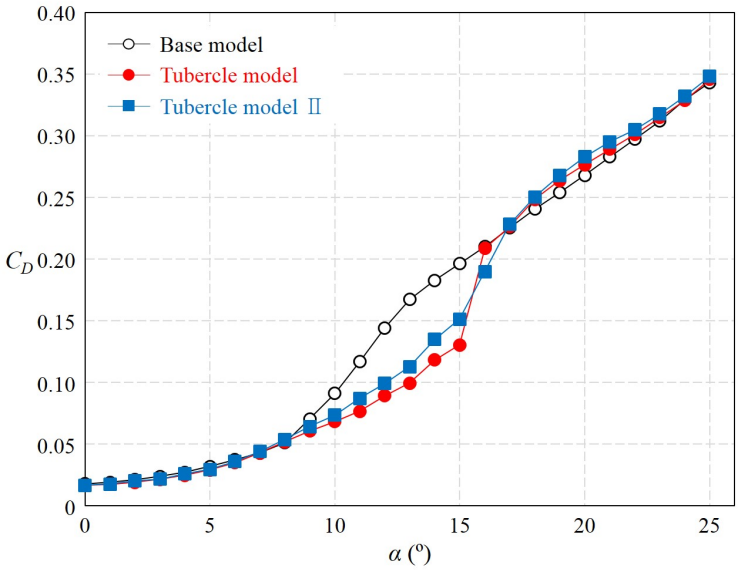

Figure 4.3. Variations of the drag forces with the angle of attack for the base, tubercle and anohter tubercle models.

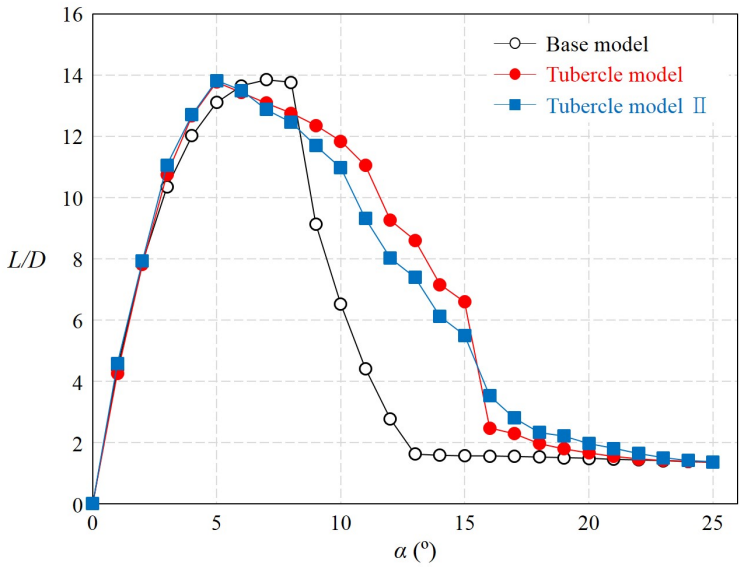

Figure 4.4. Variations of the lift-to-drag ratio with the angle of attack for the base, tubercle and anohter tubercle models.

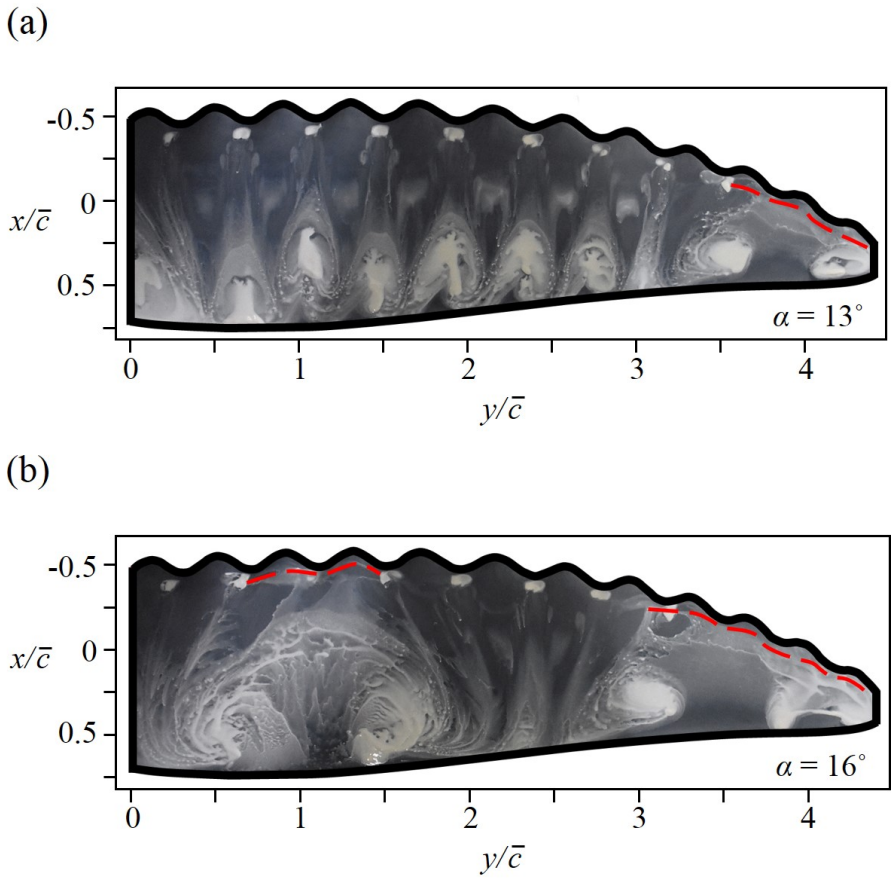

Figure 4.5. Surface-oil-flow visualizations for the tubercle model II: (a) $\alpha = 13°$; (b) $\alpha = 16°$. Here, red dashed line denotes flow separation.

Chapter 5

Application to a Quadrotor Blade

5.1 Introduction

As electronic equipment has been miniaturized recently, small-size unmanned aerial vehicle (UAV) has developed and widely used for various fields such as monitoring, exploration and entertaninment (Theys *et al.*, 2014, 2017). In particular, the multi-rotor UAV has many advantages becuase it can be VTOL (vertical take-off and landing) and their blades are easy to maintain and repair. So far, many previous studies on rotor blades have benn performed under hovering conditions (Benedict *et al.*, 2015; Brandt & Selig, 2011; Deters *et al.*, 2014). It is considered to be sufficient becuase the angle of attack for forward flight is small. However, the need for research on forwared fligth condition has arisen due to high speed of forward flight such as delivery (Hoffmann *et al.*, 2007).

Several previous studies have attempted to improve the performance of the blade by applying leading-edge tubercles, but these are limited to axial flow conditions or 0° of angle of attack (Asghar *et al.*, 2018; Cully, 2017; Moore & Ning, 2016). Therefore, in this study, a new blade model is designed by adding leading-edge tubercles. We measure performance of the blade at various rotating speeds and advance ratios. To investigate the flow characteristics, we conduct PIV measurement for suction surface and wake of the blade model.

5.2 Experimental set-up

To investigate the effect of the leading edge tubercles on the quadrotor blade performance in forward flight, two blade models with and without tubercles are considered. The thrust and torque on both models are measured using 6-axis force sensor. The flow fields around both models are obtained using a two-dimensional particle image velocimetry (2D-PIV).

Figure 5.1 shows planform views of the present blade models. They are designed based on the blade used in Phantom4 quadrotor model (DJI) and made of acrylonitrile butadiene styrene (ABS) resin. They have a mean chord length of $\bar{c} = 21.03$ mm, a radius of $s = 120$ mm, and solidity of $\sigma = 0.112$. The blade models without and with leading-edge tubercles are named as base and tubercle models, respectively. For the base model, the chord length and pitch angle variations with spanwise location is shown in figure 5.2. The tubercle model has ten tubercles along the leading edge with amplitude of $0.06\bar{c}$ and wavelength of $0.5\bar{c}$ (figure 5.1). These values are within the range of the tubercle dimensions of the real humpback whale's flipper (Johari *et al.*, 2007). The maixmum blockage ratio is 4.5% which is less than the minimum value (7.5%) recommended to avoid disturbances from the wind-tunnel wall (Barlow *et al.*, 1999). The surfaces of blade models are coated with matt black to reduce laser reflection and sanded with progressively finer sandpaper down to 600 grit to have smooth surfaces. For the tubercle model, all tubercle peaks and troughs are numbered from 1 to 10 (from the tip to the root). Same spanwise locations are also numbered for the base model for comparison.

Figure 5.3 shows the schematic diagram of the force measurement. The thrust and torque on the blade models are measured with 6-axis force sensor (ATI Mini40) which are attached to the motor assembled with the models.

Signals from the force sensor are sampled for 10 s at a rate of 10 kHz to obtain a fully converged mean force. The thrust (C_T) and power (C_{Po}) coefficients are defined as $C_T = T/(\rho U_{tip}^2 A)$ and $C_{Po} = T\Omega/(\rho U_{tip}^3 A)$, respectively, where T is the thrust, Ω is the angular velocity of the blade, ρ is the air density and U_{tip} is the tip velocity of the blade. The force measurements are conducted at three different RPMs (3,500, 4,300 and 5,100) and seven different advance ratios (μ). The angle of atack (α) considered in this study is 40°. According to product specificaitons, this value is almost the maximum angle of attack in the forward flight condition. The Reynolds numbers, $\mathrm{Re} = U_{tip}\bar{c}/\nu$ where ν is the kinematic viscosity of air, based on the mean chord length and tip velocity are about 62,000, 76,000 and 90,000. Using the method in Coleman and Steele (2009), uncertainties of the measured thrust and power coefficients are estimated to be less than 2.4% and 2.6%, recpectively. The x, y and z denote the streamwise, spanwise and vertical directions, respectively. The x' lies on the disk plane pointing upward and the y' denotes the direction of counter-clockwise rotation of the blade. The origin is located at the bottom of the hub.

The velocity fields around the blade models are measured using a 2D-PIV system shown in figure 5.4. The 2D-PIV system consists of a fog generator (SAFEX), a double-pulsed Nd:YAG laser (Litron Lasers) operating at 135 mJ, a CCD camera (Vieworks VH-4M) with a 2,048 pixel × 2,048 pixel resolution, and a timing hub (Integrated Design Tools). The fog generator produces liquid droplets having a mean diameter of 1 μm, which are introduced into the wind tunnel. Laser and laser optics make laser sheets having a thickness of 3 mm, which illuminate the planes of interest. The velocity measurements are performed on several $(x' - y')$ on suction surfaces of the blade and $(y - z)$ planes in the wake. To measure phase-locked velocity field, an optical sensor is used. And one image pair is taken per every 15 revolutions. An iterative cross-correlation

analysis is implemented with an initial interrogation window size of 64 pixel × 64 pixel and a final interrogation window size of 32 pixel × 32 pixel. The interrogation window is overlapped by 50%, leading to spatial resolutions of $0.01c_l$ (c_l: local chord length) on the $x' - y'$ plane and $0.02\bar{c}$ on the $y - z$ plane. Five hundred pairs of images are taken to obtain the time-averaged flow field. The uncertainties of velocity and vorticity are estimated to be less than 4.5% and 5.0%, respectively (Willert & Gharib, 1991; Fouras & Soria, 1998; Raffel *et al.*, 2013).

5.3 Results and discussion

Figures 5.5 and 5.6 show the variations of the thrust and power coefficients devided by solidity with the advance ratios for the base and tubercle models at RPM = 3,500, 4,300 and 5,100. The thrust coefficients of both models decrease as the advance ratio increases, which is also observed in previous study in forward flight condition (Theys *et al.*, 2014). At low advance ratios ($\mu \leq 0.1$), the thrust performance is similar within the experimental uncertainty range for models with and without tubercles. As the advance ratio increases, however, the tubercle model shows higher thrust performance than that of the base model. For example, at the highest advance ratio and at the RPM of 5,100, tubercles increase the thrust coefficient by about 18% (figure 5.5). The power coefficients of the both models also decrease as the advance ratio increases. At low advance ratios (less than $\mu \approx 0.12$), the power performance is similar within the experimental uncertainty range for models with and without tubercles. As the advance ratio increases, however, the tubercle model shows lower power performance than that of the base model. For example, at the highest advance ratio and at the RPM of 5,100, tubercles increase the power coefficient by about 9%

(figure 5.6). Considering both parameters (thrust and power coefficients), however, the increase of the thrust coefficient is higher than the power coefficient. Therefore, tubercles improve the blade performance at high advance ratios.

Figures $5.7 - 5.12$ show contours of the mean $x'-$direction velocity and velocity vectors at the spanwise locations of $P1 - P6$ on the advacing side. For the base model, trailing-edge separations are observed at all planes considered in this study. Tubercles, however, reduce back-flow region near the trailing edge behind peaks near the tip- and mid-span (figures 5.7, 5.9 and 5.12). Figures 5.17 and 5.18 show mean streamwise vorticity and velocity vectors in the wake of the base and tubercle models at two different spanwise ranges. For the both models, tip vortex is observed clearly near the tip at $y/\bar{c} \approx 0.5$. The wake of the tubercle model shows discrete vorticity distribution indicating that counter-rotating streamwise vortex pairs are generated (figures 5.17(b) and 5.18(b)).These vortical structures generate downwash motions behind peaks, resulting in reduction of back-flow reigon near the trailing edge. This mechanism is very similar to that of the 3D fixed-wing case. Figures $5.13 - 5.16$ show contours of the mean $x'-$direction velocity and velocity vectors at the spanwise locations of $T1 - P6$ on the retreating side. There is no differences between base and tubercle models.

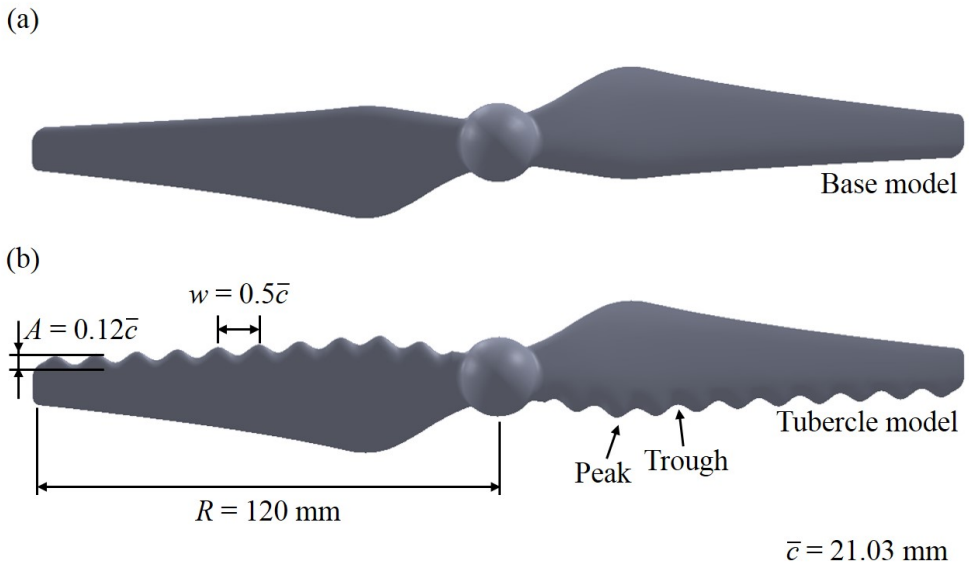

Figure 5.1. Planform viesw of blade models. (a) Base model; (b) Tubercle model.

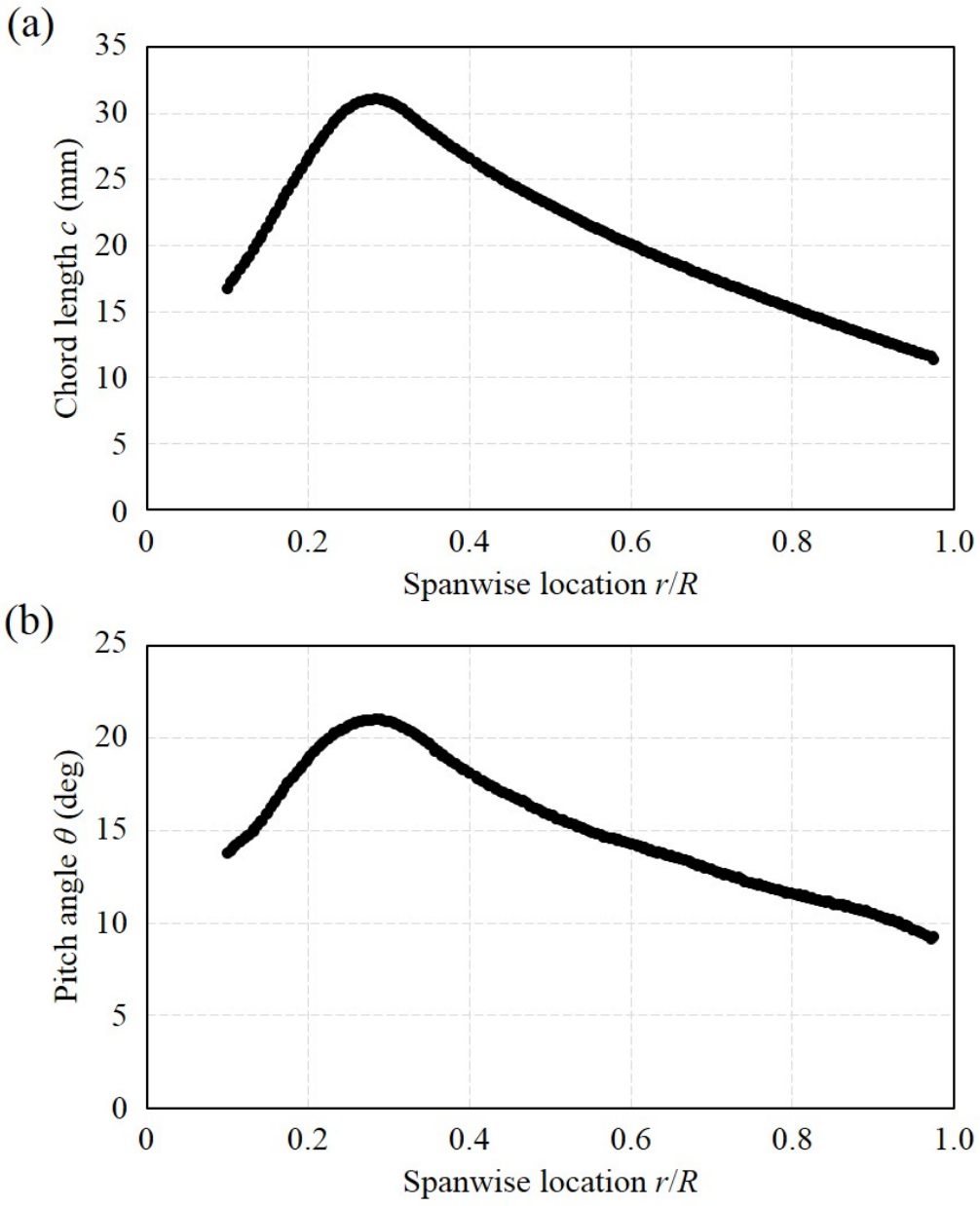

Figure 5.2. Geometry of the base model. (a) Chord length distribution; (b) Pitch angle distribution.

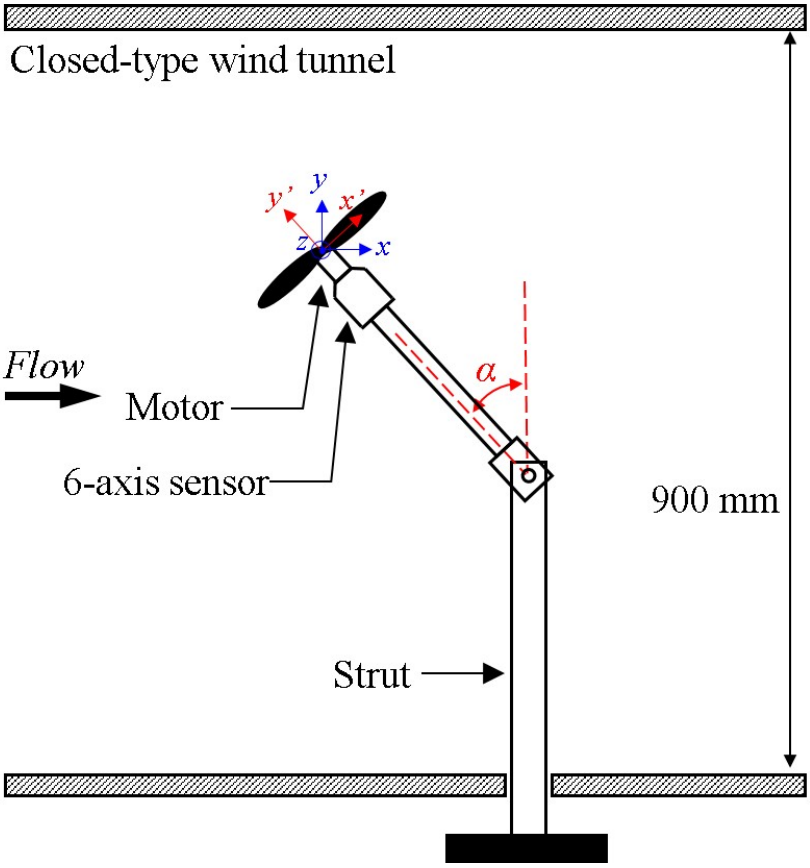

Figure 5.3. Schematic diagram of the experimental set-up for the force measurement.

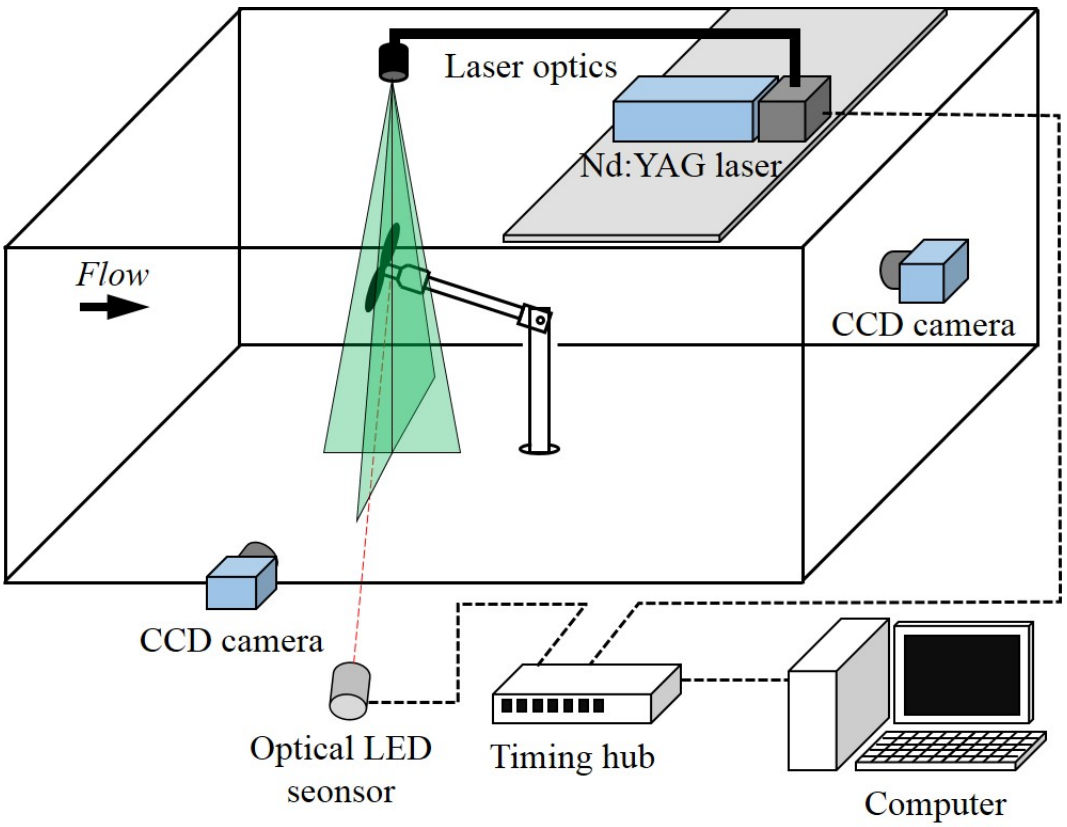

Figure 5.4. Schematic diagram of the experimental set-up for the PIV measurement.

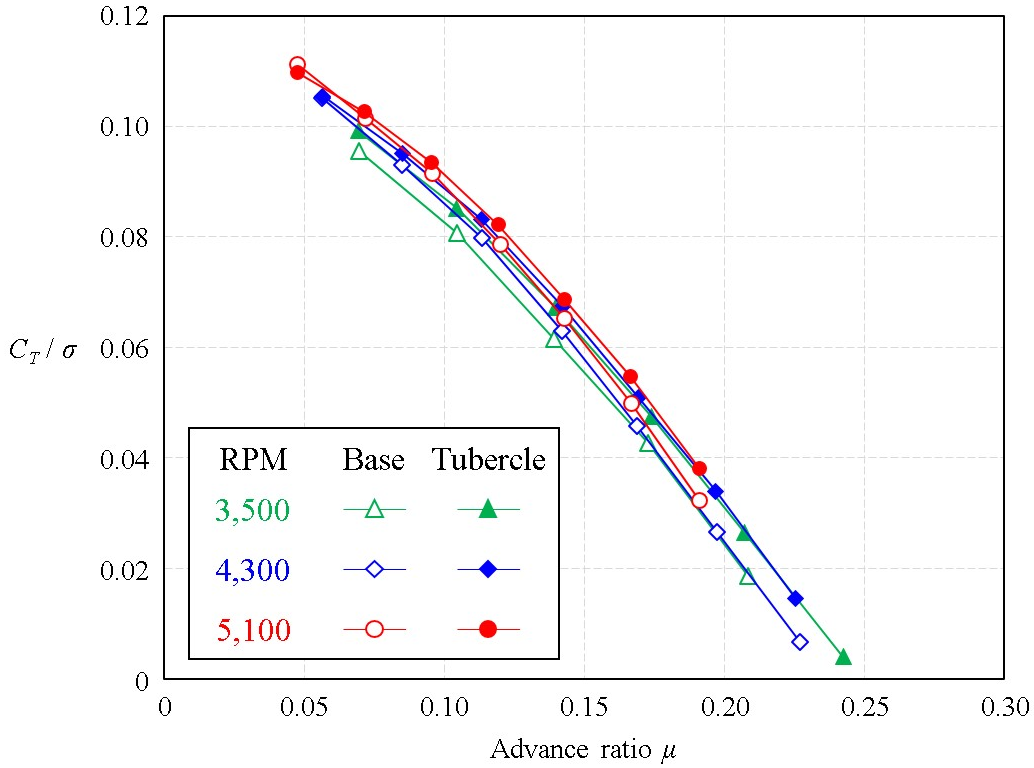

Figure 5.5. Variations of thrust coefficient divided by solidity (C_T/σ) with the advance ratio for the base and tubercle models at $\alpha = 40°$.

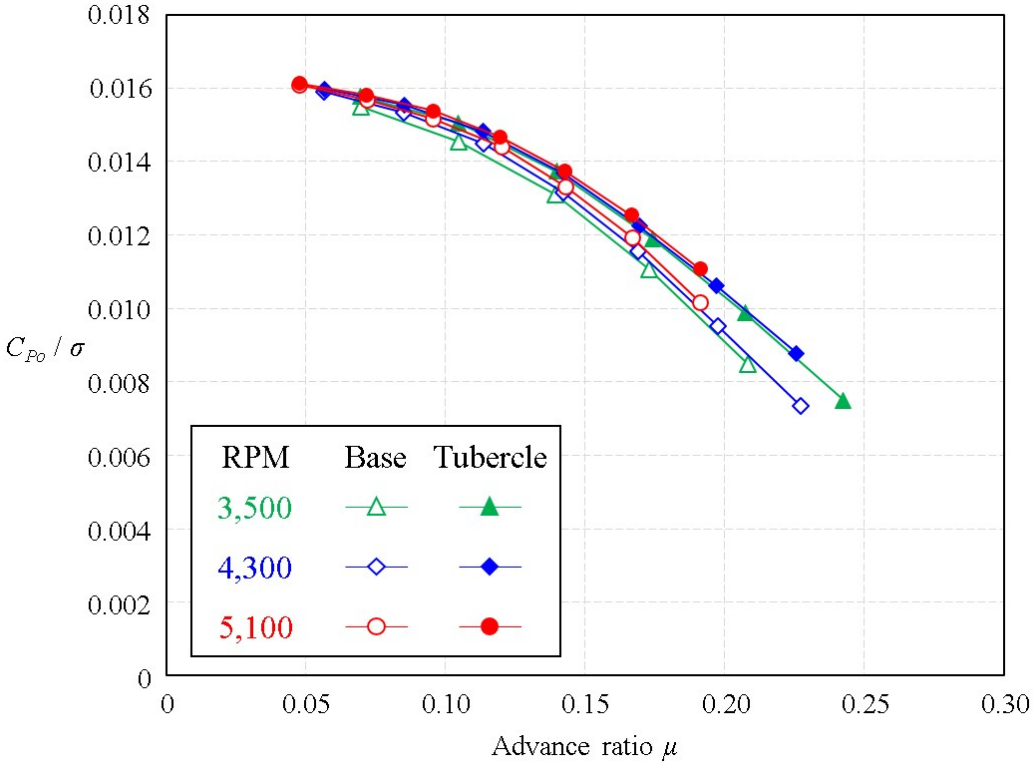

Figure 5.6. Variations of power coefficient divided by solidity (C_{Po}/σ) with the advance ratio for the base and tubercle models at $\alpha = 40°$.

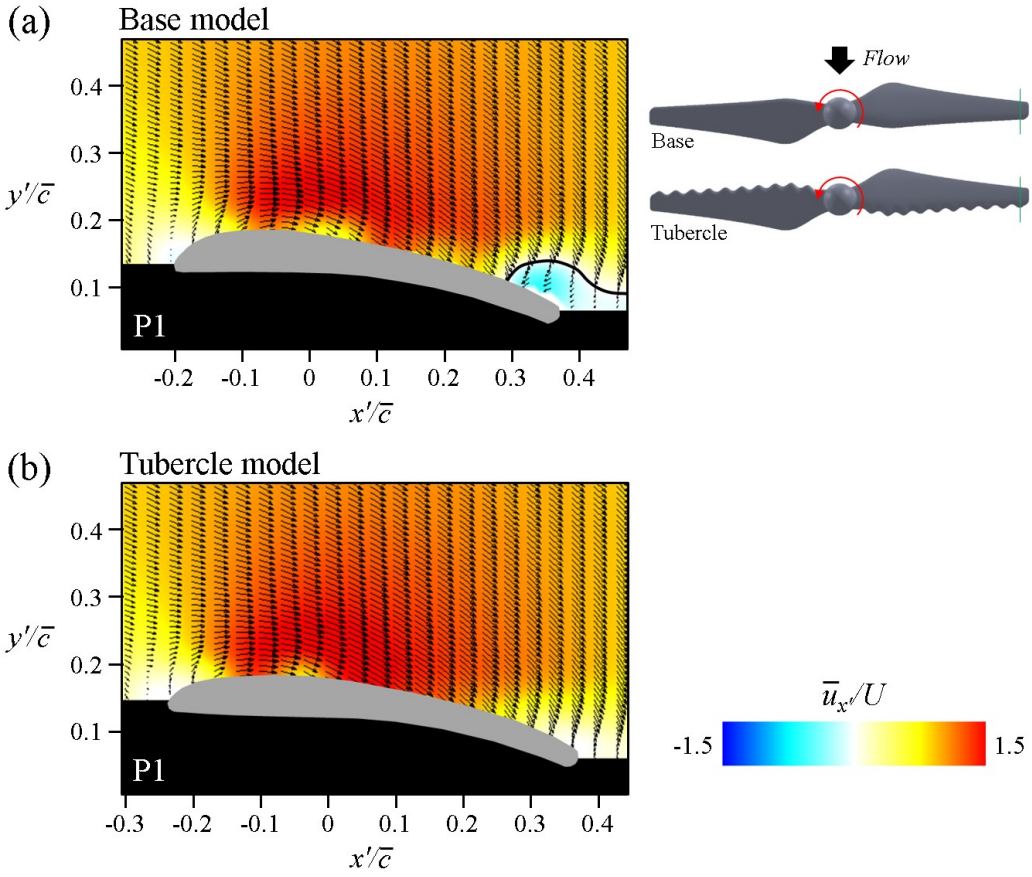

Figure 5.7. Contours of the mean x'-direction velocity and velocity vectors at the spanwise location of P1 (advancing side): (a) Base model; (b) Tubercle model. Here, the black thick line denotes $\bar{u}_{x'}$=0. The spanwise locdation corresponding to P1 is indicated by green solid lines in the right figure.

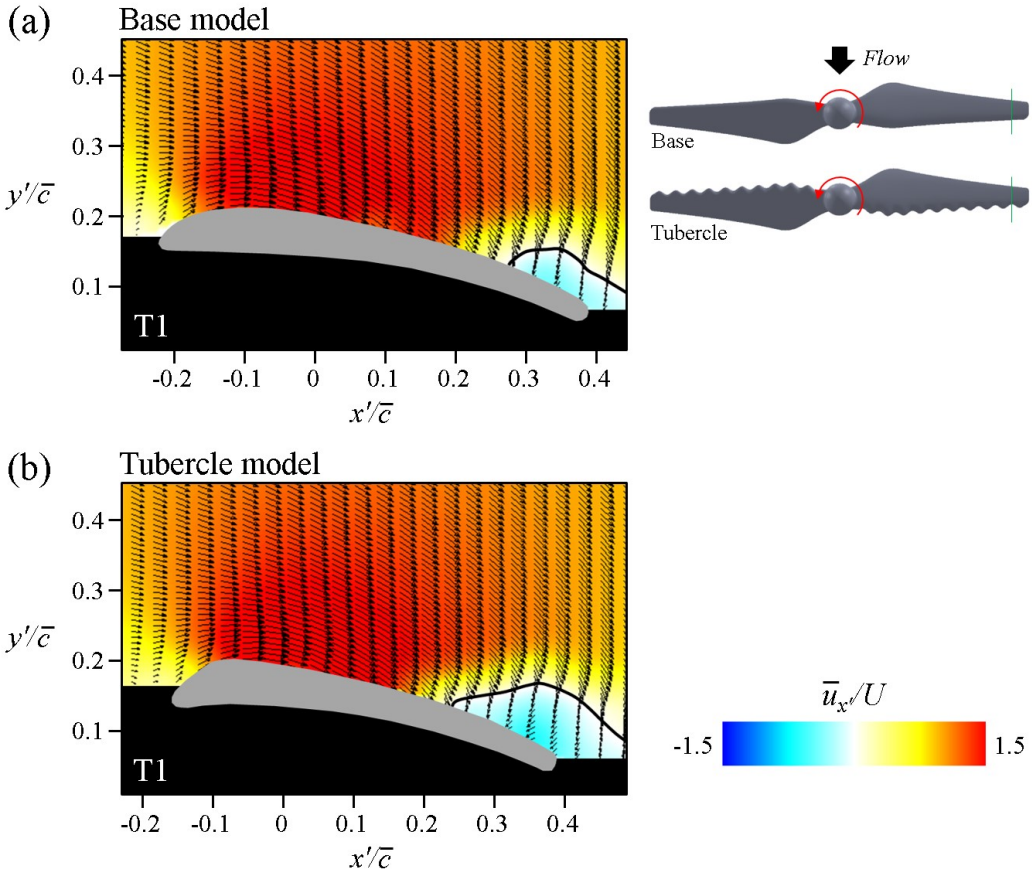

Figure 5.8. Contours of the mean x'-direction velocity and velocity vectors at the spanwise location of T1 (advancing side): (a) Base model; (b) Tubercle model. Here, the black thick line denotes $\bar{u}_{x'}$=0. The spanwise locdation corresponding to T1 is indicated by green solid lines in the right figure.

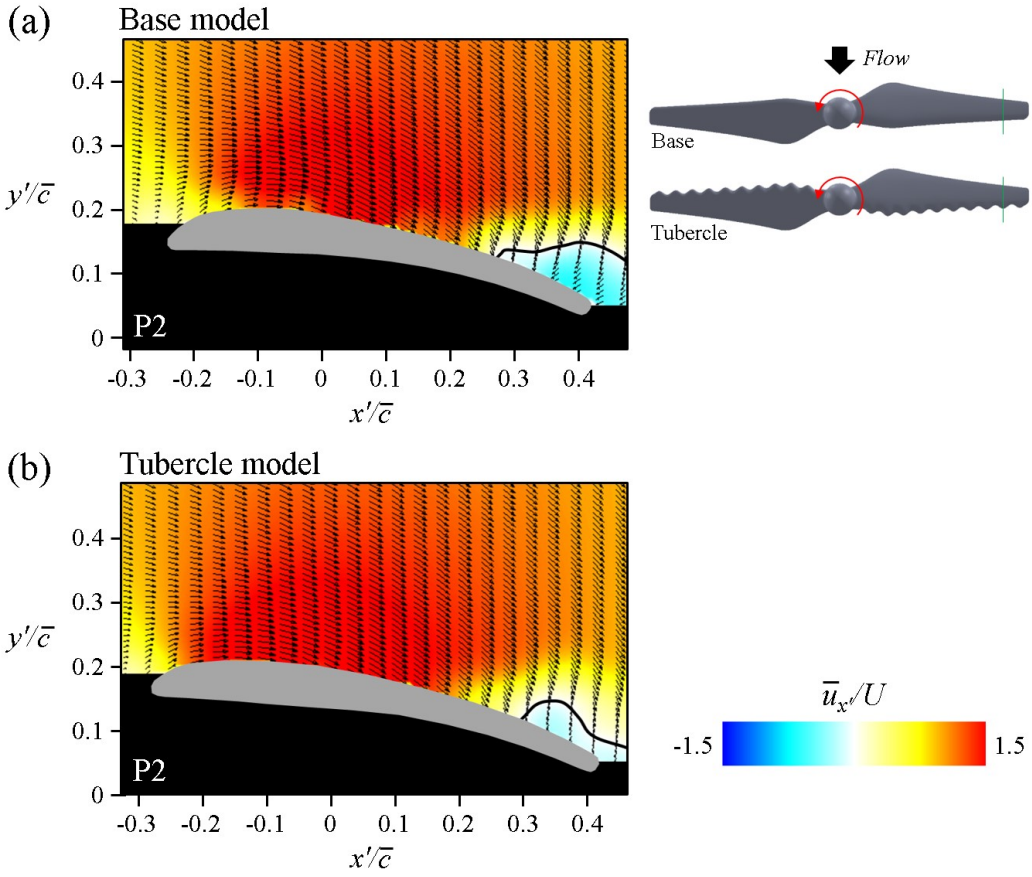

Figure 5.9. Contours of the mean x'-direction velocity and velocity vectors at the spanwise location of P2 (advancing side): (a) Base model; (b) Tubercle model. Here, the black thick line denotes $\bar{u}_{x'}$=0. The spanwise locdation corresponding to P2 is indicated by green solid lines in the right figure.

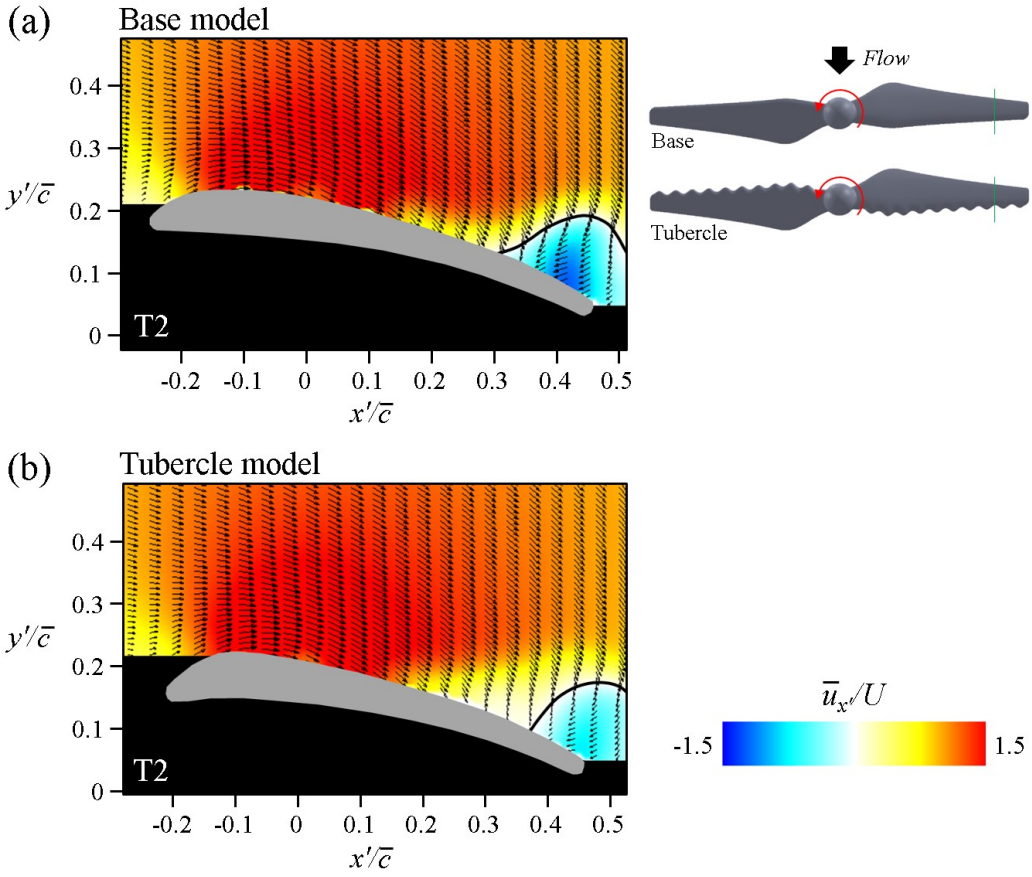

Figure 5.10. Contours of the mean x'-direction velocity and velocity vectors at the spanwise location of T2 (advancing side): (a) Base model; (b) Tubercle model. Here, the black thick line denotes $\bar{u}_{x'}$=0. The spanwise locdation corresponding to T2 is indicated by green solid lines in the right figure.

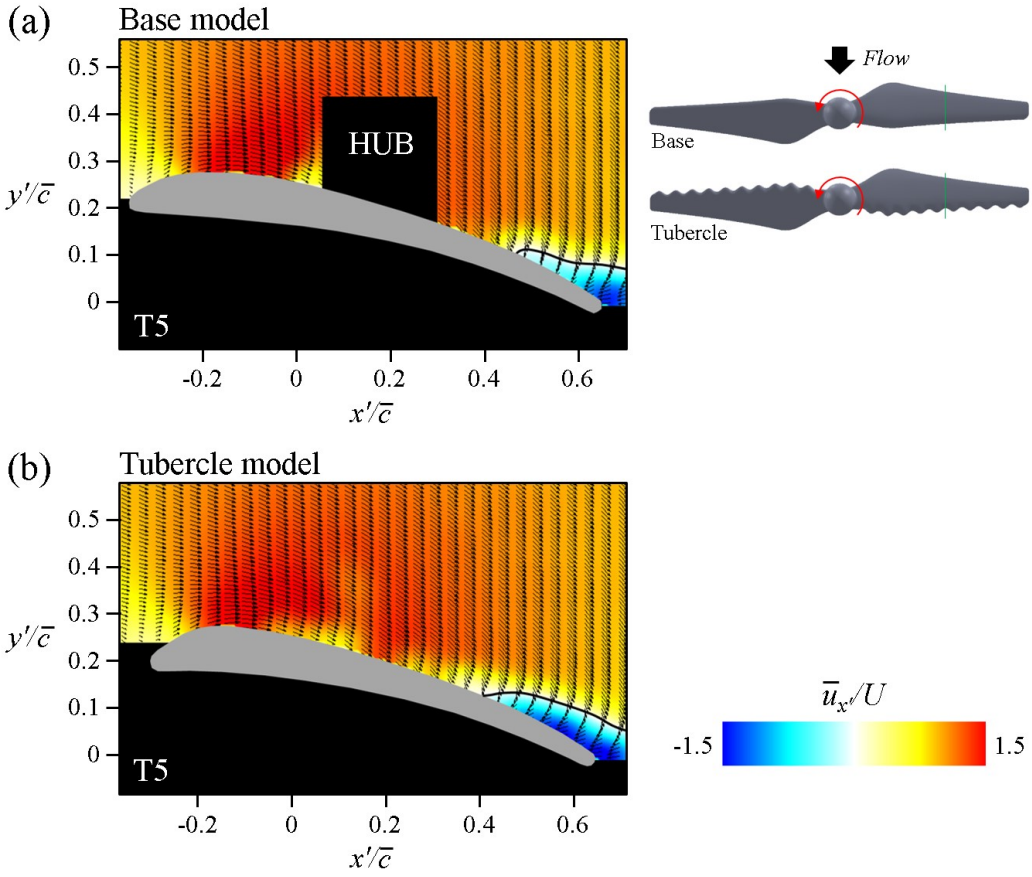

Figure 5.11. Contours of the mean x'-direction velocity and velocity vectors at the spanwise location of T5 (advancing side): (a) Base model; (b) Tubercle model. Here, the black thick line denotes $\bar{u}_{x'}$=0. The spanwise locdation corresponding to T5 is indicated by green solid lines in the right figure.

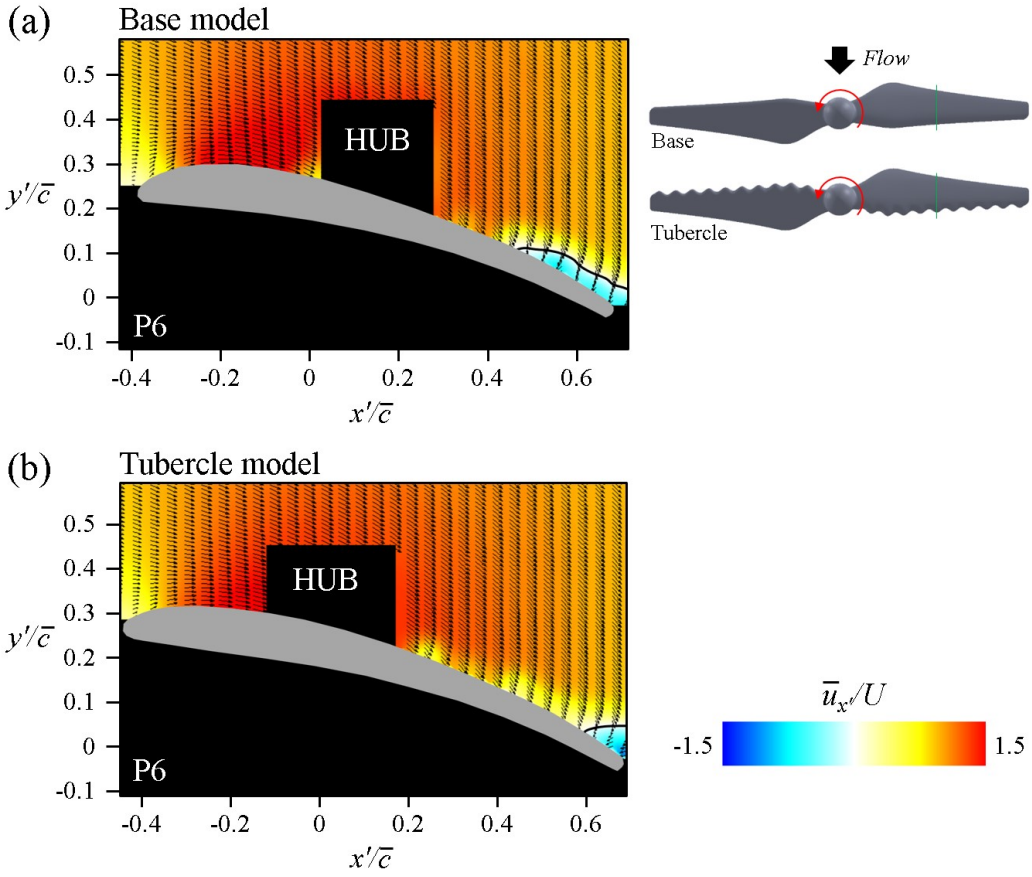

Figure 5.12. Contours of the mean x'-direction velocity and velocity vectors at the spanwise location of P6 (advancing side): (a) Base model; (b) Tubercle model. Here, the black thick line denotes $\bar{u}_{x'}$=0. The spanwise locdation corresponding to P6 is indicated by green solid lines in the right figure.

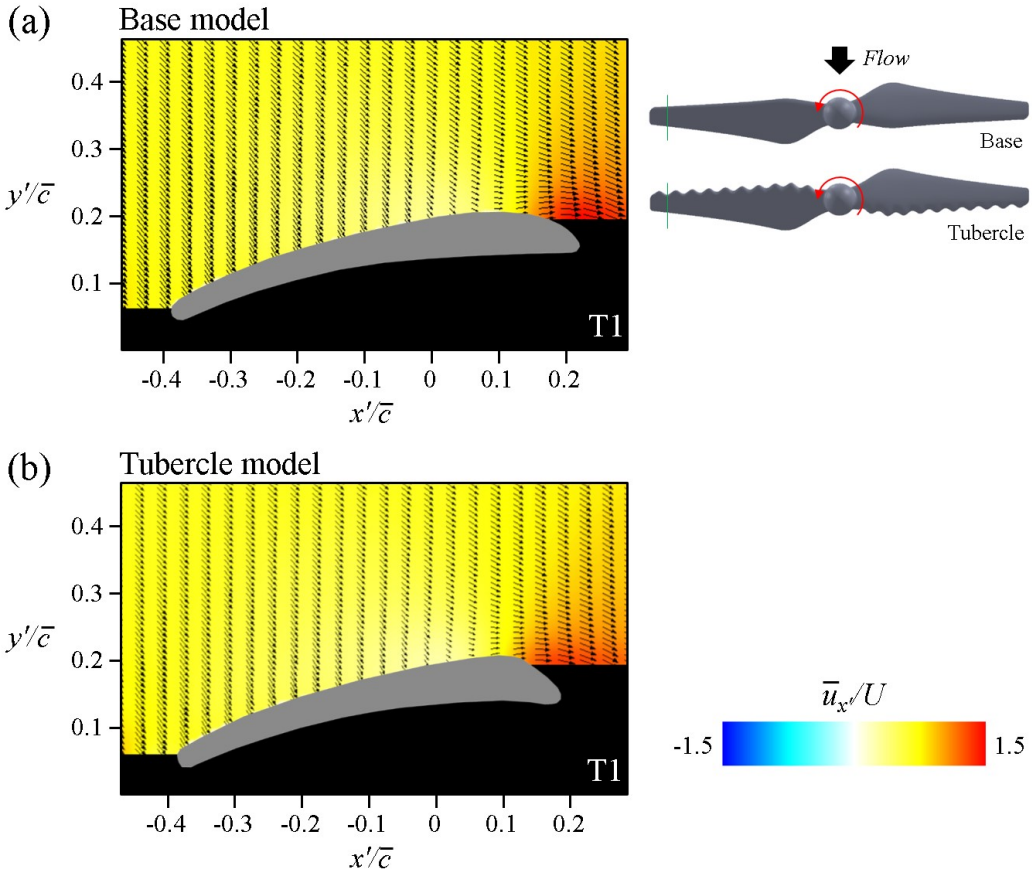

Figure 5.13. Contours of the mean x'-direction velocity and velocity vectors at the spanwise location of T1 (retreating side): (a) Base model; (b) Tubercle model. Here, the black thick line denotes $\bar{u}_{x'}$=0. The spanwise locdation corresponding to T1 is indicated by green solid lines in the right figure.

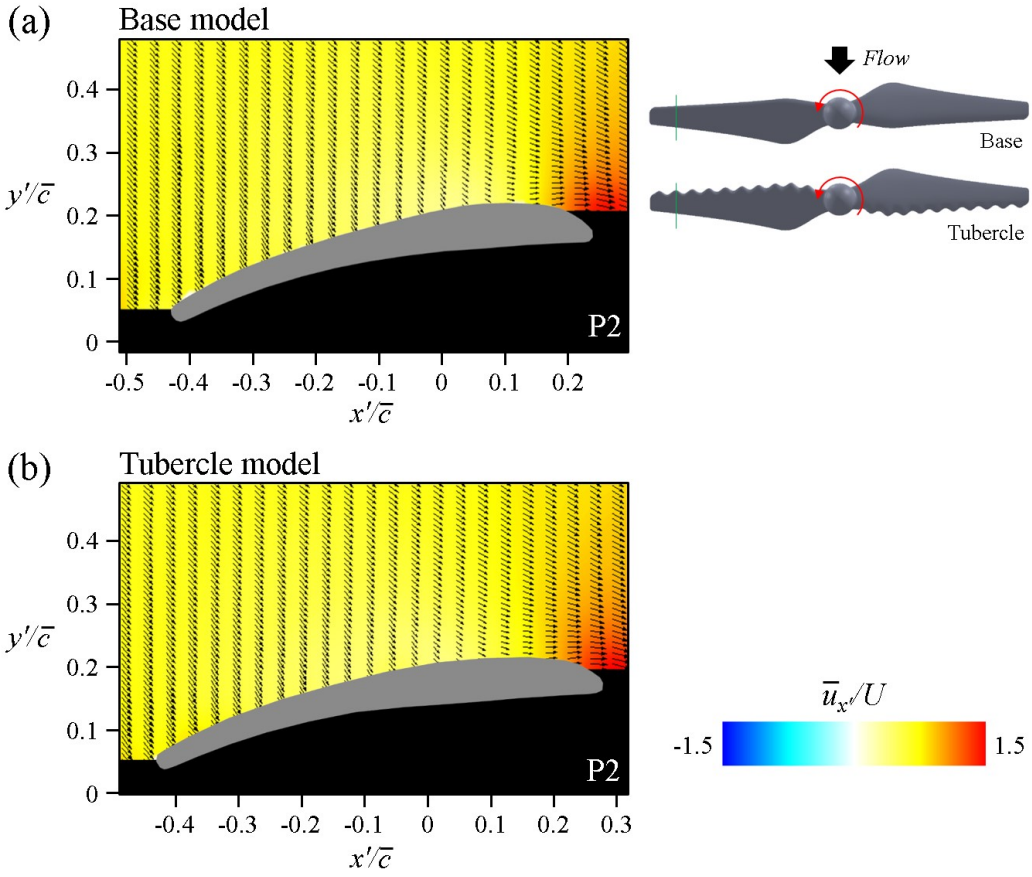

Figure 5.14. Contours of the mean x'-direction velocity and velocity vectors at the spanwise location of P2 (retreating side): (a) Base model; (b) Tubercle model. Here, the black thick line denotes $\bar{u}_{x'}$=0. The spanwise locdation corresponding to P2 is indicated by green solid lines in the right figure.

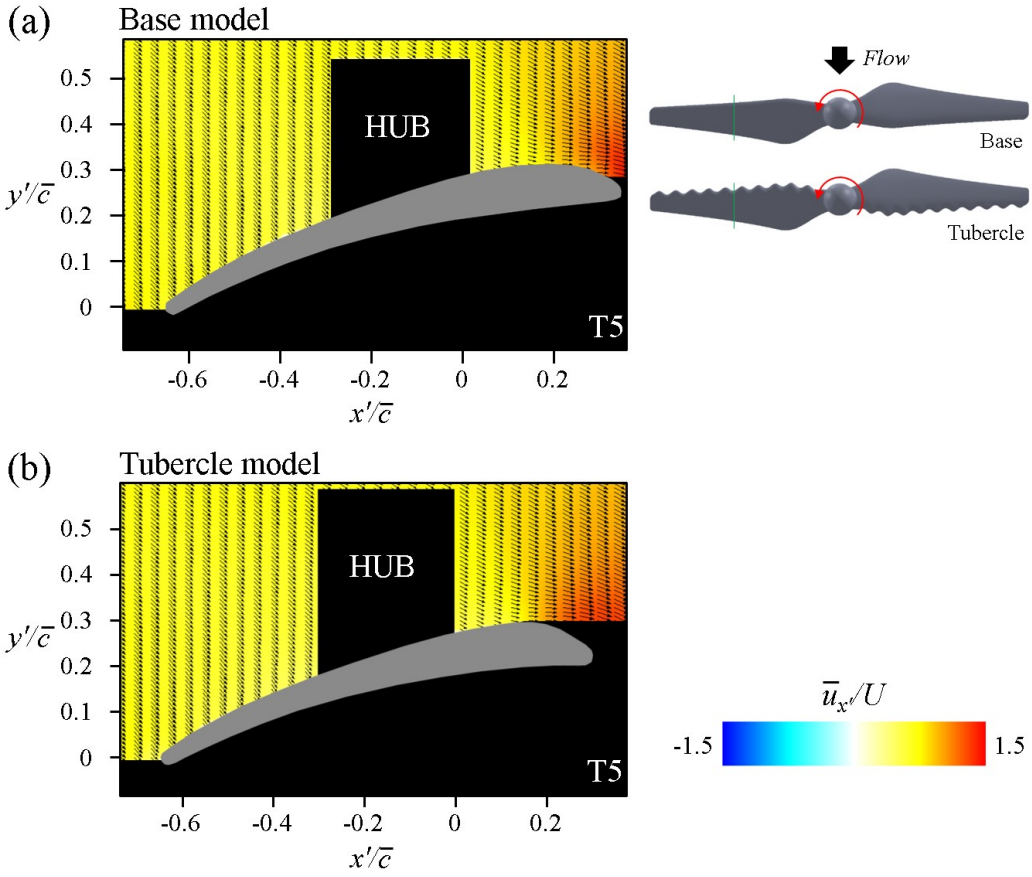

Figure 5.15. Contours of the mean x'-direction velocity and velocity vectors at the spanwise location of T5 (retreating side): (a) Base model; (b) Tubercle model. Here, the black thick line denotes $\bar{u}_{x'}$=0. The spanwise locdation corresponding to T5 is indicated by green solid lines in the right figure.

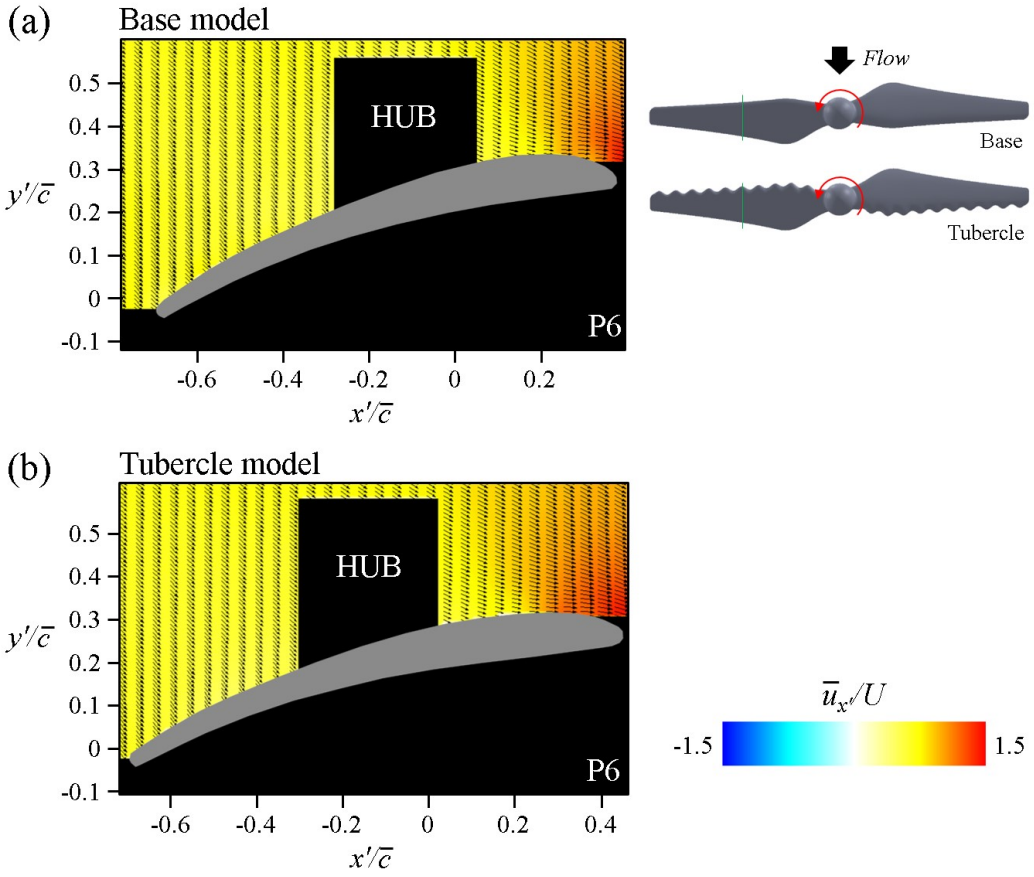

Figure 5.16. Contours of the mean x'-direction velocity and velocity vectors at the spanwise location of P6 (retreating side): (a) Base model; (b) Tubercle model. Here, the black thick line denotes $\bar{u}_{x'}$=0. The spanwise locdation corresponding to P6 is indicated by green solid lines in the right figure.

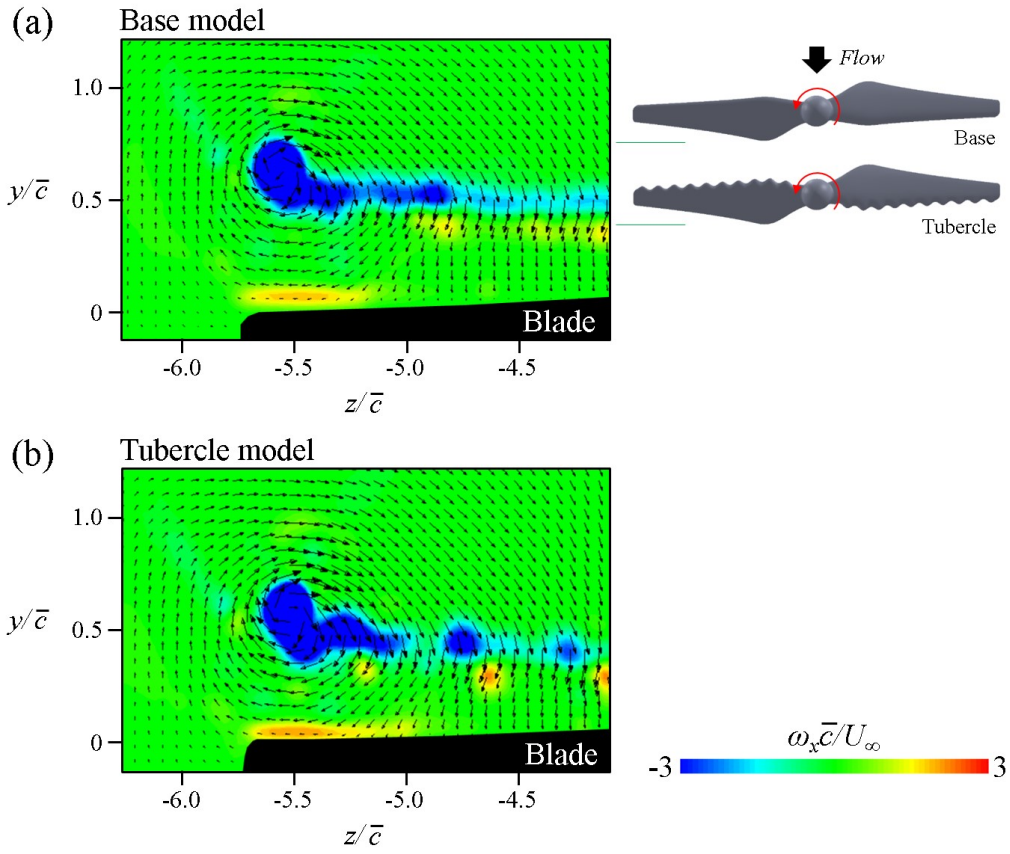

Figure 5.17. Contours of the mean ω_x and velocity vectors in the wake of the base and tubercle models ($-6.27 \leq z/\bar{c} \leq -4.10$): (a) Base model; (b) Tubercle model. The PIV measurement locdation is indicated by green solid lines in the right figure.

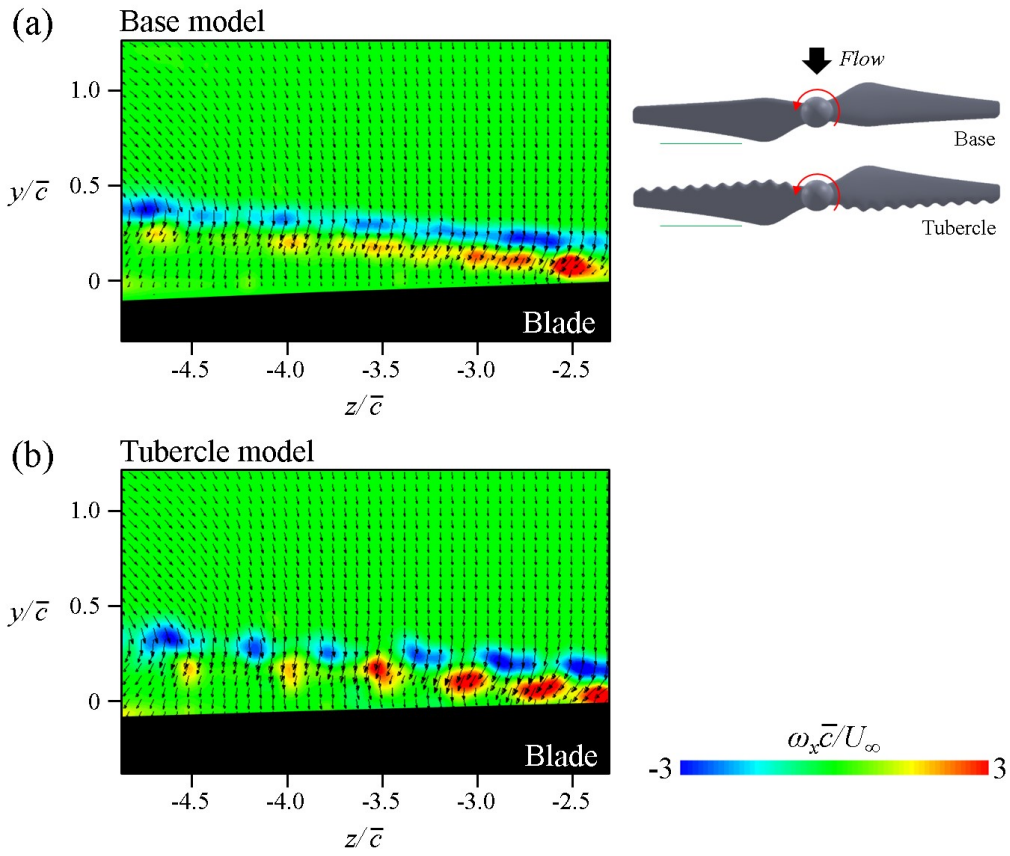

Figure 5.18. Contours of the mean ω_x and velocity vectors in the wake of the base and tubercle models ($-4.87 \leq z/\bar{c} \leq -2.30$): (a) Base model; (b) Tubercle model. The PIV measurement locdation is indicated by green solid lines in the right figure.

Chapter 6

Summary and Concluding Remarks

In this study, we experimentally investigated flow structures responsible for the wing performance enhancements by the leading-edge tubercles. The tubercles delayed the stall angle by 7° and increased the maximum lift coefficient by about 22% at the Reynolds number of 180,000. Flow separation first occurred near the tip region for both wing models. As the angle of attack increases, in case of the base model, flow separation near the tip progressed inboard, resulting in full separation. For the tubercle model, however, the stall was delayed because of two vortical motions. The first was the streamwise vortex pairs evolving from foci inside the hemi-spherical separation bubbles near the leading edge (see figure 6.1). At $\alpha = 4°$, the chordwise surface pressure distribution shows that the peak magnitude of -C_p at the trough is higher than that at the peak (figure 3.11). This resulted in a strong chordwise adverse pressure gradient at the trough, inducing an early flow separation. Hence, a hemi-spherical separation bubble with counter-rotating foci was formed near the leading edge behind the trough, which generated a streamwise vortex pair in the downstream. These vortical structures were dominant at low angles of attack and prevented inboard spanwise progression of flow separation (from tip to root). The second was the asymmetric streamwise vortex pairs evolving from foci inside separated regions after the mid-chord region, which were dominant flow structures at near-stall angles of attack (figure 6.1). A vortex with negative vorticity was more

dominant than that with positive vorticity as they approached the trailing edge (figure 3.24). These structures delayed flow separation at the peak spanwise locations, resulting the stall delay. At a post-stall angle of attack ($\alpha = 16°$), flow separation occurred in both inboard and outboard regions inside which clockwise and counter-clockwise rotating foci were formed, respectively (figure 3.7(b)). Streamwise vortices with negative or positive vorticity evolved from these foci (figure 6.1), and attached the flow in the mid-span region, resulting in a higher lift coefficient than that of the base model. These three types of vortical structures distinguished by their locations of occurrence were given in figure 6.1.

Leading-edge tubercles were applied to a quadrotor blade to improve performance in forward flight condition. The new blade had ten tubercles with amplitude of 6% and wavelength of 50% of the mean chord length of the blade without tubercles (figure 5.1). The thrust and power were measured by using 6-axis force sensor and velocity field around the blade models were captured through 2D-PIV test setup. The Reynolds numbers considered in this study were 62,000 − 90,000, which is based on the mean chord length and tip velocity of the blade model. The angle of attack is 40°. At low advance ratio ($\mu \leq 0.1$), thrust and power coefficient of the both models were similar to each other within the experimental uncertainty range (figures 5.5 and 5.6). As advance ratio increases, however, blade performance was enhanced by increasing the thrust coefficient more than the power coefficient (figures 5.5 and 5.6). Velocity fields on the suction surface of the blade model showed that leading-edge tubercles reduce back-flow regions behind peaks near the tip- and mid-span region at advancing side (figures 5.7 − 5.12). This resulted from the counter-rotating streamwise vortex pairs observed in the wake of the tubercle model (figures 5.17 and 5.18), inducing downwash motion behind peaks.

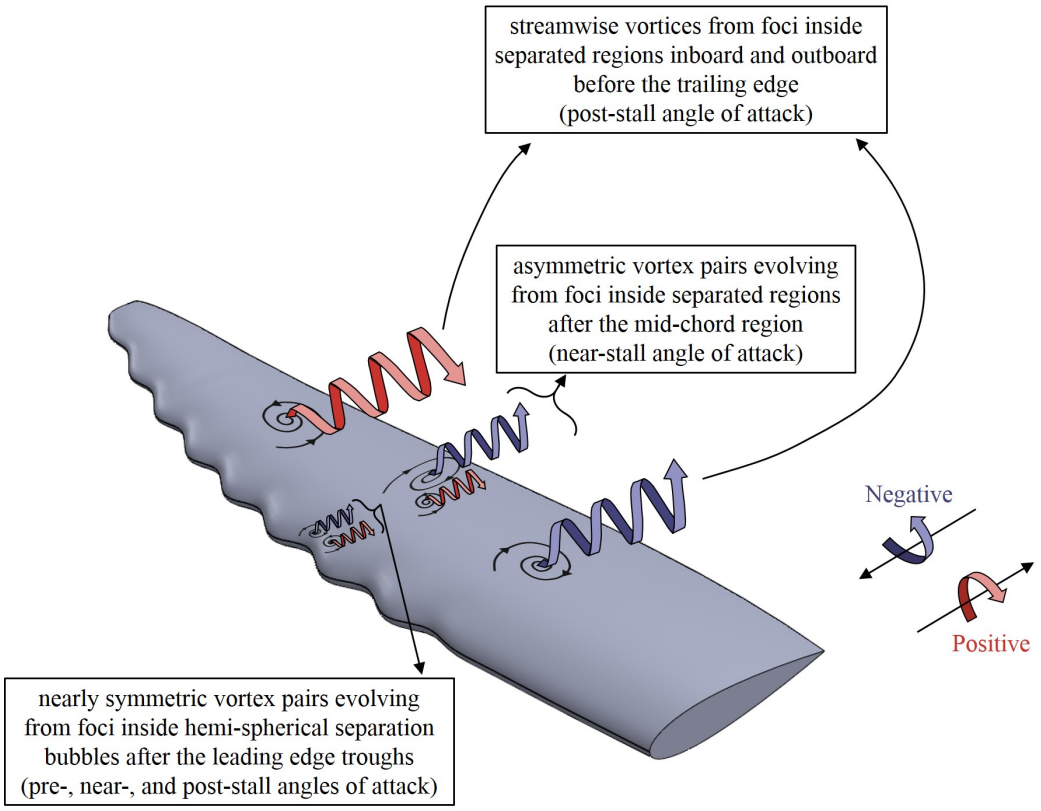

Figure 6.1. Schematic diagram of the mechanisms responsible for the performance enhancements by tubercles at various angles of attack. Red and blue curves denote vortices with positive and negative vorticity, respectively.

References

Adrian, R. J., Christensen, K. T. & Liu, Z. C. 2000 Analysis and interpretation of instantaneous turbulent velocity fields. *Exp. Fluids.* **29**, 275-290.

Asghar, A., Perez, R. E. & Allan, W. D. E. 2018 Application of leading edge tubercles to enhance propeller performance. *Applied Aerodynamics Conference (Atlanta, USA).*

Bang, K., Kim, J., Lee, S. I. & Choi, H. 2016 Hydrodynamic role of longitudinal dorsal ridges in a leatherback turtle swimming. *Sci. Rep.* **6**, 34283.

Barlow, J. B., Rae, W. H. & Pope, A. 1999 Low-speed wind tunnel testing. John Wiley & Sons.

Bartol, I. K., Gharib, M., Weihs, D., Webb, P. W., Hove, J. R. & Gordon, M. S. 2003 Hydrodynamic stability of swimming in ostraciid fishes: role of the carapace in the smooth trunkfish *Lactophrys triqueter* (Teleostei: Ostraciidae). *J. Exp. Biol.* **206**, 725–744.

Bartol, I. K., Gharib, M., Webb, P. W., Weihs, D. & Gordon, M. S. 2005 Body-induced vortical flows: a common mechanism for self-corrective trimming control in boxfishes. *J. Exp. Biol.* **208**, 327-344.

Benedict, M., Winslow, J., Hasnain, Z. & Chopra, I. 2015 Experimental investigation of micro air vehicle scale helicopter rotor in hover. *Int. J. Micro Air Veh.* **7**, 231-255.

Bolzon, M. D., Kelso, R. M. & Arjomandi, M. 2016 Formation of vor-

tices on a tubercled wing, and their effects on drag. *Aerosp. Sci. Technol.* **56**, 46-55.

Bolzon, M. D., Kelso, R. M. & Arjomandi, M. 2017 Force measurements and wake surveys of a swept tubercled wing. *J. Aerosp. Eng.* **30**, 04016085.

Bolzon, M. D., Kelso, R. M. & Arjomandi, M. 2017 Performance effects of a single tubercle terminating at a swept wing's tip. *Exp. Therm. Fluid Sci.* **85**, 52-68.

Brandt, J. & Selig, M. 2011 Propeller performance data at low Reynolds numbers. *49th AIAA Aerospace Sciences Meeting including the New Horizons forum and Aerospace Exposition*, 1255.

Cai, C., Zuo, Z., Liu, S. & Wu, Y. 2015 Numerical investigations of hydrodynamic performance of hydrofoils with leading-edge protuberances. *Adv. Mech. Eng.* **7**, 1-11.

Choi, H., Park, H., Sagong, W. & Lee, S. 2012 Biomimetic flow control based on morphological features of living creatures. *Phys. Fluids* **24**, 121302.

Coleman, H. W. & Steele, W. G. 2009 Experimentation, validation, and uncertainty analysis for engineers. John Wiley & Sons.

Cully, B. P. 2017 PIV flow field measurements of hovering rotors with leading edge protuberances. No. USNA-TSPR-455. NAVAL ACADEMY ANNAPOLIS MD ANNAPOLIS United States.

Custodio, D., Henoch, C. W. & Johari, H. 2015 Aerodynamic characteristics of finite span wings with leading-edge protuberances. *AIAA J.* **53**, 1878-1893.

Deters, R. W., Ananda Krishnan G. K. & Selig, M. 2014 Reynolds

number effects on the performance of small-scale propellers. *32nd AIAA Applied Aerodynamics Conference*, 2151.

Diebold, J. M. 2012 Aerodynamics of a swept wing with leading-edge ice at low Reynolds number. MS Thesis. University of Illinois at Urbana-Champaign.

Favier, J., Pinelli, A. & Piomelli, U. 2012 Control of the separated flow around an airfoil using a wavy leading edge inspired by humpback whale flippers. *C. R. Mec.* **340**, 107-114.

Fish, F. E. & Battle, J. M. 1995 Hydrodynamic design of the humpback whale flipper. *J. Morphol.* **225**, 51-60.

Fish, F. E. & Lauder, G. V. 2006 Passive and active flow control by swimming fishes and mammals. *Annu. Rev. Fluid Mech.* **38**, 193-224.

Fouras, A. & Soria, J. 1998 Accuracy of out-of-plane vorticity measurements derived from in-plane velocity field data. *Exp. Fluids* **25**, 409-430.

Guerreiro, J. L. E. & Sousa, J. M. 2012 Low-Reynolds-number effects in passive stall control using sinusoidal leading edges. *AIAA J.* **50**, 461-469.

Hain, J. H. W., Carter, G. R., Kraus, S. D., Mayo, C. A. & Winn, H. E. 1982 Feeding behavior of the humpback whale, MEGAPTERA NOVAEANGLIAE, in the western North Atlantic. *Fish. Bull.* **80**, 259-268.

Hansen, K. L., Kelso, R. M. & Dally, B. 2010 An investigation of three-dimensional effects on the performance of tubercles at low Reynolds numbers. *17th Australasian Fluid Mechanics Conference (Auckland, New Zealand).*

Hansen, K. L., Kelso, R. M. & Dally, B. 2011 Performance variations of leading-edge tubercles for distinct airfoil profiles. *AIAA J.* **49**, 185-194.

Hansen, K. L., Rostamzadeh, N., Kelso, R. M. & Dally, B. 2016 Evo-

lution of the streamwise vortices generated between leading edge tubercles. *J. Fluid Mech.* **788**, 730-766.

Hoffmann, G., Huang, H., Waslander, S. & Tomlin, C. 2007 Quadrotor helicopter flight dynamics and control: Theory and experiment. *AIAA Guidance, Navigation and Control Conference and Exhibit*, 6461.

Hosseinverdi, S., Jacobi, R. & Fasel, H. F. 2015 Topology and flow structures of three-dimensional separation bubbles: The effect of aspect ratio. *45th AIAA Fluid Dynamics Conference*.

Johari, H., Henoch, C., Custodio, D. & Levshin, A. 2007 Effects of leading-edge protuberances on airfoil performance. *AIAA J.* **45**, 2634-2642.

Jurasz, C. M. & Jurasz, V. P. 1979 Feeding modes of the humpback whale *MEGAPTERA NOVAEANGLIAE* in Southeast Alaska. *Sci. Rep. Whales Res. Inst.* **31**, 69-83.

Karthikeyan, N., Sudhakar, S. & Suriyanarayanan, P. 2014 Experimental studies on the effect of leading edge tubercles on laminar separation bubble. *52nd Aerospace Sciences Meeting (National Harbor, USA)*, 1279.

Lang, A. W., Bradshaw, M. T., Smith, J. A., Wheelus, J. N. Motta, P. J., Habegger, M. L. & Hueter, R. E. 2014 Movable shark scales act as passive dynamic micro-roughness to control flow separation. *Bioinspir. Biomim.* **9**, 036017.

Miklosovic, D. S., Murray, M., Howle, L. E. & Fish, F. E. 2004 Leading-edge tubercles delay stall on humpback whale (Megaptera novaeangliae) flippers. *Phys. Fluids* **16**, 39-42.

Miklosovic, D. S., Murray, M. & Howle, L. E. 2007 Experimental evaluation of sinusoidal leading edges. *J. Aircr.* **44**, 1404-1407.

Moore, K. & Ning, A. 2016 Aerodynamic performance characterization of

leading edge protrusions on small propellers. *54th Aerospace Sciences Meeting (San Diego, USA)*, 1786.

New, T. H., Wei, Z. Y. & Cui, Y. D. 2015 On the effectiveness of leading-edge modifications upon cambered SD7032 wings. *10th Pacific Symposium on Flow Visualization and Image Processing (Naples, Italy)*, 115.

Pedro, H. T. C. & Kobayashi, M. H. 2008 Numerical study of stall delay on humpback whale flippers. *46th AIAA Aerospace Sciences Meeting and Exhibit (Reno, USA)*, 584.

Pérez-Torró, R. & Kim, J. W. 2017 A large-eddy simulation on a deep-stalled aerofoil with a wavy leading edge. *J. Fluid Mech.* **813**, 23-52.

Raffel, M., Willer, C., Wereley, S. & Kompenhans, J. 2013 Particle image velocimetry: a practical guide. Springer.

Rostamzadeh, N., Hansen, K. L. & Kelso, R. M. 2014 The formation mechanism and impact of streamwise vortices on NACA 0021 airfoils performance with undulating leading edge modification. *Phys. Fluids* **26**, 107101.

Rostamzadeh, N., Kelso, R. M. & Dally, B. 2016 A numerical investigation into the effects of Reynolds number on the flow mechanism induced by a tubercled leading edge. *Theor. Comput. Fluid Dyn.* **30**, 1-32.

Serson, D., Meneghini, J. R. & Sherwin, S. J. 2017 Direct numerical simulations of the flow around wings with spanwise waviness. *J. Fluid Mech.* **826**, 714-731.

Skillen, A. & Revell, A. 2015 Flow over a wing with leading-edge undulations. *AIAA J.* **53**, 464-472.

Stanway, M. J. 2008 Hydrodynamic effects of leading-edge tubercles on con-

trol surfaces and in flapping foil propulsion. MS Thesis. Massachusetts Institute of Technology.

Theys, B., Dimitriadis, G., Andrianne, T., Hendrick, P. & De Schutter, J. 2014 Wind tunnel testing of a VTOL MAV propeller in tilted operating mode. *International Conference on Unmanned Aircraft Sytems (Orlando, USA)*, 1064-1072.

Theys, B., Dimitriadis, G., Hendrick, P. & De Schutter, J. 2017 Experimental and numerical study of micro-aerial-vehicle propeller performance in oblique flow. *J. Aircr.* **54**, 1076-1084.

van Nierop, E. A., Alben, S. & Brenner, M. P. 2008 How bumps on whale flippers delay stall: an aerodynamic model. *Phys. Rev. Lett.* **100**, 054502.

Weber, P. W., Howle, L. E. & Murray, M. 2010 Lift, drag, and cavitation onset on rudders with leading-edge tubercles. *Mar. Technol. Sname News* **47**, 27-36.

Weber, P. W., Howle, L. E., Murray, M. & Miklosovic, D. S. 2011 Computational evaluation of the performance of lifting surfaces with leading-edge protuberances. *J. Aircr.* **48**, 591-600.

Wei, Z., New, T. H. & Cui, Y. D. 2018 Aerodynamic performance and surface flow structures of leading-edge tubercled swept-back wings. *AIAA J.* **56**, 423-431.

Wei, Z., Lian, L. & Zhong, Y. 2018 Enhancing the hydrodynamic performance of a tapered swept-back wing through leading-edge tubercles. *Exp. Fluids* **59**, 103.

Weihs, D. 1981 Effects of swimming path curvature on the energetics of fish motion. *Fish. Bull.* **79**, 171-176.

Willert, C. E. & Gharib, M. 1991 Digital particle image velocimetry. *Exp. Fluids* **10**, 181-193.

Yoon, H. S., Hung, P. A., Jung, J. H. & Kim, M. C. 2011 Effect of the wavy leading edge on hydrodynamic characteristics for flow around low aspect ratio wing. *Comput. Fluids* **49**, 276-289.

Zhang, M., Wang, G. F. & Xu, J. Z. 2013 Aerodynamic control at low-Reynolds-number airfoil with leading-edge protuberances. *AIAA J.* **51**, 1960-1971.

Zhang, M., Wang, G. F. & Xu, J. Z. 2014 Experimental study of flow separation control on a low-Re airfoil using leading-edge protuberance method. *Exp. Fluids* **55**, 1710.

전단부 혹을 가진 날개 주변의 유동 특성

서울대학교 대학원
기계항공공학부
김 희 수

요 약

혹등고래 가슴지느러미의 전단부 혹은 실속 이후 받음각 영역에서 그들의 유체역학적 성능을 향상시키는 것으로 알려져 있다. 우리는 표면오일유동 가시화와 입자영상유속계를 사용하여 전단부 혹을 가지는 3차원 날개 위의 와류 구조에 대해 연구를 수행하였다. 자유류 속도와 평균 시위 길이를 기준으로 하는 레이놀즈 수 180,000에서 혹의 유무에 따라 두 가지 날개 모델을 고려하였다. 이 레이놀즈 수에서, 전단부 혹은 실속각을 7° 지연시키고, 최대양력계수를 약 22% 증가시켰다. 낮은 받음각에서, 두 모델 모두 익단 근처에서 유동 박리가 발생하였다. 받음각이 증가함에 따라, 전단부 혹이 없는 모델의 경우 유동 박리가 날개 모델 안쪽으로 (루트 지역으로) 발달하는 반면, 전단부 혹이 있는 모델의 경우 두 가지 유형의 와류 구조가 발생하여 유동 박리가 모델 안쪽으로 진행하는 것을 막고 실속각을 8°에서 15°로 지연시켰다. 두 가지 유형의 와류 구조 중 하나는 서로 반대 방향으로 회전하는 주유동방향 와류 쌍들로, 실속 전, 실속 근처, 그리고 실속 후 받음각 영역에서 전단부 골 근처 반구형 박리거품으로부터 발달한다. 다른 하나의 와류 구조는 비대칭 주유동방향 와류 쌍들로, 실속 근처 받음각 영역에서 중간시위 지역 뒤의 박리 유동 지역에서 발달한다. 실속 이후 받음각에서는 (α = 16°), 시계방향과 시계 반대 방향으로 회전하는 강한 주유동방향 와류들이 루트와 익단 지역의 후단부 근처에서 각각 발생하며, 중간스팬 지역의 유동 박리를 지연시켜 전단부 혹이 없는 모델과 비교했을 때 전단부 혹이 있는 모델이 더 높은 양력계수를 가지게 해준다.

전진 비행 조건에서 쿼드로터 블레이드의 성능을 향상시키기 위해 전단부 혹을 적용하였다. 새로운 블레이드는 전단부에 10개의 혹을 가졌으며,

혹의 크기와 간격은 각각 혹이 없는 블레이드 평균시위 길이의 6%와 50%에 해당한다. 회전속도는 3,500 RPM - 5,100 RPM까지 고려하였으며, 이때 레이놀즈 수 범위는 62,000 - 90,000이다. 전진 비행 속도는 4 m/s - 16 m/s까지 고려하였으며, 이때 진행비 범위는 0.048 - 0.279이다. 그리고 본 연구에서는 받음각 40°를 고려하였다. 낮은 진행비 ($\mu \leq 0.1$)에서는, 두 모델의 동력 계수와 추력 계수가 실험 오차 범위 내에서 비슷한 값을 보였다. 하지만 진행비가 증가함에 따라, 전단부 혹이 동력 계수보다 추력 계수를 더 크게 향상시키며, 이는 블레이드의 성능이 향상되었음을 나타낸다. 속도장 측정 결과로부터, 서로 반대 방향으로 회전하는 주유동방향 와류 쌍들이 전단부 혹을 가진 블레이드의 후류에서 관찰되었으며, 이들이 블레이드가 전진하는 영역에서 전단부 혹 피크 뒤의 역류지역을 감소시키는 것을 확인하였다.

주요어 : 혹등고래 가슴지느러미, 전단부 혹, 유동 박리, 실속 지연, 쿼드로터 블레이드, 전진 비행

학 번 : 2013-31295